学位論文

Analysis of Stern-Gerlach experiment for the ferromagnetic Clusters

強磁性クラスターを用いた Stern-Gerlach 実験の解析について

平成11年12月博士(理学)申請

東京大学大学院理学系研究科
物理学専攻

濱元 信州

Analysis of Stern-Gerlach experiment for the ferromagnetic clusters

Nobukuni HAMAMOTO

A dissertation submitted in partial fulfillment of the requirements for the degree of Doctor of Science

Department of Physics, University of Tokyo

December 1999

Abstract

Intermediate coupling model is proposed to analyze the Stern-Gerlach experiment for the clusters. In this model, the macroscopic magnetic moment and the angular momentum of the cluster is coupled through an anisotropic potential originated from the magnetic anisotropy. We calculate analytically the strong and weak coupling limit of the magnetic susceptibility. Even for the strong coupling limit, the susceptibility does not reach the locked moment limit because of the recoil effect. The susceptibility of the weak coupling limit is derived as $\frac{2}{9}\frac{\mu B}{k_B T}$. The profile and magnetization of the rotating cluster in the magnetic field are calculated. The magnetic moment and anisotropic coupling are extracted from the experiment for $Fe_{120-140}$ and $Gd_{17,23}$ clusters.

Contents

1 Introduction 5

2 The Stern-Gerlach experiment 11
- 2.1 Experimental apparatus . . . 11
- 2.2 Method of analysis . . . 15
  - 2.2.1 Superparamagnetism . . . 16
  - 2.2.2 Locked moment . . . 18
- 2.3 Experimental results . . . 25
  - 2.3.1 3d transition metals . . . 27
  - 2.3.2 4f lanthanide . . . 35
  - 2.3.3 4d transition metals . . . 38
  - 2.3.4 Alloys . . . 39

3 The Intermediate coupling model 43
- 3.1 The Intermediate coupling model . . . 43
- 3.2 Classical limit of the intermediate coupling model . . . 49
  - 3.2.1 The Schwinger boson representation of angular momentum . . . 49
  - 3.2.2 Classial limit of the intermediate-coupling model . . . 52
- 3.3 Magnetic susceptibility . . . 57
  - 3.3.1 Susceptibility for strong coupling . . . 58
  - 3.3.2 Susceptibility for weak coupling . . . 61
  - 3.3.3 Intermediate coupling . . . 64
- 3.4 Profiles and magnetization . . . 68

4 Conclusions 87

Appendix A 91
- A.1 Angular momentum . . . 91
- A.2 The derivation of susceptibility for the locked moment limit . . . 93
- A.3 The second order cumulant for the decoupling regime . . . 95
- A.4 Derivation of the matrix element . . . 97
  - A.4.1 Anisotropic interaction . . . 97
  - A.4.2 The matrix element of Zeeman coupling . . . 98

A.5 The large angular momentum limit of the Clebsch-Gordan and Racah coefficient 99
A.5.1 The Clebsch-Gordan coefficient 99
A.5.2 The Racah coefficient 100

Chapter 1

Introduction

Atoms, nuclei and atomic clusters have attracted our interest as "finite quantum systems" which are different from infinite systems like crystals and field in its degree of freedom. Shell structure is one of the typical examples. The structure originally found in the electrons in an atom was again proposed in the atomic nucleus by Mayer and Jensen in 1950's. In 1984, the shell structure was discovered in Sodium clusters by Knight *et al.* [1, 2]. The new findings of the shell structure are closely related to the recent developments of experimental technique of small particle systems. Actually, the latest cluster source developed in 1960's and 70's could produce the gas phase clusters of only a few atoms [3]. The situation undergoes a complete change in 1983 when Knight *et al.* develop new source and make alkali metal clusters of 1 to 100 atoms. The new source clarifies unexpected features of the clusters of 1 to 1,000 atoms like shell structure.

The new physics of atomic clusters involving the development of nanotechnologies is unique and different from the atomic and nuclear physics. For electrons in an atom, the mean field governed by nucleus can be well approximated to the Coulomb potential. In the atomic clusters, the mean field cannot be easily calculated because of many body effects of the nuclei. Experiments on atomic clusters have a great advantage of one on the nucleus in controlling the number of atoms or nucleons, especially, in the large number region. The infinite matter of nucleons, or the nuclear matter, cannot be realized easily, except the neutron stars. Yet, bulk crystal, which is atomic counterpart of nuclear matter, can be easily obtained. Thus, the atomic clusters are easy to handle in examining the finite-infinite transition in the finite systems. In addition, the experimental apparatuses for cluster physics are much cheaper than those for the nuclear physics.

The main subject of this thesis is about magnetism of atomic clusters. In atomic

clusters, magnetic properties are expected to be different from those in bulk due to the large fraction of surface atoms. In thin films or fine particles of magnetic elements, the magnetic moment and the magnetic anisotropy are reported and are larger than the bulk materials [4]. In the age of miniaturization of electric devices, there is increasing need to understand magnetic properties of clusters. In particular, investigation of the magnetic moment and the magnetic anisotropy is important in finding materials for high-density magnetic memory devices.

While bulk magnetic properties of ferromagnetic materials have been widely studied and are relatively well understood, experimental works on finely divided clusters of magnetic materials have not been performed. To investigate unexplored properties of magnetism in clusters, de Heer *et al.* apply the Stern-Gerlach technique to the magnetic clusters using the new source. Their experiment reveals various properties of the magnetization of the clusters.

Let us consider the experimental set up. First, clusters formed by laser evaporation are cooled by helium gas, and then the clusters are expanded to form a molecular beam. In the present study we assume that the clusters are in thermal equilibrium. Density of clusters in the beam is low, so that the clusters may be assumed to be isolated beyond the equilibration zone. Therefore, each cluster stays in a certain quantum state in the beam. Finally, the clusters enter into a Stern-Gerlach magnet and are deflected by the interaction between the gradient of the magnetic field and the magnetic polarization of electron spin induced by the magnetic field. At the entrance of the magnet, strength of the field changes gradually in time, and a time dependent interaction for the electron spin causes a transition from the initial quantum state to other quantum states. If the time dependence is sufficiently weak compared with coupling of the spin to other modes, the transition probability to other modes can be neglected. This is called the adiabatic approximation. In the present work, we calculate the deflection profile and the magnetization of the clusters with this assumption.

The Stern-Gerlach experiment is first performed to atoms to investigate quantization of electron spin. The resultant deflection profile for the silver atom shows symmetric two peaks implying quantization of the electron spin. We show in Fig. 1.1 the deflection profile obtained by the experiment for iron clusters performed by de Heer. The profile is quite different from the profile for atoms: Only one peak is observed to the profile, and the peak moves towards the right as increasing the magnetic field. The experimental data

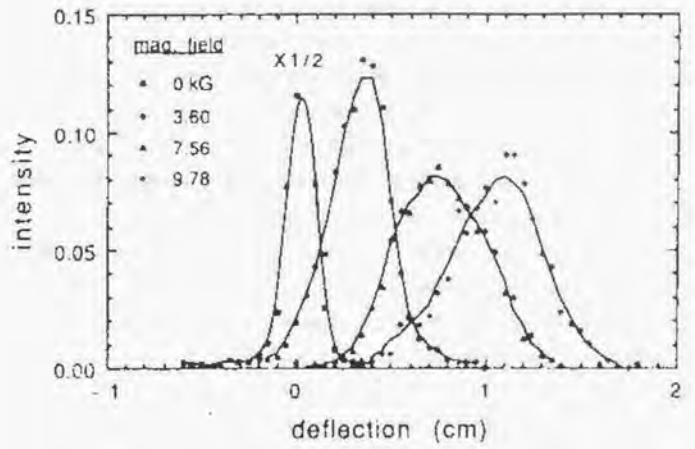

Figure 1.1: The Stern-Gerlach profiles of $Fe_{120-140}$ clusters for several value of the magnetic field. Note that deflections are uniquely in the deflection of increasing field. The zero-field profile is normalized to $\frac{1}{2}$, whereas the others are normalized to 1.

gave rise to controversy about how to interpret the data and the discussion still continues even now. It is important to study the intrinsic magnetic moment. For this purpose, we need to establish a method to extract the intrinsic magnetic moment from the observed deflection profile in the present stage of the study. This is the motivation for the present work.

The size of a cluster is small enough to be regarded as a single domain system, and the electrons produce a single giant magnetic moment. We will call it the super-electron spin in this thesis. If the electrons were completely decoupled from other degrees of freedom such as rotational motion of the cluster, the deflection profile would be a flat horizontal distribution independent of the field strength like the profiles of atoms. But the observed profiles do not follow the profile mentioned above. A small coupling of the magnetic moment to internal coordinates of the cluster gives rise to spin relaxation, making the profile different from the flat distribution. Hence it is important to make clear how various couplings produce observed deflection profiles.

There are two possibilities for degrees of freedom which couples with the super-electron

spin; rotation and vibration of the cluster. We do not believe that the vibrational modes are very important in the present experiment, because even the lowest vibrational excitation energies, which are estimated from the speed of sound in the bulk and the cluster diameter, are much larger than the temperature of the experiment. In the typical case of iron cluster of 100 atoms, the lowest rotational and vibrational excitation energies are roughly estimated as 1.92×10^{-4}K and 134K, respectively. Temperature of the clusters in the experiment is estimated as 330 K at the most.

Two models have been proposed to analyze the Stern-Gerlach experiment. The simplest model is superparamagnetism in which the population of the magnetic states are proportional to a Boltzmann factor [5]. In other words, the cluster rotation plays a role as a heat bath for the super-electron spin in the magnetic field. In practical analysis for extracting the giant magnetic moment, the Langevin formula is widely employed. It assumes equilibrium with a thermal reservoir at a temperature which is the same as the source of the cluster beam. However, it predicts a rather sharp deflection profile which is quite different from the broad profile that is often observed. Hence, the superparamagnetic model seems to be too simple for the analysis of the experiments.

Another simple model is locked-spin model in which the super-electron spin is frozen with respect to the intrinsic orientation of the cluster, which is of course free to rotate [6, 7, 8]. This model seems successful in reproducing the small peak observed near the zero deflection angle, which experimentalists call "superparamagnetism". But it is applicable only to Gd clusters. Furthermore, the model ignores the angular momentum of the super-electron spin, which is known to give recoil effects as known as the Einstein-de Haas effect.

In this thesis, we propose the intermediate coupling model as a method to extract the giant magnetic moment from the deflection profile [8], which is the main subject of the thesis. In the intermediate coupling model, the giant magnetic moment couples with the rotational degrees of freedom through the anisotropic coupling caused by the magnetic anisotropy energy. This model covers the superparamagnetic and locked-moment models as weak and strong coupling limits, respectively.

The paper consists of four chapters. Chapter 2 is devoted to overview the Stern-Gerlach experiment for the clusters. The method of the experiment is described in Sec. 2.1. The method of the analysis is discussed in Sec. 2.2 which includes the review of the superparamagnetism and the locked moment model. The experimental results are

discussed in Sec. 2.3. The main contents of the thesis are described in Chapter 3 in which the full description of the intermediate coupling model is given. The classical limit of the present model is discussed to interpret the result of quantum mechanical calculation of the model in Sec. 3.2. The calculation and analysis of the profile, the magnetization and the magnetic susceptibility using the intermediate coupling model are also discussed in the chapter. The contents presented here are based mainly on Ref. [9]. Examples of the analysis are given in the last of this chapter. Finally in Chapter 4, we present the conclusion of this study.

Chapter 2

The Stern-Gerlach experiment

The Stern-Gerlach technique is originally developed to investigate magnetic properties of atoms. The result of the experiment clarified the quantization of electron spin. In 1985, the technique is revised and applied to the clusters. Iron clusters of 2 to 17 atoms and aluminum clusters of 2 to 25 atoms are firstly investigated by the experimental technique [10, 11]. In the late of 80's through the beginning of 90's, Two groups led by de Heer [12] and Bloomfield [13] intensively investigated a variety of magnetic clusters like iron, nickel and gadolinium. The apparatus used in the Stern-Gerlach experiment of the clusters is shown in Fig. 2.1. It consists of four main sections: three high vacuum chambers and a magnet assembly. The metal cluster beam is formed in the first chamber, sent through the gradient magnet, and then analyzed in the third chamber. In this section, we review the method and apparatus of the experiment.

2.1 Experimental apparatus

The cluster beam is formed in the first chamber: the cluster source section. The clusters are produced by a laser vaporization method. A pulsed Nd-doped yttrium aluminum garnet (YAG) laser strikes a iron, nickel or some other metal disk and forms a hot plasma. It is quenched in a short pulse of helium gas in the chamber. Size of the clusters grows as the helium gas cools down the plasma. Then, mixture of helium gas and vaporized metal passes through a tube which terminates in a cylindrical nozzle. It subsequentially expands into the vacuum.

The cluster beam, in which the clusters are fairly isolated, enters into the second vacuum chamber through the molecular beam skimmer. Inside this chamber, the cluster beam goes through two collimating slits. In the experiment by de Heer *et al.*, the width

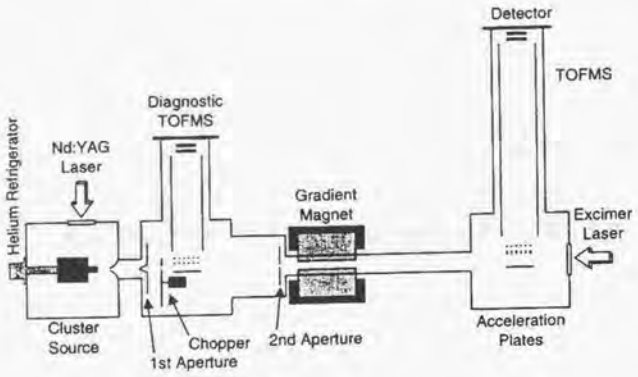

Figure 2.1: The whole apparatus of the Stern-Gerlach experiment of Bloomfield group.

and height of the slits are 0.8 mm and 4.0 mm, respectively. Bloomfield *et al.* select smaller slits of which width and height are 0.4 mm and 2.5 mm, respectively. Between the two collimating slits, Bloomfield *et al.* sets a mechanical chopper wheel, 20 cm in diameter, which serves two purposes. First, it provides a packet of the cluster of which velocity is selected. Second, it lets us determine the time τ_{res}, the clusters have been in the source. The chopper wheel rotates 100 times per second and normally blocks the cluster beam. As it rotates, a narrow slit in the wheel transverses the cluster beam's path and permits the beam to pass for a period of about 100 μs. On the other hand, de Heer *et al.* directly specify the time when the cluster creates and the cluster detected. They calculate velocity from the time difference and length of the apparatuses.

After the collimation and chopping section, the cluster beam passes through a gradient field magnet. This magnet is 250 mm (125 mm) long for Bloomfield (de Heer) group. In the entrance of the magnet the clusters feel the time-dependent force which may cause the transition of quantum states. We can estimate transition probability for Fe_N clusters using Landau-Zener formula,

$$P = \exp\left(-\frac{2\pi V_{12}}{\hbar|\dot{x}|\left|\frac{d}{dz}(\epsilon_1 - \epsilon_2)\right|}\right). \tag{2.1}$$

The velocity of the clusters in the supersonic beam $\dot{x}$ is order of 1000m/s. The spatial

variation of energy level $\frac{d\epsilon}{dz}$ can be estimated through the spatial variation of magnetic field and magnetic moment of the cluster. The strength of magnetic field outside the magnet decreases as moving away from the magnet and the magnetic field seems to be almost negligible in 1 mm distance from the magnet. The magnetic moment of the cluster seems to be $3\mu_B N$ at the most, in which N means the number of atoms in the cluster. The anisotropic interaction V_{12} is 36 mK per atom. Therefore, the probability for $N = 100$ is much less than the order of 10^{-3} and is negligible.

The cluster beam enters the ionization region of the time-of-flight mass spectrometer (TOFMS), located 1.183 m downstream from the gradient magnet. In de Heer's setup, the spectrometer is located 1.0 m downstream from the magnet. During their flight from the magnet to the mass spectrometer, the clusters that experienced a transverse force in the gradient magnet will deflect away from their zero-field trajectories.

The clusters are ionized with the light from an 193 nm ArF excimer laser, which is synchronized with the vaporization laser. Deflections of the particles are measured either by a position-sensitive time-of-flight mass spectrometry or by scanning the collimated ionizing light, across the beam.

While Bloomfield uses the latter method, de Heer group applies both method to observe the cluster deflection. The beam of excimer laser to a narrow stripe is scanned across the beam. Only those clusters that are exposed to the narrow laser beam are ionized, accelerated, and subsequently detected in the mass spectrometer. The beam position and mass spectra are recorded to determine spatial locations of each cluster size in the beam.

The time-averaged projection of a cluster's magnetization, in other words the expectation value of the quantum state of the cluster, is determined through the cluster's mass, m_{cluster}, velocity v, total deflection, d, the magnetic field gradient, dB/dz, the length of the magnet, L, and the length of the flight between the magnet and the mass spectrometer, D. The experimental magnetization of the cluster per atom, μ_{expt} is obtained as

$$\mu_{\text{expt}} = \frac{dm_{\text{cluster}}v^2}{(dB/dz)(DL + L^2/2)}. \tag{2.2}$$

To obtain hot cluster a illuminate YAG laser to heat clusters is put before the entering the Stern-Gerlach field in experimental apparatus of de Heer group. Heating the clusters by the laser at center along the beam has several advantages. The main one is that the total angular momentum is not affected, since photons carry relatively small angular momenta. Thus the laser heating increases only the vibrational temperature. This method

can produce the hot clusters of which temperature are determined by the Poisson statistics. Though the magnetic properties of hot cluster is interesting, the assumptions of our model do not cover the laser heating.

The cluster temperature is the hardest parameter to control and also have been in controversial aspect of the experiments even if the clusters are not heated by the laser. In fact, the experiments performed by de Heer group [14] and Bloomfield group [15] apply the different method to control the temperature of the clusters. We describe each method to measure the temperature of the clusters by de Heer group and Bloomfield group.

In the source, the vapor produced by the laser is cooled and expanded by the pulsed injection of the helium gas. Cooling by the helium gas condensates the clusters. The collisions between helium gas and the clusters cool the various degrees of freedom of the clusters at different rates. The translational motions are cooled best. The rotational degrees of freedom is cooled efficiently but not as well. The vibrations, on the other hand, are cooled substantially less effectively. The rate of rotational and vibrational degrees of freedom can be understood by two effects described below. Firstly, the range of collisions involved in the rotational cooling is much longer than that in the vibrational cooling. Vibrational degrees of freedom is essentially cooled by direct impacts of the helium atom with the cluster. Secondly, the rotations constitute only 3 degrees of freedom, while the vibrations have $3N$ degrees of freedom.

Because of pulsed injection of the helium gas, pressure of the expansion is time dependent. The group of de Heer uses the temperature of nozzle and detection time to know the temperature of the clusters. The detection time τ is defined as the time difference between the time when the cluster is created and the time when cluster is detected. The detection time reflects the pressure of the source. For small τ the warm cluster is expanded [16]. Therefore, they control relative vibrational temperature of the clusters by observing nozzle temperature and detection time τ.

Bloomfield *et al.* reported in Ref. [17, 13] that their source is designed to generate a beam of clusters with the well defined vibrational temperature. In the de Heer group's method, they use supersonic expansion to decide the relative temperature of the cluster. However it is difficult to measure the vibrational temperature because a supersonic expansion is highly out-of-equilibrium precess. Bloomfield and coworkers adopt completely different strategy. Their source permits clusters to grow more slowly and to equilibrate thermally with their environment before undergoing a free-jet expansion into the surrounding vacuum chamber. Then, the cluster temperature is measured as the temperature of entire source. They proposed two evidences of the cluster equilibrating with the source. Firstly, they measured the magnetization of cobalt clusters as a function of the residence time in the source. At very short residence times, they observe almost no deflection of the clusters. The longer a cluster remains in the source, the more magnetic it appears. In the long residence time, more than 2000 μs, the magnetization saturates as seen Fig. 2.2. Secondly, they performed the experiment in the different expansion conditions and confirmed the results are not changed.

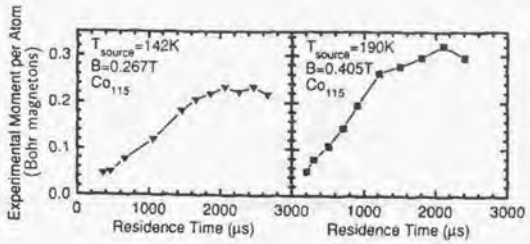

Figure 2.2: The magnetization observed in the experiment as a function of the residence time for Co_{115} clusters. The magnetization saturates implying the cluster attain the thermal equilibrium

From these results, they confirmed the cluster vibrational temperature is equal to the source temperature, which is independent of the expansion conditions. However, they do not mention about the translational or rotational temperature. In fact, for the analysis of gadolinium clusters, they do not adopt source temperature as the rotational temperature.

2.2 Method of analysis

The deflection profile is the main result which includes information about magnetization of clusters in the magnet. For example, the deflection profile for silver atom has two peaks of which positions are symmetric. Now that the quantization of angular momentum is confirmed, the analysis of the experiment is not difficult. The number of peak and distance between the position of peaks represent the magnitude of electron spin and of

magnetic moment, respectively. Like the experiment for atom, the deflection profile of aluminum clusters are symmetric discrete peak according to the total spin of the clusters. In 1986, D.M. Cox and coworkers determined the magnitude of spin of ground state of aluminum clusters from the experiment [11]. The experiment has been applied to a variety of elements like iron, nickel and gadolinium. However, unlike the profile of atoms, the profiles obtained in these clusters are asymmetric and do not have several peaks. The profiles are explained mainly as a result of two behaviors: superparamagnetism and locked moment. In this section, we review the two models and some typical results which can be fairly explained by each model.

2.2.1 Superparamagnetism

Superparamagnetism is originally found in an ensemble of fine particles of magnetic materials. In bulk ferromagnetic materials, the direction of spin magnetic moment is influenced by two types of interaction, the exchange and the dipole interaction. The exchange interaction is quite short-ranged and aligns the directions of spin magnetic moment, whereas the dipole interaction is long-ranged and anti-aligns the directions. When all spins are aligned to a single direction, it is uneconomical in dipole energy. To reduce the dipole energy, the specimen is divided into domains in which the direction of spins are aligned [18].

A magnetic particle below the critical size consists of a single magnetic domain, thus, it has a single giant magnetic moment μ. When the assembly of the magnetic particles has reached a state of thermodynamic equilibrium with the external magnetic field, total magnetization μ_z is calculated, which yields the Langevin function,

$$\frac{\mu_z}{\mu} = L(x) = \coth x - \frac{1}{x}, \tag{2.3}$$

where $x = \frac{\mu B}{k_B T}$. This thermodynamic behavior is observed in an ensemble of magnetic fine particles. Heukelom, Broeder, and Van Reijen observed the magnetization curve in some different temperatures in silica-supported nickel catalysts [19]. Their result is illustrated in Fig. 2.3. The magnetization curve is clearly scaled by B/T and the curve does not show hysteresis, which is typical in thermodynamic equilibrium properties. These properties are also observed in fine particles of iron suspended in mercury [20] or a colloidal suspension of single domain magnetic iron oxide particles [21].

Recently, S. N. Khanna and S. Linderoth applies superparamagnetism for the clusters [5]. They assume that the clusters are smaller than the critical sizes for the single domain, and that the magnetic anisotropy energy is much smaller than the thermal energy. They considered that weak coupling perturbs the direction of the magnetic moment and explores the entire Boltzmann distribution of permitted orientation in a very short time. To confirm the behavior being achieved in the Stern-Gerlach experiment, they estimate the relaxation time τ of the clusters. The superparamagnetic relaxation is described by the Arrhenius law with a relaxation time:

$$\tau = \tau_0 e^{\frac{KV}{k_B T}}, \tag{2.4}$$

where C is the magnetic anisotropy energy per unit volume, T is the temperature, and V is the volume of the cluster. The value of τ_0, which depends on the gyromagnetic precession time, is usually $\simeq 10^{-10} - 10^{-13}$sec [22]. The value of C has been determined $C \simeq 2 \times 10^7$ ergs/cm^3 from the magnetization measurements on granular alloys of 20-40 Å iron in matrices [23]. Using these values, the relaxation time about 100 K is estimated as 1-1000 ps. On the other hand, the time of which the cluster passes through the Stern-Gerlach magnet is about 100 μs. Therefore, the flight time of the cluster beam is much larger than the relaxation time τ of the clusters. They conclude from the result that the clusters in the Stern-Gerlach magnet behave as superparamagnetic.

The experiment can be analyzed by fitting the magnetization curve to the Lengevin function, which extract the magnetic moment of the clusters. In this method only the average property of the profile is used to extract the magnetic moment. The method does not use the information of the shape of the profile. However, as will be seen in Sec. 2.3, the method can extract a reasonable value for the magnetic moment of 3d transition metal clusters without fitting the shape of the profiles. Therefore, this phenomenological method is believed to explain the experiment of the 3d transition metal clusters. The profile of superparamagnetic clusters is considered to be the Gaussian of which width is sharp independent of the magnetic field like Fig. 1.1. In a superparamagnetic cluster, magnetic moment of a single cluster reaches thermal equilibrium. Time average of magnetization for each clusters is decided by the phase average. Then, profile becomes Gaussian profile of which width decided by the thermal fluctuations. However, it does not explained what degrees of freedom mainly couples with the super-spin of the clusters, and achieves the thermal equilibrium of super-spin.

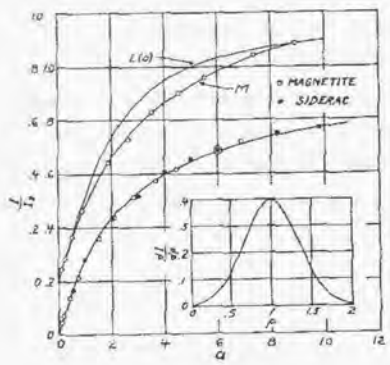

Figure 2.3: The observed magnetization of silica-supported nickel catalysis [21]. The lower curve agrees with the modified Lengivin curve obtained by assuming the particle moment distribution shown in the insert. The ratio of magnetic field and temperature a is defined as $a = \frac{\mu B}{k_B T}$. Values of I and I_s means magnetization of the cluster per volume and magnetic moment of the cluster per volume, respectively.

2.2.2 Locked moment

The experimental work on the Stern-Gerlach experiment for the gadolinium clusters was published in 1992 by D.C. Douglass, J.P. Bucher and L.A. Bloomfield [24]. They find out that the deflection profile of the gadolinium clusters are strongly depend on the number of atoms. In some clusters like Gd_{22}, the profile is similar with one of the superparamagnetism, while, in the other clusters like Gd_{21} and Gd_{23}, the magnetic field of Stern-Gerlach magnet drastically spreads out the cluster beam. The profile of Gd_{21} is illustrated in Fig. 2.4.

The spreading behavior has been considered as the result of the locked moment. The magnetic moment is dragged along the rotating cluster in the locked moment model, which broadens the distribution of magnetization. The experimentalists themselves regard the spreading profile as the result of locked moment behavior and calculate the profile by solving numerically the classical equation of motion. Later, G. Bertsch and K. Yabana [6] calculated the profile by using the locked moment model in a quantum mechanical approach. The classical treatment of the locked moment model is developed by G. Bertsch.

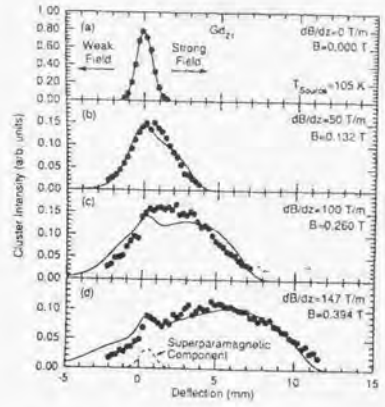

Figure 2.4: Deflection profile of Gd_{21} as a function of the magnetic field. The solid curves are the predictions of the locked moment model using $T_{rot} = 5.8$K $\mu = 2.56\mu_B$ per atom, and 4% of the clusters behaving superparamagnetically. The narrow peak in the solid curve near zero deflection in (d) is the 4% superparamagnetic component, show separately as the dashed curve.

N. Onishi, and K. Yabana [7]. They assume the magnetic field at the entrance of the magnet is adiabatic, which makes the calculation quite easier.

However, the interpretation of the peak around the zero deflection (Fig. 2.4) is still in controversy. D.C. Douglass, J.P. Bucher and L.A. Bloomfield considered that the Gd_{21} clusters are mixture of superparamagnetic clusters and locked moment clusters. The peak consists of superparamagnetic clusters including an ensemble of the Gd_{21} clusters [24]. Therefore they call it "superparamagnetic peak". On the other hand, G. Bertsch, N. Onishi, and K. Yabana considered that the peak results from the locked moment model. In fact, their calculation of locked moment profile reproduces the peak around zero deflection [7]. We review their model in the following, together with our calculation on the interpretation of the "superparamagnetic peak".

As mentioned in Introduction, in the locked moment model, the magnetic moment strongly couples with the cluster lattice; the magnetic moment is frozen to the cluster lattice. The model is the opposite limit to the superparamagnetism in which the magnetic moment is considered to be weakly coupled with the cluster lattice.

First we discuss the quantum mechanical treatment of the model. In the model, the

free magnetic clusters are rotating. The rotation of the cluster is characterized by the moment of inertia ($\mathcal{J}_i$) with respect to the body-fixed frame. The magnetic moment of the clusters ($\boldsymbol{\mu}$) is locked and couples with the magnetic field $\boldsymbol{B}$. The Hamiltonian of the locked moment model is described as

$$H = \sum_{i=1}^{3} \frac{J_i^2}{2\mathcal{J}_i} - \boldsymbol{\mu} \cdot \boldsymbol{B}, \tag{2.5}$$

where J_i means the i-th component of angular momentum of rotor J with respect to the body fixed frame ($i = 1, 2, 3$). For simplicity, we assume all the component of the moment of inertia are same.

$$\mathcal{J}_0 \equiv \mathcal{J}_1 = \mathcal{J}_2 = \mathcal{J}_3.$$

The bases for matrix elements are selected as the eigenstate of the free rotating axial symmetric rotor; $|JKM\rangle = \sqrt{\frac{2J+1}{8\pi^2}} \mathcal{D}^J_{MK}(\Omega)$, where M, K means the z- and 3-component of the angular momentum of the rotor, respectively.

The matrix elements of the Hamiltonian are evaluated as

$$\begin{aligned}\langle JKM|H|J'K'M'\rangle = \delta_{M,M'}\delta_{K,K'} \Bigg[& \frac{J(J+1)}{2\mathcal{J}_0}\delta_{J,J'} \\ & + \mu_0 B \left(\frac{2J'+1}{2J+1}\right)^{1/2} \langle J'K'10|JK\rangle\langle J'M'10|JM\rangle \Bigg],\end{aligned} \tag{2.6}$$

where the magnetic field B is applied along the z-axis. In the Stern-Gerlach magnet, the clusters feel the force which is proportional to the gradient of the magnetic field and the projection of the magnetic moment with respect to z-axis (magnetization). The strength of the force rapidly changes in the gradient magnet. The period of rotation is much smaller than the period that clusters pass through the Stern-Gerlach magnet. Then, we suppose the deflection of the clusters are proportional to the magnetization of each clusters. To calculate the profile, we diagonalize the matrix, and evaluate the magnetization of each state. The magnetization of each clusters can be evaluated by

$$\mu_i(B) = -\frac{dE_i}{dB}. \tag{2.7}$$

As discussed in the Introduction, the variation of the magnetic field at the entrance of the magnet is small enough to be regarded as adiabatic. Under the adiabatic condition, any transitions between energy levels do not occur even if the magnetic field is applied. Occupation probability of each state does not change during the flight. The clusters in

the source are supposed to be in the thermal equilibrium. Then the deflection profile is obtained by

$$P(\mu, B) = \frac{\sum_i \delta(\mu - \mu_i(B)) \exp[-J_i(J_i+1)/2\mathcal{J}_0 k_B T]}{\sum_i (2J+1)^2 \exp[-J(J+1)/2\mathcal{J}_0 k_B T]}. \tag{2.8}$$

The profiles are calculated numerically and show deflection to the strong field side. Though the profile calculated by G. Bertsch and K. Yabana did not show the peak around the zero-deflection point, our calculation for larger angular momentum reproduces the peak within the quantum treatment of the locked moment model.

The profile in the absence of the magnetic field is analytically calculated. For the Fe_{50} clusters of 15 K, which is a typical condition of the experiment, the root mean square of angular momentum is approximately equal to 200. Therefore, the summation for total angular momentum can be replaced by the integral;

$$\sum_i \approx \int_0^\infty dJ \int_{-J}^{J} dK \int_{-J}^{J} dM. \tag{2.9}$$

Therefore the profile in the absence of the magnetic field is calculated as

$$\mu_i = \mu_0 \langle JK10|JK\rangle\langle JM10|JM\rangle = \mu_0 \frac{MK}{J(J+1)}, \tag{2.10}$$

$$\begin{aligned} P(\mu, 0) &= \sum_i \mu_i \\ &\approx \int_0^\infty dJ \int_{-J}^{J} dK \int_{-J}^{J} dM \mu_0 \times \delta\left(\frac{MK}{J(J+1)}\right) \\ &= \frac{1}{2\mu_0} \ln(\mu_0/|\mu|), \end{aligned} \tag{2.11}$$

where μ_0 is the magnitude of the magnetic moment $\boldsymbol{\mu}$. The profile shows the divergence at $\mu = 0$.

Next, we calculate the magnetic field response using the perturbation theory for the magnetic field.

$$\langle i|\mu_z|i\rangle = 2B \sum J' \frac{\langle J_i K_i M_i|\mu_z|J_i' K_i M_i\rangle^2}{E_J - E_{J'}}. \tag{2.12}$$

Using the selection rule of the 1st rank tensor; $J' = J \pm 1$, average of the magnetization with a given value of J is found to be

$$\overline{\langle J|\mu_z|J\rangle} = \frac{B\mathcal{J}_0\mu_0^2}{36J^2}. \tag{2.13}$$

where, we use the Clebsch-Gordan coefficients;

$$\begin{aligned}\langle JM10|J-1\ M\rangle &= -\sqrt{\frac{J^2-M^2}{J(2J+1)}},\\ \langle JM10|J+1\ M\rangle &= \sqrt{\frac{(J+1)^2-M^2}{(J+1)(2J+1)}}.\end{aligned} \tag{2.14}$$

Putting (2.13) in the adiabatic statistical ensemble, and replacing the sum over J by an integral, we obtain for thermal expectation of the magnetization the expression

$$\frac{\langle\mu\rangle}{\mu_0} = \frac{2}{9}\frac{B\mu_0}{k_{\rm B}T}. \tag{2.15}$$

This differs from the superparamagnetic response,

$$\frac{\langle\mu\rangle}{\mu_0} = \frac{1}{3}\frac{B\mu_0}{k_{\rm B}T}. \tag{2.16}$$

by a factor of $\frac{2}{3}$. The dependence on temperature is proportional to $1/T$, which is the same as the superparamagnetism.

We next discuss the classical treatment of the locked moment model. We assume that the cluster have axial symmetry with respect to 3-axis and the magnetic moment is fixed to the direction of 3-axis. The Lagrangian of the locked moment model becomes

$$\mathcal{L}_{\rm sym} = \frac{\mathcal{J}_1}{2}(\dot\theta^2+\sin^2\theta\dot\phi^2) + \frac{\mathcal{J}_3}{2}(\dot\psi+\cos\theta\dot\phi)^2 + \mu_0 B\cos\theta, \tag{2.17}$$

where (θ,ϕ,ψ) are the Euler's angles [25]. We find the three constants of motion. One is the energy E given by,

$$E = \frac{\mathcal{J}_1}{2}(\dot\theta^2+\sin^2\theta\dot\phi^2) - \frac{\mathcal{J}_3}{2}(\dot\psi+\cos\theta\dot\phi). \tag{2.18}$$

Since the Lagrangian does not include ψ, the 3-component of angular momentum m_3 is conserved,

$$\frac{\partial\mathcal{L}_{\rm syn}}{\partial\dot\psi} = \mathcal{J}_3(\dot\psi+\cos\theta\dot\phi) = m_3. \tag{2.19}$$

The Euler angle ϕ is a cyclic coordinate which gives rise to the constant of motion; the z-component of angular momentum,

$$\frac{\partial\mathcal{L}_{\rm sym}}{\partial\dot\phi} = \mathcal{J}_1\sin^2\theta\dot\phi + m_3\cos\theta = m_z. \tag{2.20}$$

Eliminating $\dot\phi$ and $\dot\psi$ from Eqs. (2.18), (2.19) and (2.20), we obtain

$$\frac{\mathcal{J}_1}{2}\dot\theta^2 + U_{\rm eff}(\theta) = E', \tag{2.21}$$

where $U_{\rm eff}(\theta)$ and E' is defined as

$$U_{\rm eff}(\theta) = \frac{(m_z-m_3\cos\theta)^2}{2\mathcal{J}_1\sin^2\theta} - \mu_0 B\cos\theta, \tag{2.22}$$

$$E' = E - \frac{m_3^2}{2\mathcal{J}_3}. \tag{2.23}$$

Rearranging (2.21), we get

$$\int dt = \mathcal{J}_1\int\frac{d\theta}{\sqrt{2\mathcal{J}_1\{E'-U_{\rm eff}(\theta\}}}. \tag{2.24}$$

The expression is integrated from t_0 to t;

$$t-t_0 = -\mathcal{J}_1\int\frac{du}{\sqrt{f(u)}}, \tag{2.25}$$

$$f(u) = (e+hu)(1-u^2) - (m_z-m_3u)^2, \tag{2.26}$$

$$e = 2\mathcal{J}_1E' \quad\text{and}\quad h = 2\mathcal{J}_1\mu_0 B, \tag{2.27}$$

where $u=\cos\theta$. We set three solutions of $f(u)=0$ to $u_0<u_1<u_2$. For periodic solutions of the equation of motion, upper and lower limit of the integral are u_1 and u_2, respectively. The period of nutation can be evaluated as

$$\tau = 2\mathcal{J}\int_{u_1}^{u_2}\frac{du}{\sqrt{f(u)}}. \tag{2.28}$$

The average magnetization is calculated

$$\bar u = \frac{1}{\tau}\int_0^\tau\cos\theta dt = \frac{\int_{u_1}^{u_2}\frac{udu}{\sqrt{f(u)}}}{\int_{u_1}^{u_2}\frac{du}{\sqrt{f(u)}}}. \tag{2.29}$$

We assume that the variation of magnetic field is adiabatic. The adiabatic constant with respect to θ direction keeps constant during the flight and found to be

$$J_\theta = 2\int_{\theta_1}^{\theta_2}P_\theta d\theta = 2\int_{u_1}^{u_2}\frac{\sqrt{f(u)}du}{1-u^2}. \tag{2.30}$$

Therefore we can solve the motion of the cluster under the adiabatic field without integrating the equation of motion directly. The magnetization can be obtained using adiabatic constant, and found to be

$$\left(\frac{de}{dh}\right)_{J_\theta} = -\frac{\frac{\partial J_\theta}{\partial h}}{\frac{\partial J_\theta}{\partial e}} = -\bar u. \tag{2.31}$$

To consider the ensemble average, the volume of the phase space is

$$\int d\Omega = \frac{1}{2\pi}\int_{-\infty}^{\infty} dP_\theta \int_0^\pi d\theta \int_{-\infty}^{\infty} dm_z \int_0^{2\pi} d\phi \int_{-\infty}^{\infty} dm_3 \int_0^{2\pi} d\psi. \tag{2.32}$$

The volume can be rearranged to be

$$\frac{1}{\pi}\int_0^\infty dI \int_{-I}^{I} dm_z \int_{-I}^{I} dm_3 \int_{u_1}^{u_2} \frac{du}{\sqrt{(u_2-u)(u-u_1)}}, \tag{2.33}$$

where u and I^2 is defined as

$$u_{1,2} = \frac{m_3 m_z \pm \sqrt{(I-m_3)(I+m_3)(I-m_z)(I+m_z)}}{I^2}, \tag{2.34}$$

$$I^2 = P_\theta^2 + \frac{(m_z - m_3\cos\theta)}{\sin^2\theta} + m_3^2. \tag{2.35}$$

Hence the average of arbitrary physical quantity $\mathcal{O}$ is

$$\langle \mathcal{O} \rangle = \frac{1}{Z(\beta)}\int_0^\infty dI \int_{-I}^{I} dm_z \int_{-I}^{I} dm_3 \mathcal{O} \exp -\epsilon(I, m_3)/k_B T, \tag{2.36}$$

where $Z(\beta)$ is partition function;

$$Z(\beta) = \int_0^\infty dI \int_{-I}^{I} dm_z \int_{-I}^{I} dm_3 \exp\{-\epsilon(I, m_3)/k_B T\} \tag{2.37}$$

$$= 2\mathcal{J}_1\sqrt{2\pi\mathcal{J}_3}(k_B T)^{3/2}. \tag{2.38}$$

The physical quantity $\mathcal{O}$ changes according to the quantities we want to calculate. For example, we replace $\mathcal{O}$ to $\delta(u-\bar{u})$ to calculate profiles. To calculate magnetization, we set $\mathcal{O}$ to $\bar{u}$. The profile calculated by the locked moment model is illustrated in Fig. 2.5. We should note that the peak around $\bar{u}=0$ in the profile of $x=1$ is similar with the superparamagnetic peak observed in Gd_{21} clusters. In the locked moment model with quantum treatment of Ref. [6], the superparamagnetic peak is not reproduced because of the quantum effect. We check that the superparamagnetic peak is also produced in the quantum treatment for the large angular momentum.

The superparamagnetic peak mainly consists of the state of $M \simeq K \simeq 0$. Figure 2.6 illustrates the motion of the orbit calculated by the strong coupling limit of intermediate coupling model in the classical limit described in Sec. 3.2.2. The magnetic moment rotates about an axis perpendicular to the z-axis, which cause the average of the z-component of the magnetic moment to zero. When the magnetic field is applied, the orbit rotates with long period about the z-axis. Though the applied magnetic field slightly shift the range

of motion towards the direction of the magnetic field, it does not considerably affect the average of the magnetic moment. The magnetic moment stays the negative direction of the z-axis rather than the positive direction. The fraction of rotational energy becomes smaller when the magnetization is smaller. Then, the angular velocity decreases for smaller z. The period of the magnetic moment staying in $z<0$ is longer than that in $z>0$. Therefore, the average of magnetization shifts to the negative direction of z-axis.

The locked moment model have a possibility to describe the superparamagnetic peak without assuming the existence of superpramagnetic clusters.

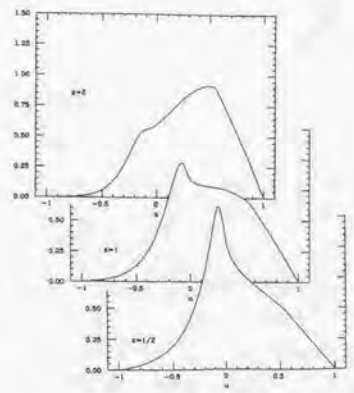

Figure 2.5: The profile calculated by the locked moment model with classical treatment. The scaling parameter $x = \frac{\mu B}{k_B T}$. We should note that the peak around $u=0$ in the profile of $x=1$ similar to the superparamagnetic peak observed in Gd_{21} cluster.

2.3 Experimental results

In this section we review the result of experiment for the 3d ferromagnetic metals, 4f elements, 4d transition metals which is non-magnetic in the bulk and alloys. We also give a short review of the bulk properties concerning the magnetism.

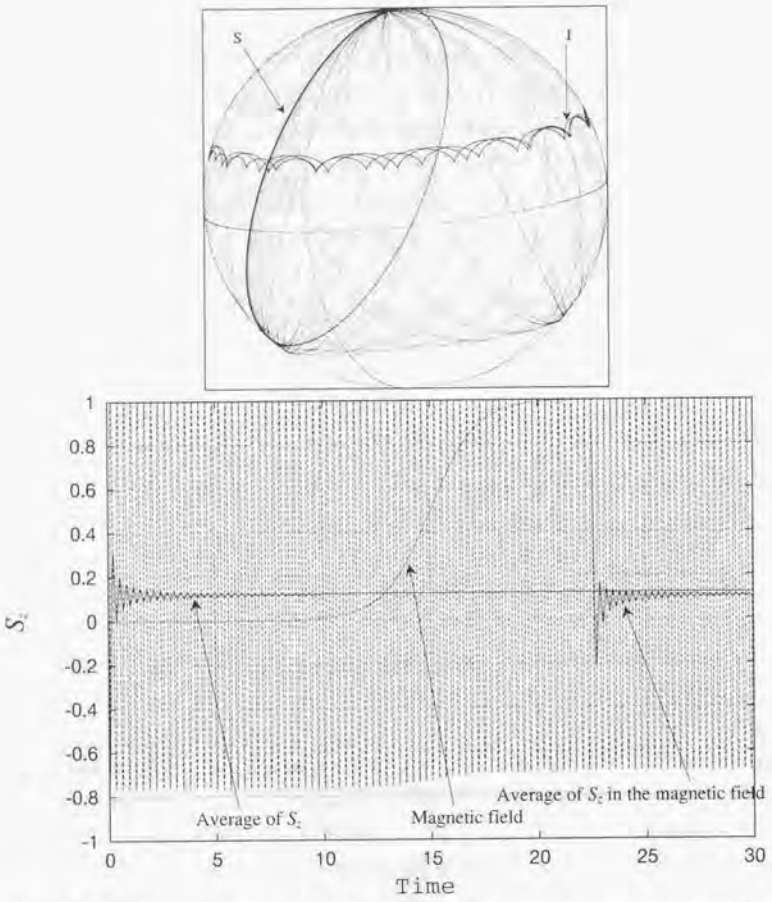

Figure 2.6: The upper figure represents the motion of magnetic moment and total angular momentum I in the space fixed frame for $I = 10, S = 1, M = 9.4, K = 9.4, u' = 10^4$ (see Sec.3.1 for the notations). The points means intersection between unit sphere and angular momentum vector in the space fixed frame. The lower figure is the time dependence of z-component of super-spin and the average of super-spin with and without magnetic field. Though the magnetic field makes range of motion narrow and shifts upwards, average of super-spin decrease.

2.3.1 3d transition metals

Iron, cobalt and nickel are familiar elements which show magnetism at room temperature. The critical temperature of magnetic-nonmagnetic transition (Curie temperature) is observed for bulk material of iron, cobalt and nickel as 1043, 1388 and 627 K, respectively. The magnetic moment of bulk iron, cobalt and nickel are $2.22\mu_B$, $1.72\mu_B$ and $0.606\mu_B$, respectively. The crystal structure of iron and nickel is body centered cubic (bcc) lattice with lattice constant 2.87 and 3.61 Å, respectively. Considering the symmetry of the crystal lattice, the magnetic anisotropy energy of iron and nickel as a function of orientation of magnetic moment has the same symmetry;

$$U_K = K_1(\alpha_1^2\alpha_2^2 + \alpha_2^2\alpha_3^2 + \alpha_3^2\alpha_1^2) + K_2\alpha_1^2\alpha_2^2\alpha_3^2, \tag{2.39}$$

where α_i's are direction cosine with respect to body fixed frame. Anisotropy constants K_1 and K_2 are known for iron

$$K_1 = 4.2 \times 10^6 \mathrm{erg/cm^3}, K_2 = 1.5 \times 10^6 \mathrm{erg/cm^3}. \tag{2.40}$$

The constants are much smaller for nickel,

$$K_1 = -4.5 \times 10^3 \mathrm{J/m^{-3}}. \tag{2.41}$$

For cobalt, its crystal structure is hexagonal close-packed (hcp) structure with lattice constant $a = 2.51\mu_B$ and $c = 4.07\mu_B$. Thus, magnetic anisotropy energy has an axial symmetry;

$$U_K = K_1' \sin^2\theta + K_2' \sin^4\theta, \tag{2.42}$$

where $\sin\theta$ is angle between symmetry axis and magnetic moment. The constant $K_1' = 0.33$[K/atom], $K_2' = 8.05 \times 10^{-2}$[K/atom].

Application of the Stern-Gerlach technique to clusters started from the experiment by D.M. Cox *et al.* to investigate the magnetic properties of iron clusters [10]. Up to now, the Stern-Gerlach experiment is performed for iron, nickel, cobalt, vanadium and chromium. The superparamagnetic behavior is observed for all kinds of elements.

The Stern-Gerlach experiment of iron clusters are firstly performed by D.M. Cox *et al.*[10]. The magnetic properties of iron clusters are extensively investigated by de Heer and coworkers [26]. Figure 1.1 shows the representative Stern-Gerlach profiles of clusters

with 120-140 atoms per cluster for several values of the deflecting field. The peak of profile moves toward the right direction with increasing field. The Stern-Gerlach experiment for nickel was performed by both de Heer group [12] and L.A. Bloomfield group [27].

Other 3d elements do not have spontaneous magnetization in the bulk matter. Especially, bulk vanadium is paramagnetic at all ranges of temperature, with a relatively temperature-independent susceptibility of about 5.8×10^{-6} emu/g at room temperature. The crystal structure of vanadium is body centered cubic (bcc). In the smaller systems of vanadium, the magnetic properties are not reveled, still in controversy. While Akoh and Tasaki observed magnetism in 90 to 300 Å particles [28], more recent experiments on thin films have yielded both positive and negative results for magnetism [29, 30]. A calculation for 15-atom vanadium cluster of the bcc structure shows that V_{15} should be non-magnetic at bulk lattice spacing. However, the cluster becomes magnetic changing lattice parameters larger. For V_9 clusters, magnetic moment is calculated as $2.89\mu_B$ per atom at bulk spacing. However, It abruptly disappears as the lattice spacing falls below 90% of the bulk spacing. The experiment on the non-magnetic clusters like vanadium was performed by L.A. Bloomfield and coworkers [31]. The results of experiment are described in the following sections.

Profile

The observed profiles of 3d transition elements are similar to cobalt, iron, nickel, and vanadium. A typical profile is shown in Fig. 2.7. The deflection is single-sided in contrast to the familiar Stern-Gerlach deflections of atoms. The peak move towards the right as increasing field. At the early stage of the study, this behavior seemed strange. Once the superparamagnetic theory of the clusters are proposed, these behaviors are considered to be a sign of the superparamagnetism.

Temperature dependence

The experiments to measure temperature dependence of the magnetization of clusters are performed by de Heer *et al.* for iron clusters, and by Bloomfield for cobalt, nickel, and vanadium clusters. The temperature dependence of magnetization of Bloomfield group is different from the result of the de Heer group. The magnetization of cobalt and nickel cluster investigated by L.A. Bloomfield *et al.* linearly depends on the $1/T$, where T is the source temperature. On the other hand, de Heer conclude that the measured magnetization increases as increasing temperature. Recalling the superparamagnetic model, the former result is readily explained. Bloomfield *et al.* regard the dependence as one of the evidence of justifying the superparamagnetic theory.

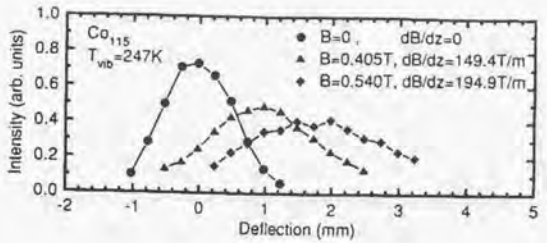

Figure 2.7: Typical deflection profiles of cobalt clusters. The temperature of the profiles is $T_{\rm vib} = 247$K. Profiles are averages of $\mathrm{Co}_{111-119}$.

We show an result of experiment by de Heer group of iron in Fig. 2.9. The magnetic field dependence of magnetization is not linear. The magnetization curve is S-shaped. The authors attribute the dependence to the electron spin resonance according to the anisotropic crystal field. The clusters in the beam rotate at frequency $\omega_{\rm rot}$. Assuming that the anisotropic crystal field has a cubic symmetry, the lowest frequency component of this perturbation is $4\omega_{\rm rot}$. The electron spin experiences a perturbation of this frequency. When the Larmor frequency is equal to rotational frequency, the electron spin shows the resonance. Therefore magnetization becomes small. P.J. Jensen and K.H. Bennemann investigate the resonance applying the Bloch equation which is a familiar method to explain the electron resonance [32, 33]. They explained the reversed temperature dependence and the S-shaped magnetic curve.

Magnetic moment

The magnetic moment of 3d transition metals has been extracted using superparamagnetic model. The temperature dependence and number dependence of the magnetic moment are obtained by the extensive Stern-Gerlach experiment. The temperature dependence of the magnetic moment is examined by de Heer and coworkers using the laser heating technique, which is the original feature of his apparatus. We show in Fig. 2.10 the results with the analysis using the Heisenberg model. Curve 1, 2, and 3 are the magnetization curves in

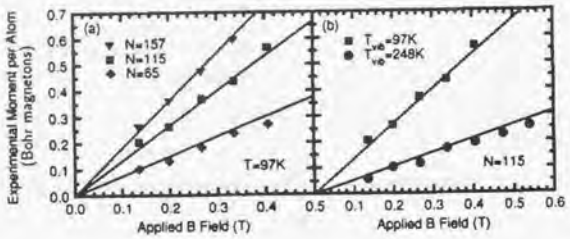

Figure 2.8: The magnetic field dependence of the magnetization for cobalt clusters. The field dependence is liner, which expected from both superparamagnetism and locked moment. Note that the experimental magnetic moment in the abscissa means the magnetization.

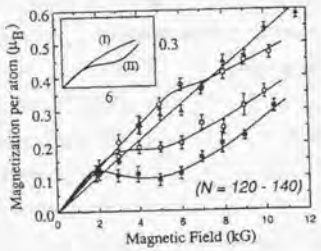

Figure 2.9: Anomalous temperature dependence of magnetization of the $Fe_{120-140}$clusters with $T_{source} = 300$K. Under the weak expansion $\tau = 3.0$ms, the curve is liner. For stronger conditions $\tau = 2.8$ms for open circles, $\tau = 2.5$ms open squares, and $\tau = 2.2$ms full squares, there are significant deviations from linearity.

the bulk iron, the Heisenberg model taking photon absorption statics into account, and the Heisenberg model including photon statics, respectively. For all curves the strength of exchange interaction is assumed to be the same in the bulk. They conclude that these data seem to strongly suggest that the Heisenberg model cannot be applied to small clusters.

Once we confirming that the clusters of 3d elements are superparamagnetic, we can examine the number dependence of the magnetic moment of the clusters. So far, Bloomfield and coworkers examined the number dependence for nickel clusters. Figure 2.11 shows the magnetic moment per atom as a function of the number of atoms in a cluster. They find the oscillation in the size dependence of the magnetic moment, which implies

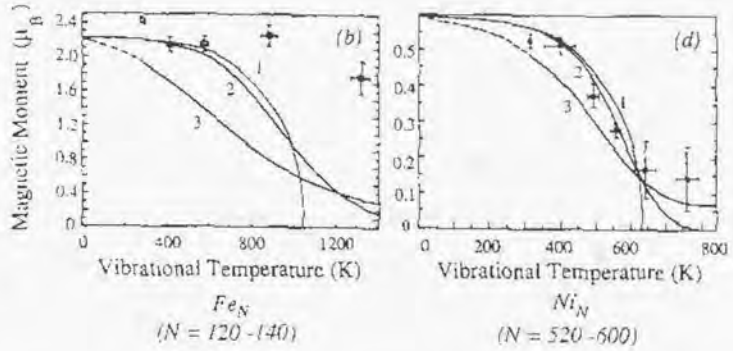

Figure 2.10: The extracted magnetic moment from the experiment assuming superparamagnetism. Curve (1) (2) and (3) are bulk magnetization curve, curve with absorption statics of photons are take into account, and Heisenberg model calculation with photon statics.

a shell effect for the magnetic moment. Two kinds of models are proposed to explain the shell structure. One is an approach from geometrical shell, another is an approach from an electronic shell.

In a single atom, the spin of valence electron aligned to make as large total spin as possible due to the Pauli principle. Thus, the magnetic moment of an atom is at maximum. The atoms in the clusters exchange valence 3d electrons with surrounding atoms, which broaden the width of 3d band. Then the magnetic moment is reduced as the number of surrounding atoms becomes larger. The magnetic moment of atom at a surface is enhanced because of the small coordination number. Because the significant number of atoms are at surface in the clusters, the enhancement of magnetization due to the surface atoms are important. In the approach in Refs. [34] and [35], they supposed the coordination number dependence of the magnetic moment of atoms. In addition, they assume the crystal structure of the clusters. Actually the results of the experiment show the minimum at $N = 13$. This can be explained that the clusters supposed to be a closed shell icosahedron, in which the coordination number of the atoms are largest for each atoms in the clusters. However, the minimum of magnetic moment at $N = 56$ cannot be explained by the simple geometrical model. According to the geometrical

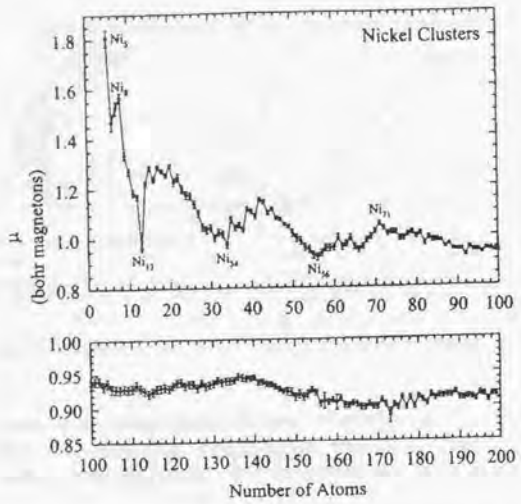

Figure 2.11: The shell structure of magnetic moment in nickel clusters.

model, magnetic moment of the clusters should be minimum for Ni_{55} of which the crystal structure is icosahedron.

Another model proposed by Fujima *et al.* [36] is based on the electronic structure of the clusters. According to the first-principle calculation of the nickel clusters of $N = 4, 6, 8, 14, 19$, the level scheme of the nickel clusters are constructed by two types of levels: a band like wide bunch of levels around a Fermi surface, and other narrow bunches of levels. The main component of the wide bunch comes from 3d atomic orbitals and one of the narrow bunch comes from the 4s component. Therefore we call the wide bunch "3d-band". Each levels spilt into major and minor components. Fermi level lies above the 3d-band and below the top of the minor component of 3d-band. The minor component of 3d-band is always filled. The magnetic moment per atom μ_N of a cluster is determined through the number of holes at the top of minor component of 3d band n_h as $\mu_N + \mu_\mathrm{B} n_\mathrm{h}$. The number of holes is related to the structure of 4s levels. Like conduction electrons of metals, 4s electrons of nickel atoms travels around the atoms in the clusters. They scattered only at a surface of the clusters. Then, the 4s electrons can be regarded as the

free electron in the cavity. In their paper, the states of 4s electrons are approximated to the state in the harmonic potential of which width is determined the number of the atoms. Increasing the number of the atoms in the clusters, the energy difference of the bunches of 4s levels close each other. The number of major shells below the 3d-band are increased. The first principle calculation suggests that the number of holes in the minor component of 3d-band n_h are the same as the number of 4s electrons. When the energy of the 4s bunch decreases and enters into below the 3d-band, magnetic moment per atom increases. Therefore, the magnetic moment oscillates as increasing the number of atoms in the clusters.

However the results of the calculation overestimate the amplitude of the oscillation. V.N. Kondratyev and H.O. Lutz proposed a hybrid model [37]. They consider a strong molecular self field H which originates from the exchange interaction of the electron in the cluster. Thus, the potential for the 4s electron is changed to $V(r) = m\omega^2 r^2/2 - \hbar\omega_\mathrm{L}/2$. The electronic shell structure of the 4s electrons are smeared out because of the self field. In this case the number of holes in the minor spin band is given by $n_\mathrm{h} = n_\mathrm{h}^0 - \delta n_\mathrm{s}$, with $n_\mathrm{h}^0 = 10 - (n_\mathrm{v} - n_\mathrm{s}^0)$, where n_v and n_s^0 are the numbers of the outer- and 4s-electrons per atom, respectively. The quantity δn_s^0 can be expressed through the contribution ρ_s of the 4s band to the level density active electrons,

$$\delta n_\mathrm{s} = (N_\mathrm{s}(\epsilon_\mathrm{F}) - N_\mathrm{s}(\epsilon_\uparrow))/N, \quad \text{where } N(\epsilon_i) = \int_{-\infty}^{\infty} d\epsilon \rho_\mathrm{s}(\epsilon) f(\epsilon - \epsilon_i), \tag{2.43}$$

where $\epsilon_\uparrow$ ($\epsilon_\downarrow$) means top energy of majority (minority) spin band. The Fermi function $f(x) = (1 + \exp(x/k_\mathrm{B}T)^{-1}$. To evaluate the density of state for the 4s electrons, they applied the semiclassical theory. The density of state is separated into smooth part ρ_s^sm and oscillation part ρ_s^sc. Each part can be expressed as

$$\rho_\omega^\mathrm{sm}(\epsilon) = \frac{\epsilon(\epsilon + \hbar\omega)}{2(\hbar\omega)^3}, \quad \rho_\omega^\mathrm{sc}(\epsilon) = \frac{\epsilon(\epsilon + \hbar\omega)}{2(\hbar\omega)^3} \sum_{k=1} \cos(2\pi k\epsilon/\omega) j_0(2\pi k\epsilon\eta/\omega) q_k. \tag{2.44}$$

The Larmor frequency $\omega_\mathrm{L} = eH/2mc$ satisfies the condition $\eta = \omega_\mathrm{L}/\omega \gg 1$. j_0 is the spherical Bessel function, and the factor q_k measures the stability of a trajectory; it permits a smooth truncation of the contribution from longer periodic orbits and can be chosen on the basis of the mean free path l or the conductivity of properties of the material as $q_k \simeq q^k$ with $q \simeq \exp(-L/l)$, where L measures the length of the primitive orbit. The oscillation

part can be calculated using the abbreviations $\Delta_\uparrow = \epsilon_F - \epsilon_\uparrow$, $\Delta_\downarrow = \epsilon_F - \epsilon_\downarrow$, $\Delta_s = \epsilon_F - \epsilon_s$,

$$\delta n_s^{sc} \simeq \frac{\Delta_\uparrow(1+X_s R)}{N(N\omega_s')4\pi\eta}\left[\arctan\left(\frac{q\sin(x)}{1-q\cos(x)}\right)\right]_{x=2\pi(1-\eta)X_s}^{x=2\pi(1-\eta)X_s}. \tag{2.45}$$

where $R = y\sinh(y)$ with $y = 2\pi k_B T/\omega_s$ and the quantity $X_s = (3n_s^0 N)^{1/3}$ counts the number of filled shells.

To take into account geometric shell, they assumed that total number 4s electrons are expressed as

$$n_s^0 \simeq n_s^{bulk} + n_s^{surf} N^{-1/3} + n_s^{curv} N^{-2/3}, \tag{2.46}$$

where n_s^{bulk}, n_s^{surf} and n_s^{curv} are contribution of 4s electrons by bulk, surface and curvature.

The results are compared to experimental data in Fig. 2.12. The shell model based on the band structure properties of strong ferromagnetic materials provides a better description of the magnetism of the ferromagnetic clusters.

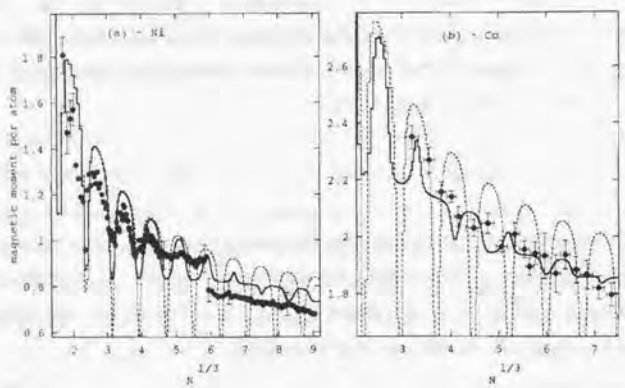

Figure 2.12: The theoretical curves for shell structure of magnetic moment. (a) free nickel clusters with $n_s^{bulk} = 0.62$ and [bulk:surf:curv]=[1:3.1:1.0];(b) free cobalt clusters with $n_s^{bulk} = 0.7$ and [bulk:surf:curv]=[1:3.1:2.1]. The solid lines display the results of the present calculations with a self-field $H = 0.7$T (a) and $H = 1.9$T (b). The dashed lines correspond to zero self field.

For vanadium clusters, the Stern-Gerlach experiment results in $0.59\mu_B$ for V_9 and $0.18\mu_B$ for V_{99} under the assumption of superparamagnetism [31]. In the analysis a cluster

vibrational temperature assumed to be the source temperature. The induced moment in 1 T field would be $0.0005\mu_B$ for bulk vanadium, well below the result of the experiment.

2.3.2 4f lanthanide

The solid of 4f lanthanide exhibit a variety of magnetic behaviors that are far richer than those of transition metals. The magnetic moment is formed by the localized 4f electrons. These electrons are interacted through the indirect exchange called RKKY interaction mediated by 6s and 5d band electrons. The interaction dependent on the distance from atom, which cause non-collinear structure of the magnetic moment. The anisotropic interaction is usually stronger than the 3d transition metals.

The profiles observed for gadolinium clusters are shown in Fig. 2.13. They observed two distinct behaviors. The profiles of Gd_{22} are single sided and are narrow Gaussian shape independent of the magnetic field, while the profiles of Gd_{23} are all broad, and their shapes depend on the applied field. The profiles of Gd_{17} resembles with that of Gd_{23} at the lowest temperature. At highest temperature, the profile of Gd_{17} resembles that of Gd_{22}. They interprets the result in the following way. The Gd_{22} clusters are assumed to be superparamagnetic, because their profiles are similar to the profile of cobalt, nickel, iron. The magnetic moment of Gd_{23} is assumed to be locked to the cluster lattice, because the profile similar with that of locked moment model. For the Gd_{17}, they suppose that the strength of coupling can be changed according with the temperature.

For the Gd_{22} clusters they present in the paper the result of analysis based on the superparamagnetism. As shown in Fig. 2.14, the experimental magnetization is proportional to the applied magnetic field. The magnetization is presented as a function of temperature and inverse of temperature in Fig. 2.15. The magnetization is not proportional to $1/T$. This fact contradicts to the superparamagnetism. They consider that the magnetic moment of Gd clusters changes with increasing temperature. The Curie temperature of Gd is 293 K which is far below the one of cobalt. Thus, the magnetic moment may change with the temperature range of experiment 97-247 K. The extracted moment based on superparamagnetism is presented in the Table 2.1. The result increases with the temperature. Though the trend is not explained ferromagnetic ordering, it can explained the Gd cluster is antiferromagnetic.

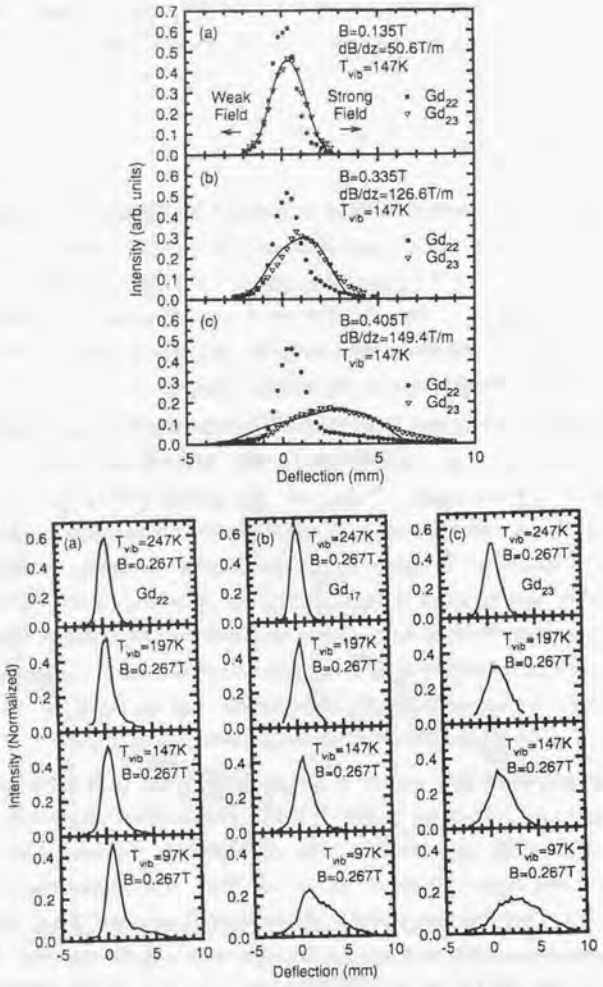

Figure 2.13: The profiles of gadolinium clusters. Typical behavior of superparamagnetism (Gd_{22}) and locked moment (Gd_{23}) are shown in upper figure. In the lower figure, the behavior of Gd_{17} is discussed. The profile of Gd_{17} resembles superparamagnetism for higher temperature, while it resembles locked moment in lower temperature.

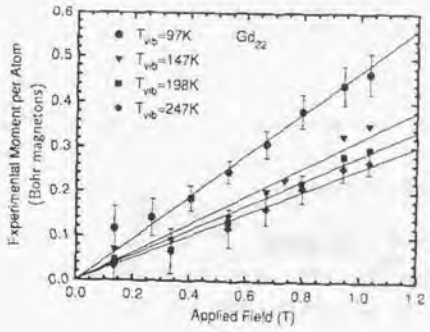

Figure 2.14: The magnetic field dependence of Gd_{22} clusters. The curve is linear except for $T_{\rm vib} = 97$K, which implies the moment couples with cluster lattice.

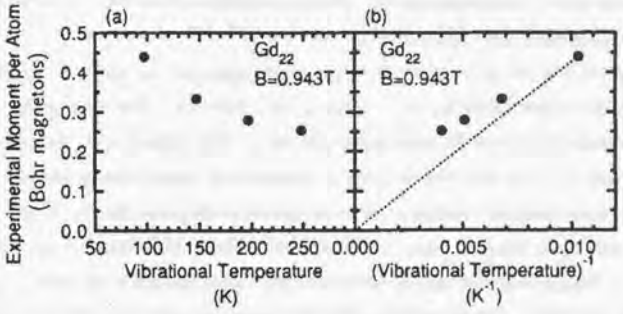

Figure 2.15: The temperature dependence of magnetization, which expected to be proportional to $1/T$ in the superparamagnetism. But this figure shows the magnetization is not proportional to $1/T$.

T_{vib}	μ
97 K	$2.94 \pm 0.35\mu_B$/atom
147 K	$3.33 \pm 0.40\mu_B$/atom
198 K	$3.65 \pm 0.44\mu_B$/atom
247 K	$3.88 \pm 0.47\mu_B$/atom

Table 2.1: The extracted magnetic moment of Gd_{22} clusters using superparamagnetism.

2.3.3 4d transition metals

The magnetic moment of 4d transition metals is discussed theoretically. Galicia calculated the magnetic moment of Rh_{13} using the molecular orbital approach [38]. This calculation supposed fcc cluster structure, which is structure of bulk rhodium, and bulk inter-atomic spacing. The predicted moment is $1.0\mu_B$ or $13\mu_B$ per atom. However, Galcia noted that the calculation may overestimate magnetic moment. Reddy, Khanna, and Dunlap recently predicted the magnetic moment of rhodium, ruthenium and palladium clusters of 13-atom by a variational calculation [39]. Their calculation assumed two types of crystal structures: icosahedral and fcc. The inter-atomic spacing is optimized by minimizing total energy. Their calculation predicted $1.6\mu_B$ per atom for icosahedral Rh_{13} and $1.46\mu_B$ per atom for fcc. They also predicted the magnetic moment of ruthenium and palladium clusters assuming icosahedral structure. The predicted moment is $1.02\mu_B$ and $0.12\mu_B$ per atom for Rh_{13} and Pd_{13}, respectively.

Applying the Stern-Gerlach technique, the magnetic moment of rhodium clusters Rh_{12-100} are investigated by Bloomfield *et al.* [40, 41]. The estimation of the magnetic moment based on the superparamagnetic model. Figure 2.16 shows the magnetic moment per atom with a cluster size. In addition to overall decreasing in μ as increasing size, some rhodium clusters exhibit anomalously large values for μ. Rh_{15}, Rh_{16}, and Rh_{19} appear to be unusual magnetic. The extraordinary size dependence of μ in rhodium clusters indicates that the cluster structure itself is important in the enhancement of the magnetic moment. They concluded that the magnetic moment is less than $0.40\mu_B$ per atom for Rh_{13} and less than $0.13\mu_B$ for Rh_{105}.

Ruthenium and palladium clusters of 12 to more than 100 are also investigated by Bloomfield *et al.* [31, 41]. Ruthenium clusters show magnetism like palladium. The magnetic moment of Ru_{10} and Ru_{115} is smaller than $0.32\mu_B$ and $0.09\mu_B$, respectively. The magnetic moment of palladium is estimated as $0.000 \pm 0.014\mu_B$ for number of atoms

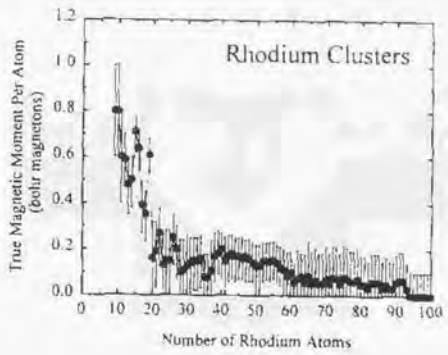

Figure 2.16: The extracted magnetic moment of rhodium clusters.

$N = 100 - 120$.

2.3.4 Alloys

The only one Stern-Gerlach experiment for alloy is performed by T. Hihara, S. Pokrant and J. A. Becker for $Bi_N Co_M$ clusters [42]. The experimental apparatus is almost the same as the other Stern-Gerlach experiments, except for the source. Their source is illustrated in Fig. 2.17. The Bi_N and Co_N clusters are generated in two independent regions of the apparatus. Bi_N or Co_N is evaporated from a rotating rod by a Nd:YAG laser beam, is cooled by helium atmosphere in each source. These two clusters are carried by the helium flow and mixed in a reaction chamber, where $Bi_N Co_M$ clusters are generated.

The deflection behaviors are similar to the deflection of Fe_N, Co_N or Ni_N clusters. Therefore they analyze their experimental data based on the superparamagnetism.

Their result for the $Bi_N Co_M$ ($M \leq 5, N \leq 10$) is shown in Fig. 2.18. The electronic configuration of cobalt atom is known to be $4s^2 3d^7$. However the Co_N clusters, electronic configuration gradually changes to $4s^1 3d^8$ which is the configuration of the solid phase of cobalt. For the Bi_N clusters, they confirmed by their Stern-Gerlach experiment that the Bi_N clusters are nonmagnetic, reflecting the diamagnetic property of bulk bismuth. If the magnetic moment of $Bi_N Co_M$ clusters originates from the electron spin of cobalt

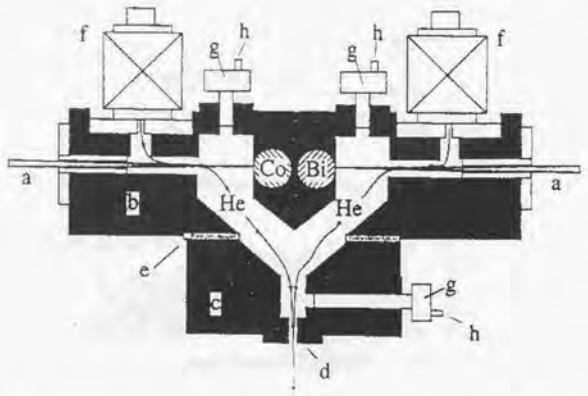

Figure 2.17: The source for creating Bi_NCo_M alloy. Cobalt and bismuth are generated independently with two sources. Each clusters are carried by the helium flow and mixed together to make Bi-Co binding.

with bulk configuration, the magnetic moment is described as $\mu_{\rm eff} = g_s\sqrt{S(S+1)}\mu_{\rm B}$. The gyromagnetic factor $g_{\rm eff}$ is approximately equal to 2. This approximation for the magnetic moment is called as "ferromagnetic spin only approximation". In Fig. 2.18, the magnetic moment predicted by the ferromagnetic spin only approximation is denoted by solid line. The results of mixed clusters Bi_NCo_M with $M \geq 3$ are roughly described by the ferromagnetic spin only approximation. However, for some species, the results are smaller than the approximation, especially $M = 5$. They propose that this reduction indicates the influence of the Bi_N-Co_5 bonds on the Co_5 cluster component.

The results of $M = 2$ can not be understood within the simple ferromagnetic spin only approximation. This indicates that the orbital angular momentum contributes to the magnetic moment of the clusters. They suppose that the Bi_NCo_M clusters consists of Bi_N cluster and Co_2 diatomic molecule. For $D_{\infty h}$ symmetric molecule like Co_2, orbital angular momentum does not quenched, and contributes to the magnetization about a internuclear Co-Co axis. They estimate contribution of orbital angular momentum by fitting experimental data. The results show odd-even staggering with respect to the number of valence electrons in the Bi_N unit.

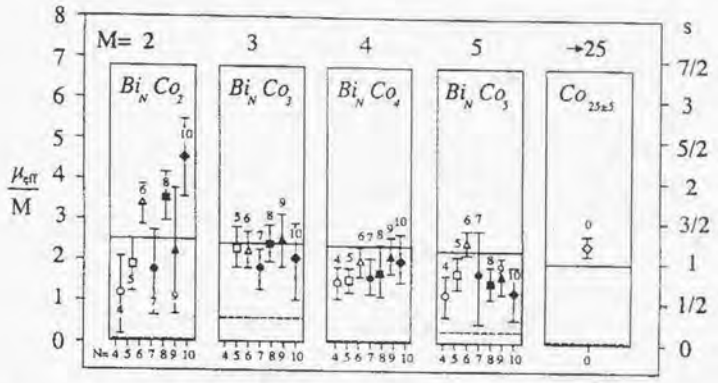

Figure 2.18: Magnetic moment of the clusters per cobalt atom as a function of the number M of cobalt atoms in the clusters. The analysis of experiment is based on the superparamagnetism.

Chapter 3

The Intermediate coupling model

As seen in the previous chapter, the superparamagnetism and locked moment models seem to succeed to extract the magnetic moment of the iron and gadolinium clusters, respectively. However the profiles cannot be explained by the superparamagnetism in which only the average is needed for analysis of the profile. The angular momentum of magnetic moment do not take into account in the locked moment model. Some gadolinium cluster like Gd_{17} can not be analyzed by both locked moment model and superparamagnetism. In this chapter, we propose the intermediate coupling model, in which the super-spin couples the rotation through the magnetic anisotropy energy.

3.1 The Intermediate coupling model

In the present model it is supposed that all the electron spins are aligned in the same direction through the exchange interaction. Thus, the electron spins are in stretched coupling states having a giant total spin $S = \frac{1}{2}n_s N$, where n_s is the number of spins participating the magnetic moment an atom. Since the magnetic moment is proportional to the total spin, the cluster has a single giant magnetic moment expressed as $\mu = g_s S$, in terms of the electronic gyromagnetic ratio g_s.

Consider as a typical case the Fe_{100} cluster at temperature 100 K. According to Kittel [43], the magnetic moment per atom for the bulk iron is $2.2\mu_B$. Then a spin value of $S \simeq 2.2 \times 100 \times 1/2 \simeq 100$ and a thermal rotational angular momentum $R \simeq 600$ in units of $\hbar$. These large values of S and R justify a classical treatment of the problem. In fact, in Sec. 2.2.2 the classical treatment allowed the problem to be reduced to a simple and transparent calculation. This was examined for a simple case, by utilizing adiabatic invariance which makes the calculation easy and transparent.

The formulation of our model is indebted to the theory of deformed nuclei, especially the particle-rotor model; readers who want to know the theory can consult standard textbooks on nuclear structure, e.g., Bohr and Mottelson [44].

Our Hamiltonian H is expressed as a sum of three terms:

$$H = H_{\rm rot} + H_{\rm coupl} + H_{\rm mag}, \tag{3.1}$$

where the terms are defined as follows. The first term $H_{\rm rot}$ stands for the rotational energy of the cluster which is expressed as

$$H_{\rm rot} = \sum_{i=1}^{3} \frac{\hat{R}_i^2}{2\mathcal{J}_i}, \tag{3.2}$$

where $\hat{R}_i$'s represent operators of three angular momentum components referred to the body fixed frame, and $\mathcal{J}_i$'s express principal moments of inertia. The vibrational modes are not taken into account, because the Debye temperature (for instance, 500[K] for iron) is much higher than the source temperature. In other words, the rotational motion is considered to work mainly as a heat bath in the spin relaxation.

The second term $H_{\rm coupl}$ expresses a coupling potential between the cluster and the super-electron spin, which originates from the crystal magnetic anisotropy energy caused by molecular or crystal fields. The simplest form of the energy is the uniaxial magnetic anisotropy, which has already been examined in Ref. [8]. We discuss the coupling potential of uniaxial and cubic symmetry in the following.

The uniaxial magnetic anisotropy is observed in the bulk gadolinium and cobalt reflecting symmetry of its crystal structure. The anisotropy constant is measured in the form

$$U_K = K_1' \sin^2\theta + K_2' \sin^4\theta, \tag{3.3}$$

where $\sin\theta$ is angle between symmetry axis and magnetic moment. The coefficient K_1' and K_2' are observed in cobalt clusters as $K_1' = 0.33$ [K/atom], $K_2' = 8.05 \times 10^{-2}$ [K/atom]. We neglect second term of the anisotropic energy in (3.3). The classical form of the anisotropic interaction is written in the components of the super-spin with respect to intrinsic frame S_i.

$$H_{\rm coupl} = uS'^2 \left(\sin^2\theta - \frac{2}{3}\right) \tag{3.4}$$

$$= -\frac{2}{3} u C_0^{(2)}(S'), \tag{3.5}$$

where u is defined through the relation $K_1' = uS'^2$. In quantum Hamiltonian, $\boldsymbol{S}'$ are operators and we are interested in their matrix elements. The reduced matrix element obtained through the Wigner-Eckart theorem is expressed by

$$\langle S || \left[\hat{S}\right]^L || S \rangle = \left(\frac{1}{2}\right)^L \sqrt{\frac{(2S+L+1)!}{(2S-L)!}}. \tag{3.6}$$

For example, for $L = 1$, one obtains the familiar form $\sqrt{S(S+1)(2S+1)}$. The coupling potential is

$$H_{\rm coupl} = -\frac{2}{3} u \mathcal{D}^{2*}_{m0}(\Omega) \left[S^2\right]^2_m. \tag{3.7}$$

Because the coupling Hamiltonian is scalar, the total angular momentum $\boldsymbol{I} = \boldsymbol{R} + \boldsymbol{S}$ is a good quantum number. In addition, the 3-component of rotational angular momentum R_3 is conserved because of the axial symmetry of the potential. The basis are obtained

$$\Psi_{\nu I M k} = \sum_{R\sigma} \langle R\mu S\sigma | IM \rangle \, \mathcal{D}^R_{\mu k}(\Omega) f^{\nu I}_R \, |S\sigma\rangle, \tag{3.8}$$

The matrix element can be estimated as

$$(H_{\rm coupl})^{Ik}_{R,R'} = -u' \sqrt{(2R+1)(2S+1)} (-1)^{S+R'-I} \times \langle Rk20 | R'k \rangle \, W(RSR'S; I2), \tag{3.9}$$

where $u' = \frac{2u\langle S||\left[\hat{S}\right]^2||S\rangle}{3\sqrt{2S+1}}$ which is used in our numerical calculation, the Racah coefficient $W(abcd; ef)$ is related to the $6j$ symbol [45].

For iron or nicked clusters, we assume that the clusters have an internal cubic structure and the potential has cubic symmetry. This is true for observation of the direction of easy magnetization being [100], [010] and [001] for iron and nickel. The anisotropy constant is measured in the form

$$E_\alpha = K_1(\alpha_1^2\alpha_2^2 + \alpha_2^2\alpha_3^2 + \alpha_3^2\alpha_1^2) + K_2\alpha_1^2\alpha_2^2\alpha_3^2 + \cdots, \tag{3.10}$$

where α_i's express the direction cosines of super-electron spin. The observed values in the bulk are $K_1 = 36$ [mK/atom] and $K_2 = 13$ [mK/atom] for iron, and $K_1 = -4$ [mK/atom] and $K_2 = 0$ [mK/atom] for nickel. We consider only the first term in the present calculation. In order to formulate the anisotropic interaction, let us start with

the above classical picture for angular momentum variables, in which S_i's commute:

$$\begin{aligned} H_{\rm coupl} &= 8uS'^4(\alpha_1^2\alpha_2^2+\alpha_2^2\alpha_3^2+\alpha_3^2\alpha_1^2-\frac{1}{5}) \\ &= -u\left\{S_1'^4+S_2'^4+S_3'^4-6(S_1'^2S_2'^2+S_2'^2S_3'^2+S_3'^2S_1'^2)\right. \\ &\quad \left.+\frac{3}{5}(S_1'^2+S_2'^2+S_3'^2)^2\right\} \\ &= -uS'^4\sqrt{\frac{32}{35}}\left\{C_4^{(4)}(\hat{\boldsymbol{S}})+C_{-4}^{(4)}(\hat{\boldsymbol{S}})+\sqrt{\frac{14}{5}}C_0^{(4)}(\hat{\boldsymbol{S}})\right\}. \end{aligned} \tag{3.11}$$

Here $C_\mu^{(\lambda)}(\hat{\boldsymbol{S}})$ stands for the spherical harmonic proportional to $Y_{\lambda\mu}(\hat{\boldsymbol{S}})$: S_i' is the spin component with respect to the three axes in the body-fixed frame, S_i denotes the spin component referred to the laboratory system, and $u = 2K_1/n_s^4N^3$. The electron spin prefers the direction of four-fold axes of the cubic symmetry. When the direction of the spin is along the four-fold axes, the value of $H_{\rm coupl}$ has a minimum energy $-\frac{8}{5}uS'^4$. And when the direction of the spin is along the eight axes of $(\pm\frac{1}{\sqrt{3}}\pm\frac{1}{\sqrt{3}}\pm\frac{1}{\sqrt{3}})$ represented by the body-fixed coordinate, the value of $H_{\rm coupl}$ turns out to be the energy maximum $\frac{16}{15}uS'^4$. In the quantum Hamiltonian, $\boldsymbol{S}'$ are operators and we are interested in their matrix elements. The interaction between the rotor and the super-electron spin in Eq. (3.11) is given by

$$H_{\rm coupl}(\boldsymbol{S},\Omega) = \sum_{\kappa,m}\left[S^4\right]_m^4\mathcal{D}_{m\kappa}^{4*}(\Omega)A_\kappa, \tag{3.12}$$

where κ takes the values of only 0 and ±4 and $A_{\pm4} = \sqrt{5/14}A_0 = -u\sqrt{32/35}$. The wave function of the rotor can be expanded in terms of the $\mathcal{D}$ functions [44],

$$\phi_{R\mu}(\Omega) = \sum_k f_{Rk}\mathcal{D}_{\mu k}^R(\Omega). \tag{3.13}$$

Since the Hamiltonian $H_{\rm coupl}$ is again scalar, the total angular momentum $\boldsymbol{I}$ is a good quantum number for the first two terms of the Hamiltonians, $H_{\rm rot}+H_{\rm coupl}$. Accordingly, we select the base labeled by the total angular momentum and magnetic quantum number I_z. The basis is obtained by the angular momentum coupling of the $\mathcal{D}$ function $\mathcal{D}_{\mu k}^R(\Omega)$ and $|S\sigma\rangle$ to $|IM\rangle$. Therefore, the total wave function of the rotor coupled with the super-electron spin is expressed as

$$\Psi_{\nu IM} = \sum_{Rk\sigma}\langle R\mu S\sigma|IM\rangle\,\mathcal{D}_{\mu k}^R(\Omega)f_{Rk}^{\nu I}\,|S\sigma\rangle\,, \tag{3.14}$$

where ν represents an index specifying states having the same IM. The matrix element of the coupling term between the bases in Eq. (3.14) is estimated as

$$\begin{aligned} (H_{\rm coupl})_{Rk,R'k'}^I &= \sqrt{(2R+1)(2S+1)}(-1)^{S+R'-I} \\ &\quad A_\kappa'\langle Rk4\kappa|R'k'\rangle\,W(RSR'S;I4), \end{aligned} \tag{3.15}$$

where $\sqrt{2S+1}A_\kappa' = A_\kappa\langle S||\left[\hat{S}\right]^4||S\rangle$.

In our calculation we use the potential strength parameter $u' = A_{\pm4}'$. Now, the wave function (3.14) and the energy in the source are determined by diagonalizing $H_{\rm rot}+H_{\rm coupl}$. Since there remains the $(2I+1)$-fold degeneracy in energy for M, we may omit M from the label for the energy $E_{\nu I}$.

The third term in Eq. (3.1) represents the interaction between an external magnetic field and the moments of the super-electron spin

$$H_{\rm mag} = -\boldsymbol{B}\cdot\boldsymbol{\mu} = -Bg_{\rm s}\hat{S}_z. \tag{3.16}$$

We choose the direction of the applied magnetic field as the axis of quantization (z axis). This interaction breaks rotational symmetry for the cluster, but the magnetic quantum number M defined above is still conserved due to the choice of quantization axis. From Eqs. (3.14) and (3.16), the matrix elements between two states are calculated as

$$\langle\Psi_{\nu IM}|H_{\rm mag}|\Psi_{\nu'I'M}\rangle = -Bg_{\rm s}\hbar\sqrt{2I'+1}(-1)^{I'}\langle I'M10|IM\rangle\,h_{\nu I\nu'I'}, \tag{3.17}$$

where the M-independent part $h_{\nu I\nu'I'}$ is expressed as

$$h_{\nu I\nu'I'} = \sum_{Rk}f_{Rk}^{\nu I*}f_{Rk}^{\nu'I'}\sqrt{S(S+1)(2S+1)}(-1)^{R-S+1}W(ISI'S;R1). \tag{3.18}$$

For the quadrupole coupling, the projection of angular momentum of rotor R with respect to 3-axis is conserved. Therefore the matrix element of $H_{\rm mag}$ can be calculated using Eq. (3.8) as

$$\begin{aligned} \langle\Psi_{\nu kIM}|H_{\rm mag}|\Psi_{\nu'k'I'M}\rangle &= -Bg_{\rm s}\hbar\sqrt{2I'+1}(-1)^{I'+R-S+1}\langle I'M10|IM\rangle \\ &\quad \sum_{Rk\mu}f_R^{\nu I*}f_R^{\nu'I'}\sqrt{S(S+1)(2S+1)}W(ISI'S;R1). \end{aligned} \tag{3.19}$$

For simplicity, we set the moment of inertia around the intrinsic axes to take the same value, namely, $\mathcal{J}_1 = \mathcal{J}_2 = \mathcal{J}_3 = \mathcal{J}$. In this case, total wave functions are classified

by an additional quantum number $\pi_k = 0, 1, 2, 3$ (k mod 4), since $H_{\rm rot}$ is diagonal and $H_{\rm coupl}$ couples to only the states having k quantum numbers different by 4. This point is different from uniaxial anisotropy, in which k quantum number is strictly conserved due to the axial symmetry. The total wave functions in the magnetic field are expressed as

$$|\Phi_{\alpha\pi_k M}(B)\rangle = \sum_{\nu I} F^{\nu I}_{\alpha\pi_k M}(B)\,|\Psi_{\nu I\pi_k M}\rangle\,, \tag{3.20}$$

where α labels the state in the same π_k, M.

To compare with the experiment, we calculate the average magnetization, which we regard as the ensemble average of $\langle \hat{S}_z \rangle$. This is the sum of the product of the expectation value of $\hat{S}_z$ and the occupation probability of each state. Now we proceed ahead with the important assumption that effect of the magnetic field is adiabatic when the cluster passes through Stern-Gerlach magnet. The variation of the magnetic field is slow when the cluster enters into and goes out from the Stern-Gerlach magnet. First the clusters are retained in the source region. In this region, as the cluster ensemble is in thermal equilibrium, the occupation probability of each quantum state is proportional to the Boltzmann factor $\exp(-E_{\nu I\pi_k}/k_{\rm B}T)$, where $E_{\nu I\pi_k}$ is the energy in the source.

The magnetization of each state in Eq. (3.20) is calculated as

$$S_{z,\alpha(\nu I)\pi_k M}(B) = \langle \Phi_{\alpha(\nu I)\pi_k M} \mid \hat{S}_z \mid \Phi_{\alpha(\nu I)\pi_k M} \rangle, \tag{3.21}$$

where $\alpha(\nu I)$ stands for the label of states connected adiabatically with the states (νI) defined in the absence of a magnetic field.

Under the adiabatic condition, any transition between energy levels does not occur even if a magnetic field is applied. The occupation probability of each quantum state is not altered during the flight. Then the deflection profile is obtained by

$$P(s, B, T) = \frac{1}{Z(T)} \sum_{\nu I \pi_k M} \delta(s - S_{z,\alpha(\nu I)\pi_k M}) \exp\left(\frac{-E_{\nu I\pi_k}}{k_{\rm B}T}\right), \tag{3.22}$$

where the partition function $Z(T)$ is given by

$$Z(T) = \sum_{\nu I \pi_k} (2I+1) \exp\left(\frac{-E_{\nu I\pi_k}}{k_{\rm B}T}\right). \tag{3.23}$$

According to Eq. 3.22, the profile is constructed by many spikes. However, smooth profile is observed because of cluster beam being spread. Then, we smear the spikes by the Gaussian function of which width is set to $0.01S$.

The magnetization, the ensemble average $\langle \hat{S}_z \rangle_{\rm enav}$, is expressed by

$$\langle \hat{S}_z \rangle_{\rm enav} = \int s P(s, B, T) ds. \tag{3.24}$$

3.2 Classical limit of the intermediate coupling model

Though the classical mechanics does not play a role as a fundamental theory after the birth of the quantum mechanics, it is still meaningful in giving an intuitive interpretation of quantum states. In this section, we discuss the classical limit of the intermediate coupling model to interpret the results which will be obtained using the quantum theory. In the intermediate coupling model, the rotor is coupled with the super-spin. To describe the classical motion of the spin, we apply the boson representation of the angular momentum. There are three kinds of representation of angular momentum, Holstein Primackoff [46], Dyson [47] and Schwinger [48] representation. In the intermediate coupling model, the magnitude of angular momentum of the rotor does not conserve because of the anisotropic coupling. Only the Schwinger representation of angular momentum can represent the mixing of states which have different magnitude of angular momentum with two kinds of bosons. Therefore, in the following, we describe the Schwinger representation of the angular momentum.

3.2.1 The Schwinger boson representation of angular momentum

The boson representation of angular momentum is a composite operator of bosons which fulfill the commutation relations of angular momentum operators. Schwinger introduced the boson representation of the angular momentum operators using two bosons $\tilde{A}$ and $\tilde{B}$,

$$[\tilde{A}, \tilde{A}^\dagger] = 1, \quad [\tilde{B}, \tilde{B}^\dagger] = 1, \quad [\tilde{A}, \tilde{B}] = [\tilde{A}, \tilde{B}^\dagger] = 0, \tag{3.25}$$

which act in a space of two-dimensional oscillator states

$$|n_A n_B) = \frac{1}{\sqrt{n_A! n_B!}} (\tilde{A})^{n_A} (\tilde{B})^{n_B} |0\,0). \tag{3.26}$$

The Schwinger representation is given by

$$\begin{aligned} \tilde{J}_+ &\to (\tilde{J}_+)_B = \tilde{B}^\dagger \tilde{A}, \\ \tilde{J}_- &\to (\tilde{J}_-)_B = (J_+)^\dagger_B = \tilde{A}^\dagger \tilde{B}, \\ \tilde{J}_z &\to (\tilde{J}_z)_B = \frac{1}{2}(\tilde{B}^\dagger \tilde{B} - \tilde{A}^\dagger \tilde{A}). \end{aligned} \tag{3.27}$$

These operators fulfill the commutation relations of angular momentum (A.1). The eigenstates of the angular momentum operators can be written as

$$|IM) = \frac{(\hat{B}^\dagger)^{I+M}(\hat{A}^\dagger)^{I-M}}{[(I-M)!(I+M)!]}|0\rangle. \tag{3.28}$$

In this space, a generating operator of a state $|L+l\ L_0+m\rangle$ from $|L\ L_0\rangle$ ($\hat{E}(lm)$) can be given as

$$\hat{E}(lm)|LL_0\rangle = |L+l\ L_0+m\rangle, \tag{3.29}$$

$$\hat{E}(lm) = \hat{\xi}(l+m)\cdot\hat{\eta}(l-m), \tag{3.30}$$

where $\hat{c}(n)$ is given by

$$\hat{c}(n) = \begin{cases} (\hat{c}^\dagger\frac{1}{\sqrt{N+1}})^n, & (n \geq 0), \\ (\frac{1}{\sqrt{N+1}}\hat{c})^{-n}, & (n \leq 0). \end{cases} \tag{3.31}$$

In the quantum mechanics of the rotor used in the intermediate coupling model, we introduce the body-fixed frame and component of angular momentum from the frame. As we describe in the Appendix A.1, the angular momentum algebra in the body fixed frame is different from the one in the space-fixed frame by sign. Therefore we describe the extend Schwinger boson representation to describe the quantized rotator introduced by M. Yamanura, T. Suzuki and H. Ichihasi [49, 50].

The quantized free rotator have three constant of motion; the total angular momentum, the z-component of angular momentum and the 3-component of angular momentum. Therefore it may be reasonable to introduce four kinds of boson operators: $(\hat{A}, \hat{A}^\dagger)$, $(\hat{B}, \hat{B}^\dagger)$, $(\hat{b}, \hat{b}^\dagger)$ and $(\hat{a}, \hat{a}^\dagger)$ which is mutually commutable.

$$\hat{s} = \frac{1}{2}(\hat{B}^\dagger\hat{B} + \hat{A}^\dagger\hat{A} - \hat{b}^\dagger\hat{b} - \hat{a}^\dagger\hat{a}), \tag{3.32}$$

$$\hat{J} = \frac{1}{2}(\hat{b}^\dagger\hat{b} + \hat{a}^\dagger\hat{a}), \tag{3.33}$$

$$\hat{J}_0 = \frac{1}{2}(\hat{B}^\dagger\hat{B} - \hat{A}^\dagger\hat{A}), \tag{3.34}$$

$$\hat{J}'_0 = \frac{1}{2}(\hat{b}^\dagger\hat{b} - \hat{a}^\dagger\hat{a}). \tag{3.35}$$

The eigenstate of $\hat{S}, \hat{J}, \hat{J}_0$ and $\hat{J}'_0$ with corresponding eigenvalue S, J, J_0 and J'_0 is given by

$$|SJJ_0J'_0\rangle = \frac{(\hat{B}^\dagger)^{S+J+J_0}(\hat{A}^\dagger)^{S+J-J_0}(\hat{b}^\dagger)^{J+J'_0}(\hat{a}^\dagger)^{J-J'_0}}{(S+J+J_0)!(S+J-J_0)!(J+J'_0)!(J-J'_0)!}|0\rangle \tag{3.36}$$

S	J	J_0	J'_0
i	i	i	i
i	h	h	h
h	i	h	i
h	h	i	h

Table 3.1: Possible conbinations of the label of the angular momentum. i and h means integer and half-integer, respectively.

where $|0\rangle$ denotes the boson vacuum. Because the boson number and the powers of each boson operator should be positive integers or zero, we get $2(S+J)$, $2J$ and $S+J+J_0$, $S+J-J_0$, $J+J'_0$, $J-J'_0$ are positive. Therefore, S, J, J_0 and J'_0 should obey the following conditions:

$$S = -J, -J+1/2, -J+1, \cdots, -1/2, 0, 1/2, 1, \cdots, \tag{3.37a}$$

$$J = 0, 1/2, 1, 3/2, \cdots, \tag{3.37b}$$

$$J_0 = -S-J, -S-J+1, \cdots, S+J-1, S+J, \tag{3.37c}$$

$$J'_0 = -J, -J+1, \cdots, J-1, J. \tag{3.37d}$$

We introduce following operators in addition to $\hat{s}, \hat{J}, \hat{J}_0$ and $\hat{J}'_0$:

$$\hat{J}_{+1} = -\frac{1}{2}\hat{B}^\dagger\hat{A}\frac{\sqrt{(J-J_0)(J+J_0+1)}}{\sqrt{(S+J-J_0)(S+J+J_0+1)}}, \tag{3.38}$$

$$\hat{J}_{-1} = \frac{1}{2}\hat{A}^\dagger\hat{B}\frac{\sqrt{(J+J_0)(J-J_0+1)}}{\sqrt{(S+J+J_0)(S+J-J_0+1)}}, \tag{3.39}$$

$$\hat{J}'_{+1} = -\frac{1}{2}\hat{a}^\dagger\hat{b}, \quad \hat{J}'_{-1} = \frac{1}{2}\hat{b}^\dagger\hat{a}^\dagger. \tag{3.40}$$

One can show that the sets $(\hat{J}_{+1}, \hat{J}_0, \hat{J}_{-1})$ and $(\hat{J}'_{+1}, \hat{J}'_0, \hat{J}'_{-1})$ satisfy the algebra of angular momentum (A.7) and (A.16) in the entire boson space. However, the entire boson space is larger than the corresponding angular momentum space. We should map the angular momentum space to the subspace of the boson space. The possible state vectors of (3.36) is represented in the Table 3.1. We find that the subspace specified by S being positive integer is consistent with angular momentum space (A.2). Furthermore, the operators $\hat{J}_{\pm1}$ and $\hat{J}'_{\pm1}$ are closed in the subspace $\{|SJJ_0J'_0\rangle$ with $|J_0 \leq J\}$. Therefore the operators J_M's and J'_M's can be interpreted as the boson representation of the angular momentum vectors in each subspace specfied by S. The $\mathcal{D}$-operator is defined as the generation

operator of $|S+\sigma; J+\rho\ J_0+M\ J_0'+\mu\rangle$ from $|S; JJ_0J_0'\rangle$:

$$\hat{\mathcal{D}}(\sigma;\rho M\mu)|S; JJ_0J_0'\rangle = |S+\sigma; J+\rho\ J_0+M\ J_0'+\mu\rangle, \tag{3.41}$$

$$\hat{\mathcal{D}}(\sigma;\rho M\mu) = \hat{B}(\sigma+\rho+M)\hat{A}(\sigma+\rho-M)\hat{b}(\rho+\mu)\hat{a}(\rho-\mu). \tag{3.42}$$

The $\mathcal{D}$-operator should satisfy the following relation in each physical space:

$$\hat{\mathcal{D}}^{(L)}_{M\mu}|S; RR_0M\mu\rangle = \sum_{\rho}\langle JJ_0LM|R+\rho J_0+M\rangle \times(-1)^{\rho-\mu}\langle J+\rho J_0'+\mu J-\mu|JJ_0'\rangle|S; J+\rho J_0+MJ+\mu\rangle. \tag{3.43}$$

The operator can be expressed as

$$\hat{\mathcal{D}}^{(L)}_{M\mu} = \sum_{\rho}\bar{\mathcal{D}}^{(L)}_{M\rho}\bar{\mathcal{D}}'^{(L)}_{\rho\mu}, \tag{3.44}$$

$$\bar{\mathcal{D}}^{(L)}_{M\rho} = \bar{\mathcal{D}}(\rho M)\langle J-\rho J_0LM|JJ_0+M\rangle, \tag{3.45}$$

$$\bar{\mathcal{D}}'^{(L)}_{\rho\mu} = \bar{\mathcal{D}}(\rho,\mu)(-1)^{\rho-\mu}\langle J+\rho J_0'+\mu L-\mu|JJ_0'\rangle, \tag{3.46}$$

where

$$\hat{\mathcal{D}}(\sigma;\rho M\mu) = \bar{\mathcal{D}}(\sigma+\rho,M)\bar{\mathcal{D}}'(\rho,\mu), \tag{3.47}$$

$$\bar{\mathcal{D}}(\sigma+\rho,M) = B(\sigma+\rho+M)A(\sigma+\rho-M), \tag{3.48}$$

$$\bar{\mathcal{D}}'(\rho,\mu) = b(\rho+\mu)a(\rho-\mu). \tag{3.49}$$

3.2.2 Classial limit of the intermediate-coupling model

Hamiltonian of the present model H is already introduced in Eq. (3.1),

$$H = H_{\rm rot} + H_{\rm coupl} + H_{\rm mag}, \tag{3.50}$$

where the terms are defined as follows. The first term, $H_{\rm rot}$, stands for the rotational energy of the cluster which is expressed as

$$H_{\rm rot} = \sum_{i=1}^{3}\frac{\hat{R}_i^2}{2\mathcal{J}_i}, \tag{3.51}$$

where $\hat{R}_i$'s represent operators of three angular momentum components referred to the body fixed frame, and $\mathcal{J}_i$'s express principal moments of inertia. The second term, $H_{\rm coupl}$ expresses a coupling potential between the cluster and the super-electron spin, which is

originated from the crystal magnetic anisotropy energy caused by molecular or crystal fields. The symmetry of the coupling potential is changed reflecting to the symmetry of the crystal structure. In this thesis, we consider two types of symmetries. One is the dipole symmetry which is realized for the hcp structure in the bulk. The coupling Hamiltonian for the quadrupole symmetry is given in Eq. (3.4),

$$H_{\rm coupl} = uS'^2\left(\sin^2\theta - \frac{2}{3}\right) \tag{3.52}$$

$$= u\left(\frac{1}{3} - S_3'^2\right). \tag{3.53}$$

Another is the cubic symmetry realized in fcc or bcc structure for the bulk. The coupling Hamiltonian of the present symmetry is described in Eq. (3.11) as

$$\begin{aligned} H_{\rm coupl} &= 8uS'^4(\alpha_1^2\alpha_2^2+\alpha_2^2\alpha_3^2+\alpha_3^2\alpha_1^2-\frac{1}{5}) \\ &= -u\left\{S_1'^4+S_2'^4+S_3'^4-6(S_1'^2S_2'^2+S_2'^2S_3'^2+S_3'^2S_1'^2)\right. \\ &\quad \left.+\frac{3}{5}(S_1'^2+S_2'^2+S_3'^2)^2\right\}. \end{aligned} \tag{3.54}$$

The third term in Eq. (3.1) represents the interaction between the external magnetic field and the moments of the super-electron spin

$$H_{\rm mag} = -\boldsymbol{B}\cdot\boldsymbol{\mu} = -Bg_s\tilde{S}_z, \tag{3.55}$$

The transformation coefficient in the Cartesian coordinate between space-fixed and body-fixed frame A_{ij} is defined as

$$\hat{S}_i' = A_{ij}\hat{S}_j. \tag{3.56}$$

The coefficient is related to the $\mathcal{D}$ function which is also a transformation coefficient in the spherical bases,

$$\hat{S}_\mu' = \mathcal{D}^1_{\mu\nu}\hat{S}_\nu, \tag{3.57}$$

$$A_{ij} = T_{i\mu}\mathcal{D}^1_{\mu\nu}T^{-1}_{j\nu}. \tag{3.58}$$

We apply the Heisenberg equation of motion to the total Hamiltonian using Eq. (3.53) for $H_{\rm coupl}$.

$$\begin{aligned}\dot{\tilde{I}}'_i &= -i[\tilde{I}'_i, H] \\ &= -\epsilon_{ijk}\tilde{\omega}'_j\tilde{I}'_k - g_S B A_{z\beta}\epsilon_{\alpha\beta\gamma}\tilde{S}'_k + O(\hbar), \qquad (3.59)\\ \dot{\tilde{S}}'_i &= -i[\tilde{S}'_i, H] \\ &= -\epsilon_{ijk}\tilde{\omega}'_j\tilde{S}'_k + 2u\tilde{S}'_3\tilde{S}'_{(2\delta_{i1}+\delta_{i2})} - g_S B A_{z\beta}\epsilon_{ijk}\tilde{S}'_k + O(\hbar), \qquad (3.60)\\ \dot{\tilde{R}}'_i &= -i[\tilde{R}'_i, H] \\ &= -\epsilon_{ijk}\tilde{\omega}'_j\tilde{R}'_k - 2u\tilde{S}'_3\tilde{S}'_{(2\delta_{i1}+\delta_{i2})} + O(\hbar). \qquad (3.61)\end{aligned}$$

Supposing $H_{\rm coupl}$ to Eq. (3.54), we calculate the Heisenberg equation of motion,

$$\begin{aligned}\dot{\tilde{I}}'_i &= -i[\tilde{I}'_i, H] \\ &= -\epsilon_{ijk}\tilde{\omega}'_j\tilde{I}'_k + g_S B A_{zj}\epsilon_{ijk}\tilde{S}'_k + O(\hbar), \qquad (3.62)\\ \dot{\tilde{S}}'_i &= -i[\tilde{S}'_i, H] \\ &= -\epsilon_{ijk}\tilde{\omega}'_j\tilde{S}'_k + 16u\tilde{S}'_{i+1}\tilde{S}'_{i+2}(\tilde{S}'^2_{i+2} - \tilde{S}'^2_{i+1}) - g_S B A_{zj}\epsilon_{ijk}\tilde{S}'_k + O(\hbar), \qquad (3.63)\\ \dot{\tilde{R}}'_i &= -i[\tilde{R}'_i, H] \\ &= -\epsilon_{ijk}\tilde{\omega}'_j\tilde{R}'_k - 16u\tilde{S}'_{i+1}\tilde{S}'_{i+2}(\tilde{S}'^2_{i+2} - \tilde{S}'^2_{i+1}) + O(\hbar), \qquad (3.64)\end{aligned}$$

where $\tilde{\omega}'_i = \frac{\tilde{R}'_i}{\mathcal{J}'_i}$.

The time dependence of coefficient $A_{i\alpha}$ is defined by the Heisenberg equation;

$$\begin{aligned}\dot{A}_{i\alpha} &= -iT_{i\mu}[\mathcal{D}^1_{\mu\nu}, H]T^{-1}_{j\nu} \qquad (3.65)\\ &= \epsilon_{ijk}\omega_j A_{k\alpha}. \qquad (3.66)\end{aligned}$$

or

$$\dot{A}_{i\alpha} = -\epsilon_{\alpha\beta\gamma}\omega_\beta A_{i\gamma}. \qquad (3.67)$$

The equations are still in an operator form, we take an expectation value of the equations to make a corresponding classical theory. The coherent state is usually defined as the most "classical" state, that is, the quantum state with minimum-uncertainly [51]. However, the coherent state of angular momentum can not describe the variation of magnitude of angular momentum, while the angular momentum of rotor or the total angular momentum change the magnitude for the motion in the magnetic field. We adopt the coherent

state of the Schwinger boson representation of angular momentum which can describe the variation of the magnitude of angular momentum. The coherent state of angular momentum is applied to a classical state of super-spin:

$$|aa^*bb^*AA^*BB^*\zeta\zeta^*\rangle = |c\rangle|\zeta\zeta^*\rangle, \qquad (3.68)$$

where $|c\rangle$ and $|\zeta\zeta^*\rangle$ are the coherent state of the Schwinger boson representation of angular momentum and of angular momentum, respectively

$$\begin{aligned}|c\rangle &= \exp(BB^\dagger + AA^\dagger + bb^\dagger + aa^\dagger - B^*B - A^*A - b^*b - a^*a), \qquad (3.69)\\ |\zeta\zeta^*\rangle &= \exp(\zeta S'_+ - \zeta^* S'_-)|SS\rangle. \qquad (3.70)\end{aligned}$$

Note that the $|SS\rangle$ is the state in the body fixed frame where the commutation rule is different from the space fixed frame by sign [52]. The coherent state (3.70) is the eigenstate of the lowering operator S_- with an eigenvalue ζ. The expectation value of S_i's are calculated as

$$\begin{aligned}\langle\hat{S}_1\rangle &= S\sin\theta\cos\psi, \qquad (3.71)\\ \langle\hat{S}_2\rangle &= S\sin\theta\sin\psi, \qquad (3.72)\\ \langle\hat{S}_3\rangle &= S\cos\theta, \qquad (3.73)\end{aligned}$$

where the parameters θ and ϕ are defined as

$$\zeta = \frac{1}{2}\theta\exp i\sigma\psi. \qquad (3.74)$$

Then the coherent state is interpreted as a state that the angular momentum direction is represented by $(\theta\phi)$.

The coherent state (3.69) is the eigenstate of the bosons $\hat{B}, \hat{A}, \hat{a}$ and $\hat{b}$ with corresponding eigenvalues B, A, a and b. We parameterize the classical expectation value of the boson operator B, A, b and a to get the classical interpretation of the coherent state.

$$\begin{aligned}B &= \sqrt{2I}e^{-i\phi'/2}\sqrt{\cos^2\theta'/2 + S/2I}e^{-i\psi'/2}, \qquad (3.75)\\ A &= \sqrt{2I}e^{i\phi'/2}\sqrt{\sin^2\theta'/2 + S/2I}e^{-i\psi'/2}, \qquad (3.76)\\ b &= \sqrt{2I}e^{i\phi/2}\cos\theta/2e^{i\psi/2}, \qquad (3.77)\\ a &= \sqrt{2I}e^{-i\phi/2}\sin\theta/2e^{i\psi/2}. \qquad (3.78)\end{aligned}$$

The expectation values of $\hbar\hat{s}, \hbar\hat{I}, \hbar\hat{I}_0$, and $\hbar\hat{I}'_0$ for $|c\rangle$ are given by

$$\langle c|\hbar\hat{s}|c\rangle = \frac{\hbar}{2}(B_c^2 + A_c^2 - b_c^2 - a_c^2) = \hbar S, \tag{3.79}$$

$$\langle c|\hbar\hat{I}|c\rangle = \frac{\hbar}{2}(b_c^2 + a_c^2) = \hbar I, \tag{3.80}$$

$$\langle c|\hbar\hat{I}_0|c\rangle = \frac{\hbar}{2}(B_c^2 - A_c^2) = \hbar I_0, \tag{3.81}$$

$$\langle c|\hbar\hat{I}'_0|c\rangle = \frac{\hbar}{2}(b_c^2 - a_c^2) = \hbar I'_0. \tag{3.82}$$

Under the parameterization, $I_i's$ and $I'_j's$ are expressed as

$$\begin{aligned} I_x &= R\sin\theta'\cos\phi', \quad I_y = R\sin\theta'\sin\phi', \quad I_z = R\cos\theta', \\ I'_1 &= R\sin\theta\cos\phi, \quad I'_2 = R\sin\theta\cos\phi, \quad I'_3 = R\cos\theta, \end{aligned} \tag{3.83}$$

where we apply the following approximation in the derivation of Eq.(3.83). The fluctuation part of the coherent state which is of order of $\hbar$ is neglected. The approximation is justified under large angular momentum. We approximate that the Plank constant is zero. We take that R is infinite and that $\hbar R$ is constant. The quantum number S is the same order as that of R, and the fluctuation of S is vanished.

If (I_x, I_y, I_z) and (I'_1, I'_2, I'_3) can be regarded as angular momentum with respect to space-fixed frame and body-fixed frame the angles (θ', ϕ') and (θ, ϕ) specify the directions of the angular momentum vector in both frames. The sets of the angles (ϕ', θ', ψ') and (ϕ, θ, ϕ) are expected to be regarded as the Euler angles specifying a frame which can be obtained by rotations from the space-fixed frame and body-fixed frame, respectively. This frame is called Q-frame of which the 3-axis coincides with the direction of the angular momentum vector.

The expectation value of $\bar{D}(\rho M)$ and $\hat{D}(\rho M)$ are reduced to

$$\bar{\mathcal{D}}(\rho M) \to e^{iM\phi'}e^{i\rho\psi}, \quad \bar{\mathcal{D}}'(\rho M) \to e^{-i\rho\phi}e^{-\rho\psi\mu\phi}. \tag{3.84}$$

Using (A.63), the Clebsch-Gordan operators are also given as

$$\langle R - \rho R_0 JM|RR_0 + M\rangle \to \langle R - \rho R_0 JM|RR_0 + M\rangle \simeq d^{(J)}_{M\rho}(\phi'). \tag{3.85}$$

$$(-1)^{\rho-\mu}\langle R + \rho\Omega_0 + \mu J - \mu|R\Omega_0\rangle \to (-1)^{\rho-\mu}\langle R + \rho\Omega_0 + \mu J - \mu|R\Omega_0\rangle \simeq d^{(J)}_{\rho\mu}(-\theta). \tag{3.86}$$

Therefore, c-number approximations of $\bar{\mathcal{D}}^{(J)}_{M\rho}$ and $\bar{\mathcal{D}}^{(J)}_{\rho\mu}$ can be given in the following forms

$$\bar{\mathcal{D}}^{(J)}_{M\rho} = \mathcal{D}^{(J)}_{M\mu}(\phi', \theta', \psi'), \tag{3.87}$$

$$\bar{\mathcal{D}}'^{(J)}_{\rho\mu} = \mathcal{D}^{(J)}_{M\mu}(-\phi, -\theta, -\psi). \tag{3.88}$$

Thus, we can obtain the approximate expectation value of $\bar{\mathcal{D}}^{(J)}_{M\mu}$

$$\langle c|\bar{\mathcal{D}}^{(J)}_{M\mu}|c\rangle = \sum_\rho \mathcal{D}^{(J)}_{M\rho}(\phi'\theta'\phi') = \mathcal{D}^{(J)}_{M\mu}(\phi''\theta''\psi''). \tag{3.89}$$

Therefore, the coherent state is regarded as the most classical state of the rotor. The expectation value of the angular momentum operators or the $\mathcal{D}$-functions for the state (3.68) corresponds to one of the classical values. Therefore, the classical equation of motion is obtained by replacing the q-number with c-number in the equation (3.62-3.67).

3.3 Magnetic susceptibility

Magnetic susceptibility plays an important role in analyzing the experiment in which the magnetic field is so weak that magnetization linearly depends on the magnetic field. Examining the magnetic susceptibility, we can easily compare the present model, locked-moment model, and superparamagnetism. We calculate the magnetic susceptibility for intermediate coupling model and discuss the weak and strong coupling limits in following subsections.

For the present, let us discuss a general expression for magnetic susceptibility. Using the Feynman theorem, we obtain the expectation value of S_z as

$$\left\langle \hat{S}_z \right\rangle = -\left\langle \frac{\partial}{\partial(Bg_s)} H_{\rm mag} \right\rangle \tag{3.90}$$

$$= -\frac{\partial}{\partial(Bg_s)} \langle H_{\rm mag} \rangle . \tag{3.91}$$

The magnetic susceptibility is expressed as

$$\begin{aligned} \chi &= \frac{\partial}{\partial g_s B}\left\langle \hat{S}_z \right\rangle_{\rm enav}\Big|_{Bg_s=0} = -\frac{\partial^2}{\partial(Bg_s)^2}\Delta E_{\rm enav}\Big|_{Bg_s=0} \\ &= -\frac{2}{Z(T)}\sum_{\nu IM}\sum_{\nu' I'} \frac{|\langle \Psi_{\nu' I' M}|\hat{S}_z|\Psi_{\nu IM}\rangle|^2}{E_{\nu I} - E_{\nu' I'}} \exp\left(-\frac{E_{\nu I}}{k_B T}\right), \end{aligned} \tag{3.92}$$

where $\Delta E_{\rm enav}$ means the ensemble average of energy shift and partition function.

We will deal with the strong and weak coupling limits of the susceptibility (3.92) in Secs. 3.3.1 and 3.3.2, respectively. The susceptibility in intermediate coupling will be calculated numerically in Sec. 3.3.3.

3.3.1 Susceptibility for strong coupling

We first discuss the energy eigenvalue and the eigenstate of $H_{\rm rot} + H_{\rm coupl}$ in the strong coupling limit. Since the good quantum numbers are total angular momentum I and its projection on the z axis M, we rewrite the Hamiltonian of the present model in terms of the total angular momentum I,

$$\frac{\hat{\boldsymbol{I}}^2 + \hat{\boldsymbol{S}}'^2 - 2\hat{\boldsymbol{I}}\cdot\hat{\boldsymbol{S}}'}{2\mathcal{J}} + H_{\rm coupl}(\hat{\boldsymbol{S}}'). \tag{3.93}$$

The third term of the numerator is the Coriolis term, which couples the degrees of freedom of super-electron spin to the one of the rotor. It must be noticed that the Coriolis term is not taken into account in the locked moment model in which the super-electron spin is not included as a dynamical variable. We will be seen how this term contributes to the magnetic susceptibility.

Since $H_{\rm coupl}$ gives the dominant contribution to the energy eigenvalue of $H_{\rm rot}+H_{\rm coupl}$ in the strong coupling, the Coriolis term can be treated by perturbation theory. Without the Coriolis interaction, the unperturbed state is given as a direct product of the eigenfunction of $H_{\rm coupl}$ with respect to the intrinsic frame and the eigenfunction of the total angular momentum and its z component: $\mathcal{D}^I_{MK}(\Omega)\sum_{\sigma_k} g_{\sigma_k}|S\sigma_k\rangle$. The energy eigenvalues of the Hamiltonian neglecting the Coriolis term are expressed as

$$\frac{\hbar^2}{2\mathcal{J}}(I(I+1)+S(S+1)) + u'E^{\rm A}_N. \tag{3.94}$$

where $u'E^{\rm A}_N$ stands for the energy eigenvalue of the coupling Hamiltonian $H_{\rm coupl}$. This energy spectrum is the rotational band of band head energy $u'E^{\rm A}_N$. For the strong coupling limit, band head of excited band is much higher than one of the ground band. The occupation probability of the higher bands can be negligible. We assume that the susceptibility is described by the ground band only. This point will be discussed more closely in Appendix A.2.

Let us now focus on the ground band of the present model in the strong coupling. Figure 3.1 illustrates the energy eigenvalues of $H_{\rm coupl}$ evaluated numerically in the space $|S\sigma\rangle$: $E^{\rm A}_N$. The eigenstate of $H_{\rm coupl}$ must belong to a certain irreducible representation of the point group O. The irreducible representations A_1, E, T_1 for $S = 4n$, A_2, E, T_2 for $S = 4n+2$, and T_1, T_2 for odd S appear in the lowest energy region. Considering the dimension of these representations, namely 1,1,2,3 and 3 for A_1, A_2, E, T_1 and T_2, respectively, we find that the bunch of the levels always contains six states. The six-fold and the eight-fold approximately degenerate states appear at the lowest and highest energies, respectively. This fact implies that the direction of super-electron spin is localized to the six (eight) directions corresponding to the potential minima (maxima) in the lowest (the highest) bunching states for large S. Therefore, these states are approximated by

$$\hat{R}^i|SS\rangle, \tag{3.95}$$

where $\hat{R}^i$ stands for the operator corresponding to the rotation from the third axis to the ith direction of the potential minima.

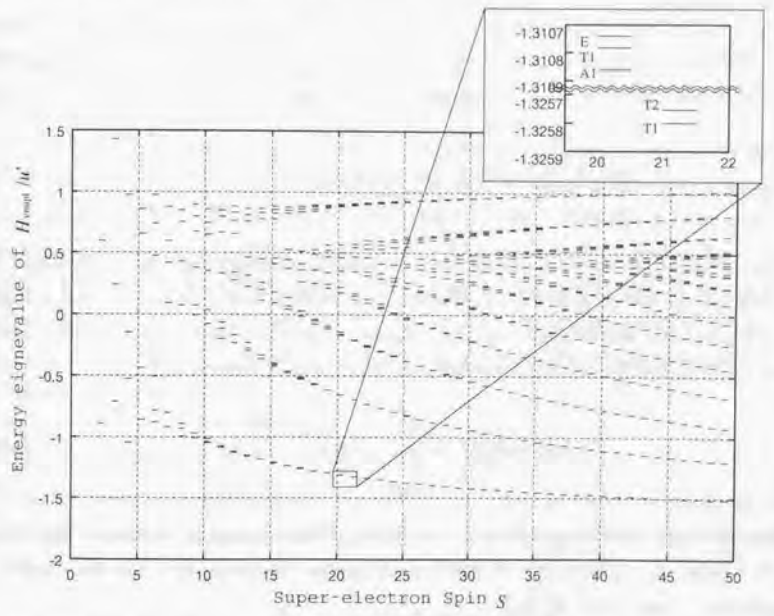

Figure 3.1: The eigenvalue of $H_{\rm coupl}/u'$ as a function of the magnitude of super-spin S.

For the present, we shall take into account the Coriolis term in first-order perturbation theory. According to the first-order perturbation theory of degenerate states, we should solve the secular equation in order to determine the energy shift and perturbed states. In

this case, each level in the rotational band is $6(2I+1)^2$-fold degenerate: The quantum numbers M, K have the values $-I \leq M\ K \leq I$ and the ground state of super-electron spin is six-fold degenerate. The dimension of the secular equation is reduced by a factor of $(2I+1)$ because M is a good quantum number. As we discussed before, the direction of super-electron spin corresponds to the one of the potential minima for the ground state. Choosing the direction of quantization axis as one of the potential minima, we can express the Coriolis term as

$$\hat{\boldsymbol{I}} \cdot \hat{\boldsymbol{S}} = \hat{I}_3^i \hat{S}_3^i + (\hat{I}_+^i \hat{S}_-^i + \hat{I}_-^i \hat{S}_+^i), \quad \begin{matrix} \hat{I}_3^i = \hat{R}^i \hat{I}_3 \hat{R}^{i\dagger}, & \hat{I}_\pm^i = \hat{R}^i \hat{I}_\pm \hat{R}^{i\dagger}, \\ \hat{S}_3^i = \hat{R}^i \hat{S}_3 \hat{R}^{i\dagger}, & \hat{S}_\pm^i = \hat{R}^i \hat{S}_\pm \hat{R}^{i\dagger}. \end{matrix} \tag{3.96}$$

The second term of Eq. (3.96) does not contribute to the Coriolis matrix element between parallel, antiparallel, or orthogonal directions. In fact, we can estimate the matrix element of raising and lowering operators of super-electron spin:

$$\langle SS|\hat{S}_\pm \hat{R}'(\theta)|SS\rangle = \begin{cases} 0, & \text{for } \theta = 0, \\ \propto \hbar\sqrt{2S}(1/2)^{S+1}, & \text{for } \theta = \frac{\pi}{2}, \\ 0. & \text{for } \theta = \pi, \end{cases} \tag{3.97}$$

where $\hat{R}'(\theta)$ is the rotation through angle θ about the axis perpendicular to the 3 axis. In addition, the first term of Eq. (3.96) does not contribute to the matrix element between orthogonal and antiparallel directions, because the matrix elements of $\hat{S}_3^i$ for orthogonal and antiparallel directions are evaluated as $(1/2)^S$ and 0, respectively:

$$\langle SS|\hat{R}'(\theta)|SS\rangle = \begin{cases} 1, & \text{for } \theta = 0, \\ \propto (1/2)^S, & \text{for } \theta = \frac{\pi}{2}, \\ 0, & \text{for } \theta = \pi. \end{cases} \tag{3.98}$$

The Coriolis matrix element does not vanish only between parallel directions. Therefore, the secular equation for the Coriolis term is approximately solved. The wave function results in an eigenstate of $\hat{I}_3^i$:

$$|IMKi\rangle = \hat{R}^i|SS\rangle \hat{R}^i \sqrt{\frac{2I+1}{8\pi^2}} \mathcal{D}^I_{MK}(\Omega). \tag{3.99}$$

The first-order energy shift is obtained as

$$\langle I'MK'j|2\hat{\boldsymbol{I}} \cdot \hat{\boldsymbol{S}}|IMKi\rangle = 2\hbar^2 KS \delta_{K,K'} \delta_{I,I'} \delta_{i,j}. \tag{3.100}$$

We calculate the susceptibility for the strong coupling limit supposing the wave function of the ground band to be Eq. (3.99). A detailed account of the derivation of the susceptibility will be described in Appendix A.2. We obtain

$$\chi \simeq \frac{2}{9}\frac{\hbar^2 S^2}{k_{\rm B}T}\left(1 - \frac{2}{5}\beta' S^2 + \frac{4}{35}(\beta' S^2)^2 + \cdots\right) < \frac{2}{9}\frac{\hbar^2 S^2}{k_{\rm B}T}, \tag{3.101}$$

where $\beta' = \frac{\hbar^2}{2\mathcal{J}k_{\rm B}T}$. The leading order corresponds to susceptibility for the locked moment model. The higher orders mean correlations through the Coriolis term, in other words, a recoil effect due to the angular momentum of the super-electron spin or Einstein-de Haas effect. We find from Eq. (3.101) that this effect always suppresses the magnetic susceptibility compared with the one of the locked moment. This fact is apparently seen in numerical calculations in Sec. 3.3.3.

3.3.2 Susceptibility for weak coupling

In this subsection we calculate the susceptibility for the weak coupling and high temperature limits. First, we discuss the energy eigenvalue and the eigenfunction of $H_{\rm rot} + H_{\rm coupl}$ in the weak coupling. In the absence of coupling, the energy eigenvalues form a single rotational band with $(2R+1)^2$-fold degeneracy. The coupling is treated as first-order perturbation theory; the energy shift and wave function are determined by solving the secular equation in a set of degenerate states. Since the degenerate levels in the rotational band split up under the influence of the weak coupling, the energy eigenvalues are expressed as

$$\frac{\hbar^2 R(R+1)}{2\mathcal{J}} + \Delta E_{I\lambda(R)}, \tag{3.102}$$

where $\lambda(R)$ specifies the state adiabatically connected with R, and $\Delta E_{I\lambda(R)}$ stands for the energy shift obtained as the eigenvalue of the weak anisotropic coupling. The perturbed wavefunction is expressed as

$$\Psi_{\lambda(R)IM} = \sum_{k\sigma\mu} \langle R\mu S\sigma|IM\rangle\, \mathcal{D}^R_{\mu k}(\Omega) c_k^{\lambda(R)} |S\sigma\rangle\,, \tag{3.103}$$

where the coefficient $c_k^{\lambda(R)}$ is determined by the diagonalization of $H_{\rm coupl}$ in the degenerate levels in each R.

We calculate, by employing the Eq. (3.92), the magnetic susceptibility for weak coupling in the form of a second-order correction to the energy. The energy denominator

between the levels in different R is much larger than the one in the same R in the weak coupling. Thus, we neglect the mixing of states in different R in the limit. The matrix element of Zeeman interaction between the weak coupling bases, Eq. (3.103), can be calculated using the orthogonality condition $\sum_k c_k^{\lambda(R)*} c_k^{\lambda'(R)} = \delta_{\lambda\lambda'}$ as

$$\left\langle \Psi_{\lambda(R)IM} | \hat{S}_z | \Psi_{\lambda'(R)I'M} \right\rangle = \hbar^2 \delta_{\lambda,\lambda'} \sqrt{2I'+1} (-1)^{I'} \langle I'M10|IM\rangle \times \sqrt{S(S+1)(2S+1)} (-1)^{R-S+1} W(ISI'S;R1). \tag{3.104}$$

The substitution Eqs.(3.102) and (3.104) into Eq. (3.92) yields

$$\chi = -\frac{2}{Z(T)} \sum_R \left(\sum_{\lambda(R)MI \neq I'} \frac{|\left\langle \Psi_{\lambda(R)IM} | \hat{S}_z | \Psi_{\lambda(R)I'M} \right\rangle|^2}{\Delta E_{I\lambda(R)} - \Delta E_{I'\lambda(R)}} e^{-\frac{E_R + \Delta E_{I'\lambda(R)}}{k_B T}} \right), \quad E_R = -\frac{\hbar^2 R(R+}{2\mathcal{J}} \tag{3.105}$$

Since $\Delta E_{I'\lambda(R)}$ is small due to the weak coupling, we can approximate $e^{-\frac{\Delta E_{I'\lambda(R)}}{k_B T}}$ to $1 - \frac{\Delta E_{I'\lambda(R)}}{k_B T}$. Rearranging the summation, we have a form of the susceptibility being independent of dynamics,

$$\chi \simeq -\frac{2}{Z(T)} \sum_R \left(\sum_{\lambda(R)MI > I'} \frac{|\left\langle \Psi_{\lambda(R)IM} | \hat{S}_z | \Psi_{\lambda'(R)I'M} \right\rangle|^2}{k_B T} \right) e^{-\frac{E_R}{k_B T}}. \tag{3.106}$$

Putting Eq. (3.104) into Eq. (3.106), and expanding for R, we obtain the magnetic susceptibility

$$\chi \simeq 2 \frac{\sum_{R=0}^{\infty} \hbar^2 \left(\frac{4S(S+1)(2S+1)R^2}{9} + \cdots \right) \exp\left(-\frac{\hbar^2 R(R+1)}{2\mathcal{J} k_B T} \right)}{\sum_{R=0}^{\infty} \left((2R+1)^2 (2S+1) \right) \exp\left(-\frac{\hbar^2 R(R+1)}{2\mathcal{J} k_B T} \right)} \tag{3.107}$$

At the high temperature limit, one can evaluate Eq. (3.107), treating R as a continuous variable and replacing the sum by integral;

$$\chi \simeq \frac{2\hbar^2 S(S+1)}{9 k_B T}. \tag{3.108}$$

It is observed in this subsection that the susceptibility of the weak coupling limit coincides with the one of the locked moment. One should note that this does not mean that the super-electron spin is locked in the weak coupling limit. The susceptibility is independent of the dynamics in the weak coupling limit, whereas, in the strong coupling limit, the susceptibility originates from the locked moment dynamics. In fact, taking into account

the axial deformation, we find the susceptibilities of the weak and the strong coupling limits are different.

The matrix element of $\hat{S}_z$ is independent of the deformation, because Eq. (3.104) is independent of λ. For the axial deformation with weak coupling, 3 component of angular momentum of rotor is a good quantum number. Then the wave function becomes

$$|IMRk\rangle = \sum_{\mu\sigma} \langle R\mu S\sigma | IM \rangle \sqrt{\frac{2R+1}{8\pi^2}} \mathcal{D}^R_{\mu k} |S\sigma\rangle. \tag{3.109}$$

The energy level for the axial deformation is

$$E_{IRk} = \frac{R^2 + (\alpha - 1)k^2}{2\mathcal{J}_1}, \tag{3.110}$$

where $\alpha = \frac{\mathcal{J}_1}{\mathcal{J}_3}$. Putting Eqs. (3.110), (3.109) and (3.104) into (3.92), we can calculate the susceptibility of the weak coupling with axial deformation. The result is same as Eq. (3.107) when the deformation is small

In the calculation, we replace sum with integral, and neglect the Coriolis effect by taking the limit of S goto 0. The result of susceptibility is given by

$$\chi \simeq \frac{2}{9} \frac{\hbar^2 S(S+1)}{k_B T}. \tag{3.111}$$

The dependence of deformation α in the numerator originated from the magnetic interaction of system is canceled by partition function in the denominator. Thus, the susceptibility in the weak coupling is independent of the axial deformation.

In the strong coupling with the axial deformation, the energy level for the ground band is dependent on the deformation

$$E_{IK} = -\beta(I(I+1) + (\alpha - 1)K^2 + \alpha K S), \tag{3.112}$$

where $\beta = \frac{\hbar^2}{2\mathcal{J}_1 k_B T}$. The eigenstate is not different from one of the spherical, the matrix element of $\hat{S}_z$ for axial deformed cluster coincides with the spherical one. Putting the energy (3.112) and eigenfunction (3.99) into (3.92) and expanding it for K and $(1-\alpha)$, we can obtain after lengthly but straightforward calculation the susceptibility of the axial deformed locked moment model

$$\chi \simeq \frac{2}{9} \frac{\hbar^2 S^2}{k_B T} \left(1 - \frac{1}{5}(1-\alpha) + \cdots \right). \tag{3.113}$$

Therefore, considering the axial deformation, we find that the susceptibility for the weak and the strong coupling limits are different. The two limits happen to be the same value when the value of $\mathcal{J}_i's$ are equal.

3.3.3 Intermediate coupling

We calculate the magnetic susceptibility for intermediate coupling in this subsection. In numerical calculations of the deflection profile and the magnetization, a main task is diagonalization of Hamiltonian matrices of large dimensions. In the source area, the partial Hamiltonian $H_{\rm mag}$ is zero, and therefore the total angular momentum is conserved. The most major population of angular momentum is $I_{\rm eff}(T) = \sqrt{\frac{2\mathcal{J}k_{\rm B}T}{\hbar^2}}$ for the rotational band with $(2I+1)^2$-fold degeneracy. The dimension of matrices to be diagonalized is approximately $S \times I_{\rm eff}(T)$. A typical size is of the order of 10^5. In the magnetic field where states having $I/2$ different are mixed, the number of dimensions is magnified by $I/2$, and becomes eventually of the order of 10^7. It may not be feasible in numerical calculations. Let us use a similarity transformation in order to scale down the angular momenta. In Eq. (3.15), the matrix element is approximated as

$$(H_{\rm coupl})_{RK,R'K'} \simeq A'_\kappa \frac{\sqrt{(2R+1)(2R'+1)}}{2\overline{R}+1} d^1_{\kappa\mu}(\theta_1) d^1_{\mu 0}(\theta_2) \tag{3.114}$$

with

$$\overline{R} = \frac{R+R'}{2} \quad \text{and} \quad \mu = R' - R, \tag{3.115}$$

and two angles, θ_1 and θ_2 are defined, respectively, as

$$\cos\theta_1 = \sqrt{\frac{\overline{K}}{\overline{R}}} \quad \text{with} \quad \overline{K} = \frac{K+K'}{2}$$

and

$$\cos\frac{\theta_2}{2} = \sqrt{\frac{(\overline{R}-S+I)(S-\overline{R}+I)}{4\overline{R}S}}. \tag{3.116}$$

These angles are invariant under a scale transformation defined as

$$\begin{pmatrix} r, r'\ \overline{r} \\ k, k'\ \overline{k} \\ s, i, m \end{pmatrix} = \eta \begin{pmatrix} R, R'\ \overline{R} \\ K, K'\ \overline{K} \\ S, I, M \end{pmatrix}. \tag{3.117}$$

In a similar manner, the matrix elements given in Eq. (3.17) are expressed approximately as

$$\langle \Psi_{\nu\pi_K IM} \mid H_{\rm mag} \mid \Psi_{\nu' I' \pi_K M} \rangle \simeq B g_{\rm s} \sqrt{S(S+1)} \frac{\sqrt{(2I+1)(2I'+1)}}{2\overline{I}} \sum_{RK} f^{\nu I *}_{RK} f^{\nu' I'}_{RK} (-)^{I'-I} d^1_{0\,I-I'}(\theta_3) d^1_{I-I'\,0}(\theta_4) \tag{3.118}$$

with

$$\cos\theta_3 = \sqrt{\frac{M}{\overline{I}}}, \quad \cos\frac{\theta_4}{2} = \sqrt{\frac{(\overline{I}-S+R)(S-\overline{I}+R)}{4\overline{I}S}}.$$

The two additional angles θ_3 and θ_4 are also invariant under the scale transformation. Eventually these four angles are invariant under the transformation in Eq. (3.117). The four d functions are all smooth functions of the four angles.

To make $\hat{S}^2$ invariant under the similarity transformation, Eq. (3.117), the Plank constant is changed according to η. In other words, we can scale down the angular momentum quantum number by adjusting the Plank constant as

$$\hbar' = \frac{\hbar}{\eta}, \quad s = \eta S. \tag{3.119}$$

The temperature $k_{\rm B}T$, the coupling u', and magnetic field parameter $g_{\rm s}B\hbar S$, which have dimension of energy, are invariant under the similarity transformation. In the following, the units of these energy parameters are selected as $\frac{\hbar^2 S^2}{2\mathcal{J}}$ which is also invariant under the similarity transformation.

We are now ready to calculate numerically the susceptibility in the intermediate coupling scheme. It is already known by the analysis in Sec. 3.3.1 that the ground state of $H_{\rm coupl}$ has to be approximately six-fold degenerate states in the strong coupling limit. It seems reasonable that the ground state is approximately six-fold degenerate for $S_{\rm c} = 10$. The reason for this is based on the numerical diagonalization of $H_{\rm coupl}$ in $S_{\rm c} = 10$ (Fig. 3.1). Three energy levels having one-fold, three-fold, and two-fold degeneracies from lower energy to higher make a bunch around the ground state. The energy differences of these states are about 0.01. In contrast to this, we find from Fig. 3.1 that the energy difference between the bunch of the ground state and the first excited bunch is about 1.0. The energy spacings between six states around the ground state are much smaller than the energy spacing between the ground bunch and the first excited bunch. Therefore, we can regard the ground state as approximately six-fold degenerate state.

A truncation of the angular momentum is necessary to make numerical diagonalization feasible. We select $I_{\rm max} = 80$ in the calculation. The occupation probability steeply declines as the energy becomes large. For the rotational band, one can neglect states of high angular momentum in the calculation of the partition function. Actually, for the single rotational band with $(2I+1)^2$-fold degeneracy, levels of which the angular momentum is larger than $I_{\rm c}(T) = \sqrt{6.2\mathcal{J}k_{\rm B}T/\hbar^2}$ contribute only less than 10 % of the

partition function. Therefore the numerical calculation of the partition function is reliable only if $I_c(T) \leq I_{\max}$. For $I_{\max} = 80$, the result of the calculation is reliable in its range $k_B T < 20.6$. We choose 20 for the temperature.

We display the coefficient χ' of the magnetic susceptibility obtained by numerical calculation in Fig. 3.2. The coefficient χ' is defined as

$$\chi = \chi' \frac{\hbar^2 S^2}{k_B T}. \tag{3.120}$$

We exactly diagonalized $H_{\rm rot} + H_{\rm coupl}$ which includes full the Coriolis term. Then, the Zeeman coupling $H_{\rm mag}$ is treated as perturbation theory. The first point to be discussed is whether our calculation reaches the two distinct limits discussed above. The susceptibility in Fig. 3.2 decreases and converges on 2/9, as the coupling becomes smaller than the temperature. Therefore the result of the calculation is consistent with the analysis for the weak coupling discussed in Sec. 3.3.2.

The second point is the strong coupling limit. As we will discuss in Appendix A.2, Eq. (A.26) is the conditions of temperature and coupling to attain the susceptibility of the locked moment. The application of Eq. (A.26) for $S_c = 10$ yields the condition of strong coupling:

$$\frac{u'}{k_B T} \gg 3.1. \tag{3.121}$$

As discussed in Sec. 3.3.1, the coefficient of susceptibility for the strong coupling is not the locked moment value 2/9 but smaller than it due to the recoil effect. Actually, in Fig. 3.2, the results of the strong coupling are also smaller than 2/9 (dashed line), and close to the value of Eq. (3.101) (dotted line). A possible reason for some deviation from the dotted line is that the quantum fluctuation of the direction of the super-spin among different minima of the coupling potential decreases the susceptibility.

A peak at $\frac{u'}{k_B T} \simeq 0.55$ is found in Fig. 3.2. This peak accounts for the energy splitting of the anisotropic interaction being comparable to the energy splitting by Coriolis term $\frac{\hbar^2}{2\mathcal{J}} 4 S I_{\rm eff}(T)$. The width of the energy splitting of the anisotropic interaction corresponds to the energy difference between potential maxima and minima, i.e., $\frac{8}{3}u'$. In practice the width becomes smaller due to the quantum fluctuation of the direction of super-spin and is found $2u'$ for $S = 10$ from Fig. 3.1. Then the peak is expected to be

$$2u' \simeq \frac{\hbar^2}{2\mathcal{J}} 4 I_{\rm eff} S \quad \Leftrightarrow \quad \frac{u'}{k_B T} \simeq 2\sqrt{\frac{\hbar^2 S^2}{2\mathcal{J}} \frac{1}{k_B T}} \simeq 0.45. \tag{3.122}$$

In fact, this condition is consistent with the observed position of the peak.

As mentioned in the Introduction, one often assumes superparamagnetism, in which the susceptibility is $\frac{1}{3}\frac{\hbar^2 S(S+1)}{k_B T}$ for the clusters to analyze the experiments. We find from Fig. 3.2 that the superparamagnetic limit is not reached in any range of coupling strength.

The last point is the temperature dependence of the magnetization. It is reasonable to consider that the susceptibility decreases as the temperature increases because of thermal fluctuations of the direction of super-spin. In Ref. [26], it was reported that the temperature dependence of the magnetization is reversed. However, in our calculations, such a behavior did not appear in any range of coupling.

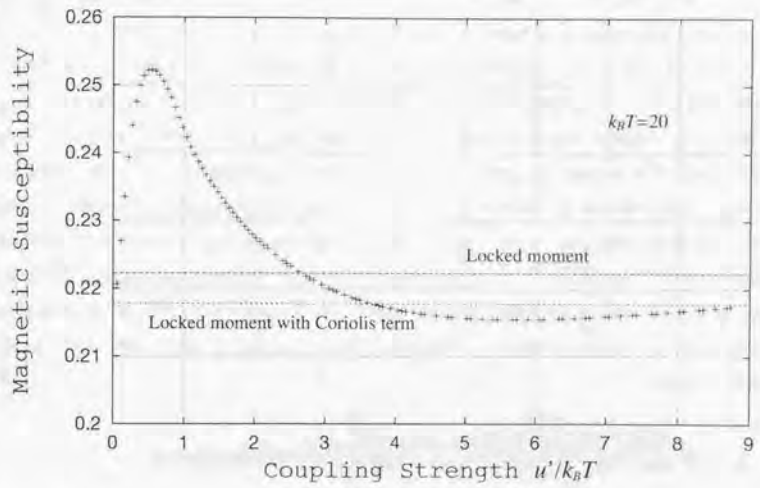

Figure 3.2: The magnetic susceptibility calculated by the perturbation theory. The ordinate is the coefficient of the magnetic susceptibility χ' (described in text). The abscissa is the ratio of the coupling strength to temperature.

We investigate the quantum state which consists the peak using the classical equation of motion discussed in Sec. 3.2.2. Calculating the susceptibility of quadrupole coupling, we confirmed that the position of the peak in the susceptibility does not changed in the quadrupole coupling. In the classical calculation, we adopt the quadrupole coupling to

keep computational time short. Fig. 3.3 shows the energy levels for $I = 20, S = 10, k = 10$ obtained by both quantum and classical theory as a function of the quadrupole coupling. We solve the equation of motion with adiabatically increasing the strength of coupling. The initial condition is decided by the additional quantum number R in the absence of coupling. The orbit of low energy and high energy levels in the absence of the coupling is confined in the region of $S_3 > 0$. However in the intermediate energy region, the orbit moves between the regions of $S_3 > 0$ and $S_3 < 0$. If the quadrupole potential is increased, the orbit confined to the region of either $S_3 > 0$ or $S_3 < 0$. The time average of S_3 is approximately zero. The staggering seen in the classical calculation of energy level originates from the confinement of orbit. The upper (lower) part of the staggering correspond to the confinement to the positive (negative) region. The staggering starts when the coupling $\frac{2}{3}u'S^2$ is equal to the difference of the rotational energy $R^2/\mathcal{J}$ and the minimum of rotational energy $(I - S)^2/2\mathcal{J}$ in the absence of coupling. Therefore, the points where the staggering starts are on the line of $E = (I - S)^2/2\mathcal{J} + 2u'S^2/3$.

When the typical angular momentum $R \simeq 20$, the typical energy is approximately 400. According to the discussion above, the peak is expected at $u' \simeq 10$. The point $(u', E) \simeq (10, 400)$ lies on the line of staggering starts. We calculate susceptibility of each levels using the classical theory. Figure 3.4 illustrates the susceptibility of each level. The peaks found in the figure correspond to the points where staggering starts. Though the peak is seen in the positive and negative region, the magnitude of positive peak is always larger than one of the negative. Therefore these orbit significantly affects the peak of susceptibility.

3.4 Profiles and magnetization

As mentioned in the previous section, truncation of the angular momentum is necessary to make the numerical calculations feasible. We take $I_{\max} = 26$ and the magnitude of super-electron spin $S_c = 10$. The result of the calculation is reliable if $k_B T < 2$ for $I_{\max} = 26$. Since high temperature is one of the conditions to achieve a locked moment, we should select the temperature as high as possible. Then we choose $k_B T = 2$.

First, we pay attention to the magnetic field dependence of the deflection profile. Figure 3.5 shows the deflection profile for three values of the magnetic field strength $g_s BhS = 0.5, 2, 10$, respectively. Our calculation exhibits that the position of the peak

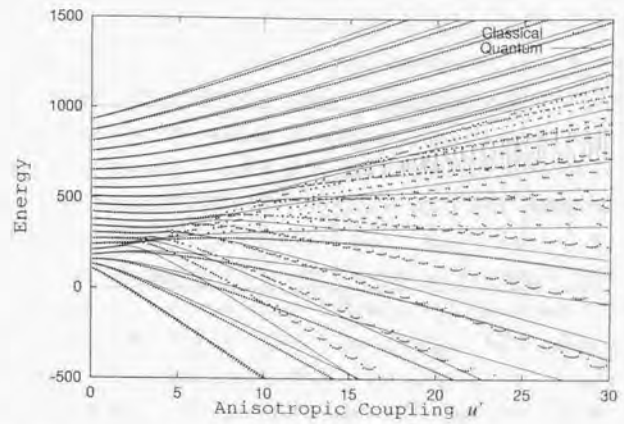

Figure 3.3: The energy levels obtained by the classical and quantum theory for $I = 20, S = 10, k = 10$.

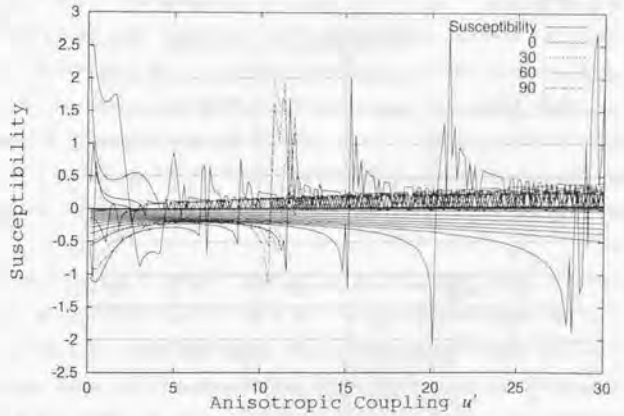

Figure 3.4: The susceptibility of each level in the Fig. 3.3. The solid line corresponds to M=0. As shown in the keys in the graph, dotted lines means $\cos^{-1}\frac{M}{I}$=30,60,90.

always deflects to the strong field side, as observed in many experiments. By solving the classical equation of motion, Ballone *et al.* have demonstrated in Ref. [53] that the coupling between the super-spin and the cluster body causes the deflection behavior. We will have a closer examination of this statement in terms of our quantal model.

In order to make our discussion transparent, we start with the weak coupling limit. The profile of the weak coupling in Fig. 3.5 is a flat but slightly sloping distribution in the weak magnetic field. Figure 3.6 showing the energy levels of the weak coupling, $u' = 4.47 \times 10^{-3}$, for $S_c = 2, M = 0, \pi_k = 0$, and $R \simeq 3$ or 4, helps us to understand the distribution in terms of the energy level. In the absence of coupling, the energy levels of the present model form a single rotational band. These levels split up under the influence of the weak coupling; energy levels form a bunch of states around each unperturbed state in the rotational band. As the applied magnetic field becomes stronger than the coupling, these levels split up again under the influence of the applied magnetic field, and are rearranged more likely to be the eigenfunction of $\hat{S}_z$. In other words, the super-spin precesses about the direction of the magnetic field independently of the cluster (decoupling) for $g_s B\hbar S > u'$. Occupation probabilities of levels in the same R become almost equal due to the weak coupling. Then, the magnetization remains small and the profile becomes a flat distribution. When the energy difference resulting from the Zeeman splitting is equal to a typical energy spacing of the rotational levels; $2g_s B\hbar S = \hbar^2 R_{\rm eff}/\mathcal{J}$, a pseudo-crossing between different rotational levels occurs. In other words, the pseudo-crossing takes place where the Larmor precession frequency $\omega_{\rm L}$ is comparable to the cluster rotation frequency $\omega_{\rm rot}$: $\omega_{\rm L} \simeq \omega_{\rm rot}$. That is to say, the pseudo-crossing leads to an exchange of the occupation probabilities between those levels. This process increases the magnetization, and develops a peak in the profile at $\langle S_z \rangle / S = 1$ like the Boltzmann distribution.

The above discussion leads us to divide the mechanisms of magnetization into two types, that is, the magnetizations by the processes of decoupling and by the pseudo-crossing. These two types of magnetization are apparently seen in Fig. 3.7 in which we show the magnetic field dependence of the magnetization in the weak coupling. The magnetization linearly increases as the magnetic field in the process to decoupling; then remains steady by the decoupling of super-spin; finally increases suddenly through the pseudo-crossing.

In the intermediate and the strong coupling, we cannot distinguish the regions of

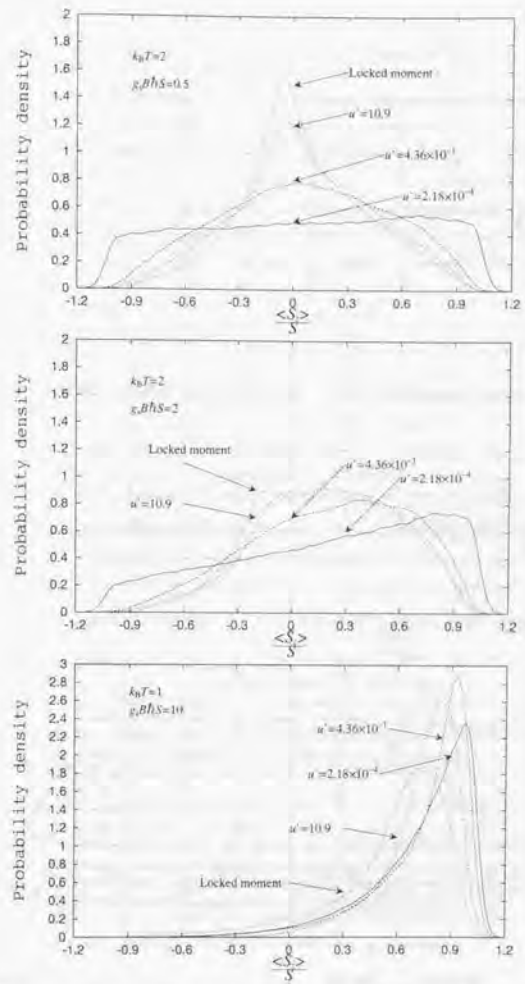

Figure 3.5: The profile for three coupling strength $u' = 2.24 \times 10^{-4}, u' = 4.47 \times 10^{-1}$, and $u' = 11.2$. of magnetic field $g_s B\hbar S = 0.5, 2, 10$. The temperature is set to $k_B T = 2$ for $g_s B\hbar S = 0.5, 2$ and to $k_B T = 1$ for $g_s B\hbar S = 10$.

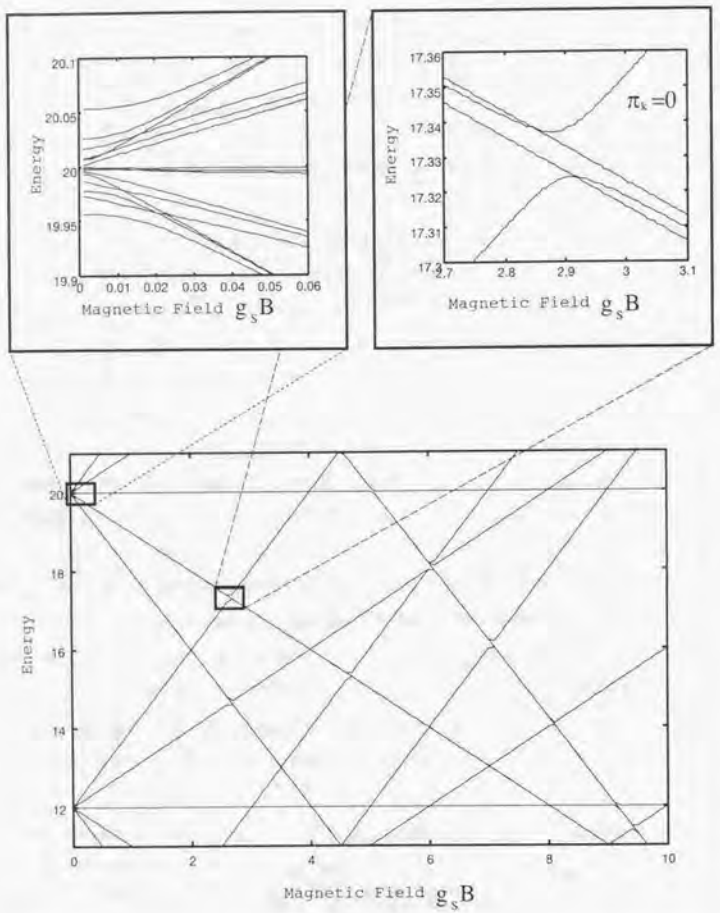

Figure 3.6: Energy levels of the weak coupling ($u' = 4.47 \times 10^{-3}$) as a function of magnetic field for $S_c = 2, M = 0.$ and $R \simeq 3$ or 4.

Figure 3.7: An example of peculiar behavior of magnetization for $S_c = 2$

the magnetic field strength in which either the decoupling or the pseudo-crossing occurs. Accordingly, the peculiar behavior of magnetization observed in the weak coupling disappears.

The calculated susceptibility (Fig. 3.2) indicates that $u' = 11.2$ is in the strong coupling region. However, the profile in this case in Fig. 3.5 is not identical with the locked moment profile. We attribute this to the Coriolis term, which is important at the temperature of the ensemble, $k_B T = 2$. A higher temperature was possible in the calculation in Ref. [8] because a simpler anisotropy term there permitted smaller dimension Hamiltonian matrices. In fact, we confirmed that the calculation of $I = 26, S = 10$ for the quadrupole coupling do not show the superparamagnetic peak.

Finally, let us move to the discussion of the profiles in intermediate coupling. We select the cumulants to characterize the profiles. The first and second order cumulant mean the average and the variance of the profile, respectively. A cumulant higher than second-order vanishes for the Gaussian probability distribution. In our calculation the third- and fourth-order cumulants are less than 10% and 1% of second-order, respectively.

Thus, the profiles in the intermediate coupling can be approximated by the Gaussian profile.

We now discuss the first (Fig. 3.9) and the second-order cumulant (Fig. 3.10) in more detail. The general trend of the first-order cumulant looks like more or less one of either the superparamagnetic or locked moment. The magnetization of intermediate coupling is smaller than the one of the locked moment because of the recoil effect. We may note, in passing, that the anomalous behavior in the weak coupling, discussed earlier, should appear when the energy splitting by the magnetic field is comparable to the typical energy difference of rotational levels, that is,

$$2g_s B\hbar S \simeq \frac{2\hbar^2 R_{\rm eff}}{2\mathcal{J}} \quad \Leftrightarrow \quad g_s B\hbar S \simeq \frac{1}{S}\sqrt{\frac{\hbar^2 S^2 k_{\rm B}T}{2\mathcal{J}}} \simeq 0.14. \tag{3.123}$$

But this region is out of the calculated range of the Fig. 3.9.

The second-order cumulant is calculated by means of two methods. One is the direct diagonalization of H, and the other is the perturbation for the magnetic field. Figure 3.10 illustrates the second-order cumulant, as a function of magnetic field, obtained by direct diagonalization. The second order cumulant is sensitive to the coupling. The cumulant declines as either the coupling or the magnetic field becomes stronger. In other words, the magnetic field and the coupling make the shape of the profile narrower. The second-order cumulant of the locked moment profile in the absence of a magnetic field and the flat profile observed in the decoupling region are estimated as $\frac{1}{9}$ and $\frac{S(S+1)}{3S^2}$, respectively. Actually, in Fig. 3.10, the strong coupling $u' = 10.9$ and the weak coupling $u' = 2.18\times10^{-4}$ in the weak magnetic field are close to $\frac{1}{9}$ and $\frac{S(S+1)}{3S^2}$, respectively.

Figure 3.8 shows the second order cumulant in the absence of a magnetic field evaluated by perturbation of the magnetic field. The maximum of angular momentum $I_{\rm max}$ and the temperature $k_{\rm B}T$ are taken at 80 and 20, respectively. The maximum of the angular momentum in this calculation is much larger than the one in the direct diagonalization. The second order cumulant of the profile approaches the strong coupling limit 1/9 in the coupling $u' = 3.5$. It decreases almost linearly in the region of the coupling beyond 20 because of the tunneling between different directions of the potential minima.

For the weak coupling limit, the ensemble average of the profile converges on 0.122 as seen in Fig. 3.8. We can estimate the second-order cumulant of the weak coupling limit. The magnetization of each level in this limit is calculated from the diagonal part of Eq. (3.104):

$$\langle \hat{S}_z \rangle = \hbar\sqrt{2I+1}(-1)^I \langle IM10|IM\rangle \sqrt{S(S+1)(2S+1)}(-1)^{R-S+1} W(ISIS;R1). \tag{3.124}$$

The second-order cumulant for weak coupling is estimated to be

$$\langle \hat{S}_z \rangle^2_{\rm cumulant} = \hbar^2 \frac{S(S+1)(2S+1)}{Z(T)} \sum_{RI M\lambda(R)} (2I+1) |\langle IM10|IM\rangle|^2 |W(ISIS;R1)|^2 \exp(-\frac{E_R}{k_{\rm B}T}). \tag{3.125}$$

Treating R as a continuous variable and replacing the sums by an integral yields

$$\langle \hat{S}_z \rangle^2_{\rm cumulant} \simeq \frac{\hbar^2}{9} S(S+1). \tag{3.126}$$

Actually, in Fig. 3.8, the second order cumulant of the profile is close to $\frac{S_c(S_c+1)}{9S_c^2} \simeq 0.122$.

Let us look at Fig. 3.10 again and discuss the behavior around the flat profile which is seen in the weak coupling region of the figure. The flat distribution is achieved, as discussed before, in the decoupling region. The magnetic field is much stronger than the coupling, though it is not so strong as to give rise to pseudo-crossing between states of different R. Hence, we need two assumptions for calculating the magnetic field or coupling dependence of $\langle \hat{S}_z \rangle^2$ by perturbation of the coupling. The first one is that the magnetic field is much larger than the coupling,

$$g_s B\hbar S \gg u', \tag{3.127}$$

to assume the decoupling of the super-spin from the cluster. The second assumption is that the magnetic field is weaker than the energy difference between the states of different R,

$$g_s B\hbar S < \frac{\hbar^2}{2\mathcal{J}} 2R_{\rm eff}, \tag{3.128}$$

which assures that the pseudo-crossing do not occur at least for levels having typical angular momentum. A detailed account of the calculation is presented in Appendix A.3. Here we give just the result, Eq. (A.46):

$$\langle \hat{S}_z \rangle^2_{\rm rn.av.} \simeq \frac{1}{3}\hbar^2 S(S+1) - \frac{64}{1215}\left(\frac{u'}{Bg_s}\right)^2 + \left\{\frac{4}{135}\hbar^2\left(\frac{-190+39S(S+1)}{693}\right) - \frac{4}{3645}\hbar^2 S(S+1)\right\}\left(\frac{u'}{k_{\rm B}T}\right)^2. \tag{3.129}$$

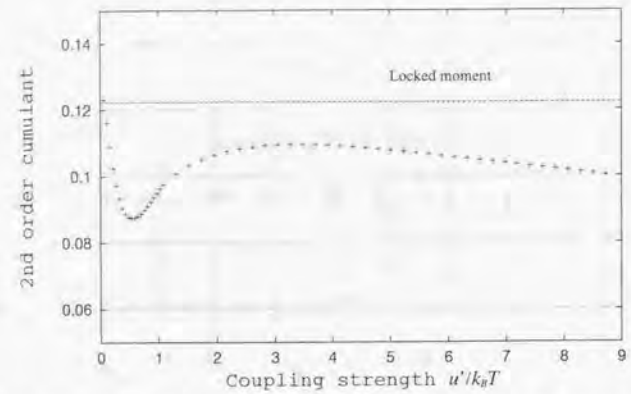

Figure 3.8: The second order cumulant of the profile as a function of the ratio of coupling strength u' and temperature k_BT. The temperature is fixed at 20.

When one analyzes the experiment in more detail, the higher-order cumulants may bring about important information. For example, the third order cumulant (Fig. 3.11) characterizes the asymmetry of the profile. In the whole range of magnetic field, the third order cumulant is smaller than the second order cumulant and is smaller as the coupling becomes stronger. The profiles are always symmetric with respect to $\langle S_z \rangle = 0$ in the absence of a magnetic field. When the magnetic field is applied, the asymmetry grows on account of time reversal symmetry breaking. The third order cumulant have a peak at $g_s B\hbar S/k_BT \simeq 2$. In a strong magnetic field, the profiles has a narrow peak at $\frac{\langle S_z \rangle}{S} = 1$ like Fig. 3.5. The profiles are more likely to be symmetric but still not quite. In other words, the third-order cumulant decreases but is not equal to zero.

Finally, we discuss the analysis of the experiment using the present model. To characterize the profiles, we select the first and the second order cumulant. The first and the second order cumulant of experimental profile are fitted by the cumulants calculated using the present model. We first discuss the gadolinium clusters. Considering the symmetry of the magnetic anisotropy coupling of bulk gadolinium, we apply the quadrupole coupling. Figure 3.12 and 3.13 illustrate the first and the second order cumulants of the profile for Gd_{23} and Gd_{17} clusters, respectively. The ratio of temperature and magnetic field $x = \frac{\mu B}{k_BT}$ is constant along the solid line. The coupling u' do not alter on the dotted

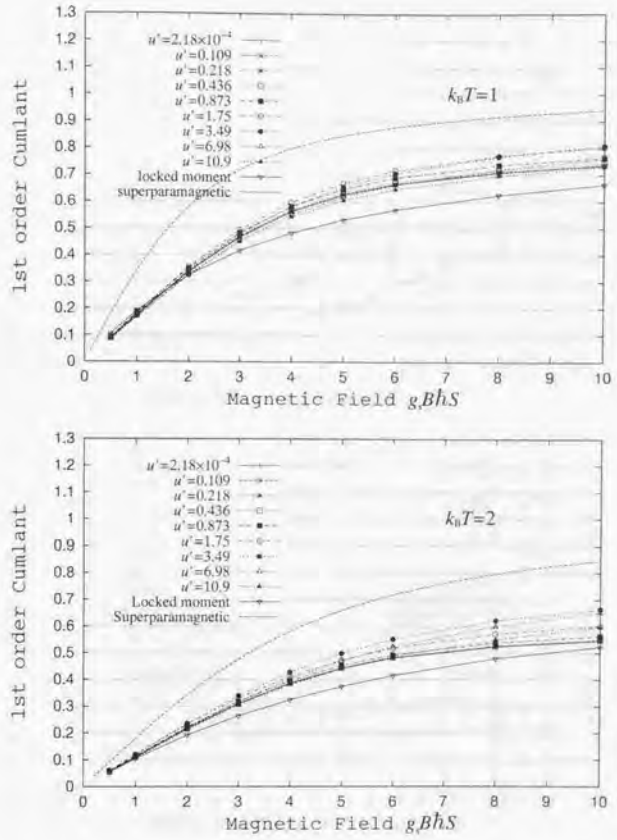

Figure 3.9: The first order cumulant of each profile as a function of the magnetic field $g_sB\hbar S$. The temperature k_BT is fixed at 1 and 2 for Fig. 7a and Fig. 7b respectively.

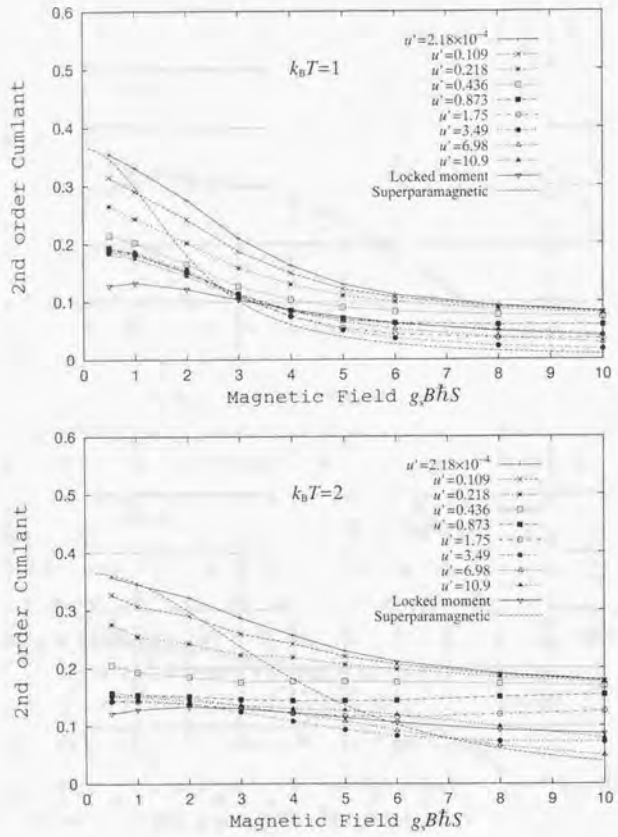

Figure 3.10: The second order cumulant of each profile as a function of the magnetic field $g_s B\hbar S$. The temperature $k_B T$ is fixed at 1 and 2 for Fig. 8a and Fig. 8b respectively.

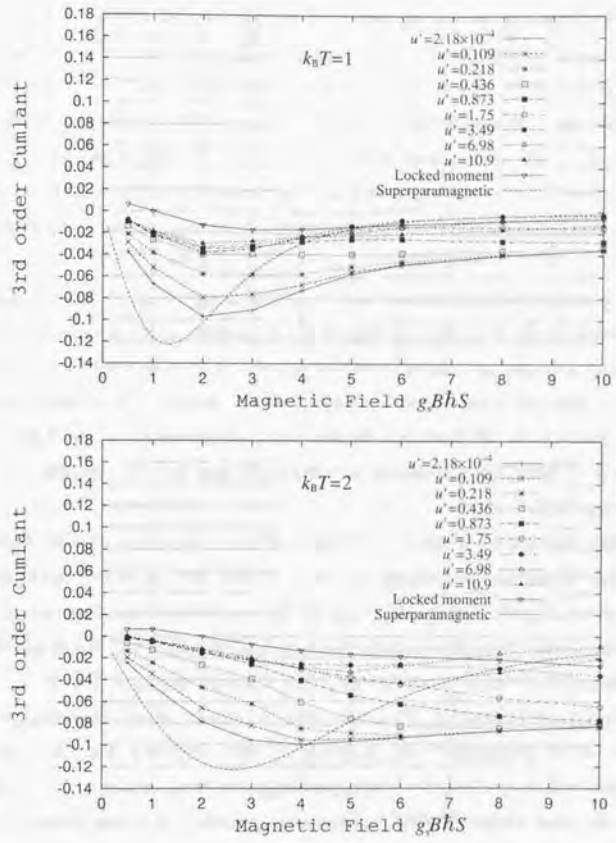

Figure 3.11: The third order cumulant of each profile as a function of the magnetic field $g_s B\hbar S$. The temperature $k_B T$ is fixed at 1 and 2 for Fig. 9a and Fig. 9b respectively.

line. The coupling parameter q which is defined through the relation $u' = (2.5)^q$.

We set the temperature $k_BT = 10$ for the numerical calculation. The rotational temperature extracted by the locked moment model is estimated as $T = 5 \pm 3$[K]. On the other hand, the unit of the energy parameters in the present model is about 5×10^{-2}[K]. The temperature of the experiment is order of 10^2 in our unit. The cumulants in high temperature is scaled by the ratio of temperature and magnetic field. We fixed the temperature $k_BT = 10$ for the numerical calculation, in which scaling low is fairly fulfilled.

The result of the analysis is shown in Fig. 3.15 for Gd_{17} and Fig. 3.14 for Gd_{23}. In both figures the analysis based on the locked moment model is also illustrated. The intermediate coupling model gives a better fitting than the analysis of locked moment model.

We now analyze Gd_{17} cluster at the vibrational temperature $T_{\rm vib} = 147$[K]. We fit the first and second order cumulant of the calculated profile. The magnetic moment and the anisotropic coupling u' of Gd_{17} is extracted as $1.49 - 1.78\mu_B$/atom and $\frac{u'}{k_BT} = 0.82 - 12.9$, where the rotational temperature is fixed to $T_{\rm rot} = 8.56$[K]. Comparing the profiles of various temperatures, we estimate the rotational temperature $T_{\rm rot} = 5.99 - 12.2$. The best quality of fitting is achieved at $\mu = 1.69\mu_B$/atom and $\frac{u'}{k_BT} = 3.65$. The profile is shown in Fig. 3.15.

For Gd_{23} cluster, we extract $\mu = 1.42 - 1.56\mu_B$/atom and $\frac{u'}{k_BT} = 1.56 - 7.43$ for the magnetic moment and the coupling, respectively. The rotational temperature of the cluster is set to $T_{\rm rot} = 5.5$[K]. The range of the temperature is estimated by comparing the theoretical and the experimental profile as $T_{\rm rot} = 4.65 - 6.51$[K]. Figure 3.14 shows the best fit profile which is realized at $\mu = 1.49\mu_B$/atom and $\frac{u'}{k_BT} = 4.09$.

As we reviewed in Sec. 2.3, the behavior of the gadolinium clusters changes according to its size. D.C. Douglass *et al.* discussed in Ref. [13] that Gd_{23} and Gd_{22} clusters behaves like locked moment and superparamagnetic, respectively. They suggest from their experimental profile that Gd_{17} clusters undergoes a transition from locked-moment behavior at a low temperature to superparamagnetic behavior at a high temperature. The total anisotropic coupling of the cluster for Gd_{23}, $\frac{u'}{k_BT} = 1.03 \times 23/5.5 = 4.30$, is larger than that of Gd_{17}, $\frac{u'}{k_BT} = 1.83 \times 17/8.56 = 3.63$. The results support the result of the experiment by Bloomfield *et al.* [13].

Bloomfield and coworkers extract the magnetic moment using the locked moment model. The results are 1.42 and 1.1 μ_B/atom for Gd_{23} and Gd_{17}, respectively. Reflecting

	$\mu[\mu_B/\text{atom}]$	u'/k_BT	u'[K/atom]
Gd_{23}(Quadrupole)	1.50 (1.42 - 1.56)	4.29 (1.56 - 7.43)	1.03 (0.373 - 1.78)
Gd_{23}(Cubic)	1.42 (1.30 - 1.56)	0.851 (0.75 - –)	0.203 (0.179 - –)
Gd_{17}	1.69 (1.49 - 1.78)	3.65 (0.82 - 12.9)	1.84 (0.41 - 6.49)
$Fe_{120-140}$	0.613 (0.581 - 0.650)	0.655 (0.327 - 1.75)	0.0252 (0.0126 - 0.0683)

Table 3.2: The result of analysis using the intermediate coupling model

the intermediate behavior, the magnetic moment of Gd_{17} is considerably changed from the result of the locked moment model. The magnetic moment of Gd_{23} is almost same as the result of analysis using the locked moment model.

Next we analyzed the experiment for Gd_{23} using a different potential. We apply the cubic symmetry for the anisotropic potential. The experimental temperature is set to T=5[K] according to Ref. [14]. Fitting the magnetic susceptibility and the second order cumulant, the magnetic moment can be estimated as 1.30 - 1.56 μ_B/atom. The anisotropic coupling u' is extracted to be larger than 0.163. The best-fitting is obtained at $1.42\mu_B$/atom and 0.185 [K/atom] for the magnetic moment and the coupling u', respectively. The ratio of temperature and magnetic field becomes $\frac{g_L B\hbar S}{k_BT} = 0.593$. In the Figure 3.16, we show the fitted profile and the profile of locked moment. For both theoretical profile, the ratio of temperature and the magnetic field are same. The temperature for the present model is set to $k_BT = 2$. For the cubic coupling, the profile of the present model makes a better agreement with experiment than one of the locked moment.

The magnitude of coupling seems to be different according to the symmetry of potential. But this is simply because of our definition of the anisotropic potential. The depth of potential is given by $\frac{2}{3}u'$ and $\frac{8}{3}u'$ for the quadrupole and the cubic symmetry, respectively. The depth of potential for the quadrupole and the cubic symmetry can be estimated as 0.687 and 0.541 [K/atom], respectively. These depth are similar at the extracted strength of coupling.

The extracted moment is much smaller than one of the bulk ($7.55\mu_B$/atom). It can be explained by the non-collinear configuration of the local spins [54]. The magnetism of rare-earth elements is associated with the 4f electrons which is localized to the atoms. The local 4f electrons are interacted through the indirect exchange RKKY interactions mediated by conduction electrons. The interaction oscillates as a function of distance, which cause helical structure in the bulk 4f rare-earth metals. Though the magnetic structure of the bulk Gd is ferromagnetic below the Curie temperature, the structure

can be changed for the clusters. Actually, it is found a magnetic reconstruction at the Gd(0001) surface [55]. Antiferromagnetic coupling at the surface is predicted along with a 6.3% expansion of the first layer spacing in recent calculations [56]. The subsequent IV-LEED studies show that the first layer spacing is actually contracted by 2.4%, with a 1% second layer spacing expansion [57]. Then, it is possible to assume that the nearest-neighbor coupling J and the next nearest-neighbor coupling K becomes ferromagnetic and antiferromagnetic, respectively. The atoms lie at a surface are affected by K due to the low coordination number. They calculated the Heisenberg model with exchange coupling J and K which favors parallel and antiparallel direction, respectively. The model calculations predict that the strong exchange antiferromagnetic coupling K leads a noncollinear configuration of the local magnetic moment.

We next apply the intermediate coupling model to iron clusters. Since the magnetic anisotropy of bulk iron is much smaller than one of the gadolinium, the iron cluster is considered to be superparamagnetic. The symmetry of anisotropic potential is assumed to cubic which is observed in magnetic anisotropy potential of bulk iron. The result of analysis is illustrated in Fig. 3.17 for the profile of iron. In this figure, we also show the profile in which the cluster's magnetic moment fixed to the bulk magnetic moment. The fitting of the profile using the intermediate coupling model is better than the profile of bulk. The position of peak for the bulk profile appears at strong field side far from the position of peak for the experimental profile. We extract 0.581 - 0.650 μ_B/atom and 12.6 - 67.3 [mK/atom] for the magnetic moment and anisotropic coupling u', respectively. The quality of fitting is best when the magnetic moment and anisotropic coupling u' are 0.613μ_B/atom and 25.2 [mK/atom], respectively. The anisotropic coupling is much smaller than one in the gadolinium clusters and is comparable to one of the bulk iron (36 [mK/atom]). On the contrary, the magnetic moment analyzed by the superparamagnetism is larger than the magnetic moment of bulk iron (2.2μ_B/atom).

While first-principle approach for the $Fe_{120-140}$ clusters is not reported, there are many papers for smaller size ($N < 20$) of iron clusters. These papers predict that magnetic moment of clusters is larger than the bulk [58, 59, 60]. However, γ phase of bulk iron seems to be antiferromagnetic in the low temperature of which magnetic moment 0.7μ_B/atom [61]. The antiferromagnetic phase is observed in the fine particles of iron. The calculation based on the tight binding Hubbard Hamiltonian predict the antiferromagnetic phase of iron, which is smaller than the bulk magnetic moment [62].

Another possible explanation for the result is that the surface local magnetic moment may cause the canted structure of the magnetic moments. For all theoretical calculation performed so far, the local moment did not take into account. We need a further study like a first principle calculation to confirm the smaller magnetic moment in the iron clusters.

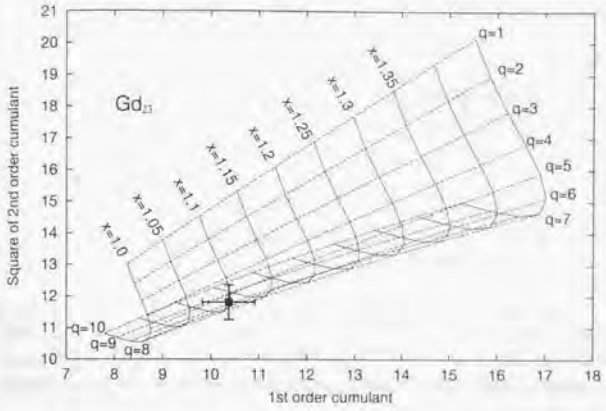

Figure 3.12: The first and second order cumulant of Gd_{23} clusters. $x = \frac{\mu B}{k_B T}$ and $u' = (2.5)^q$ is constant along the dotted and solid line, respectively. The temperature is fixed at $T = 5.5$K. The magnetic moment of the cluster is $\mu = 30.7x\mu_B$ The experimental data is calculated from the experimental profile in Ref. [14]. Error bars are estimated from the error bars of magnetization in the same reference (Fig. 2.14).

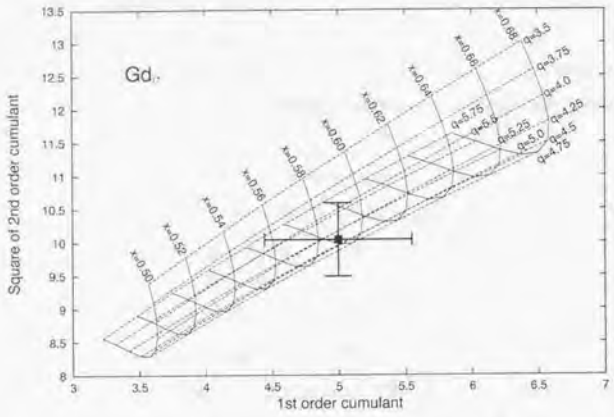

Figure 3.13: The first and second order cumulant of Gd_{17} clusters. $x = \frac{\mu B}{k_B T}$ and $u' = (2.5)^q$ is constant along the dotted and solid line, respectively. The temperature is fixed at $T = 8.56$K. The magnetic moment of the cluster is $\mu = 47.7 x \mu_B$. The experimental data is calculated from the experimental profile in Ref. [14]. Error bars are estimated from the error bars of magnetization in the same reference (Fig. 2.14).

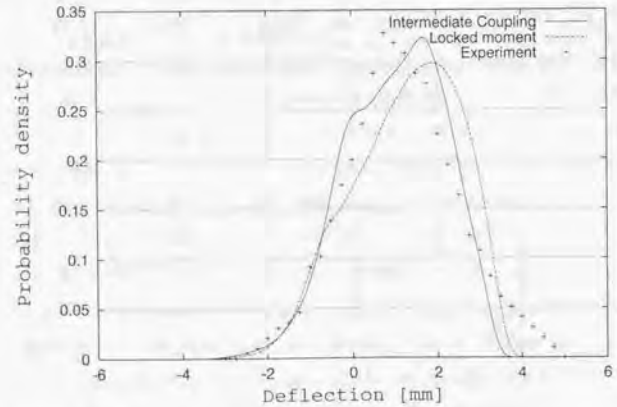

Figure 3.14: The profile of experiment and intermediate coupling model for Gd_{23} clusters. We set $\frac{g_s B \hbar S}{k_B T} = 1.13$ and $k_B T = 10$. The ratio of coupling to temperature $\frac{u'}{k_B T}$ is set to 4.29. The profile of locked moment model is also illustrated. We set $\frac{g_s B \hbar S}{k_B T} = 1.45$.

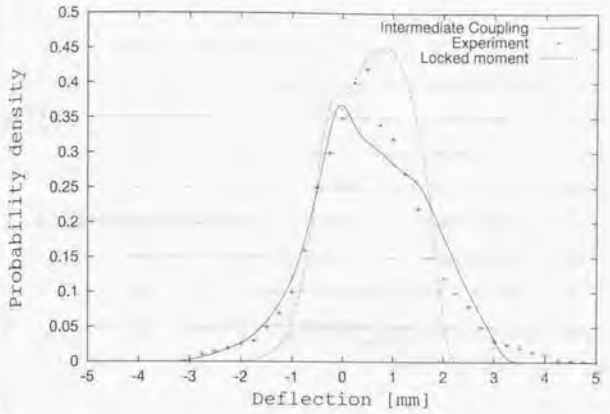

Figure 3.15: The profile of experiment and intermediate coupling model for Gd_{17} clusters. We set $\frac{g_s B \hbar S}{k_B T} = 0.60$ and $k_B T = 10$. The ratio of coupling to temperature $\frac{u'}{k_B T}$ is set to 3.65. The profile of locked moment model is also illustrated. We set $\frac{g_s B \hbar S}{k_B T} = 1.5$.

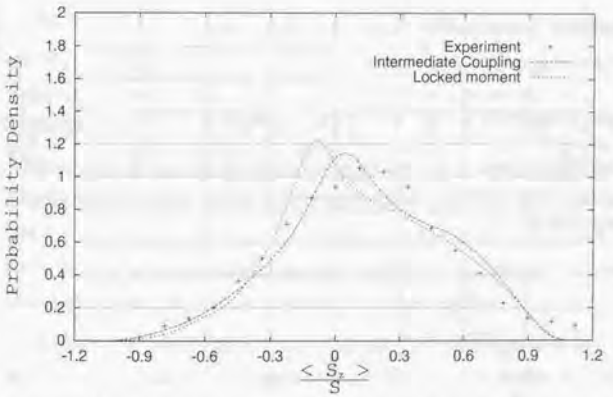

Figure 3.16: The profile of experiment and two theoretical models with the same parameter. We set $\frac{g_s B \hbar S}{k_B T} = 0.593$ for both theoretical models and $k_B T = 2$ for intermediate coupling model. The ratio of coupling to temperature $\frac{u'}{k_B T}$ is set to 0.851

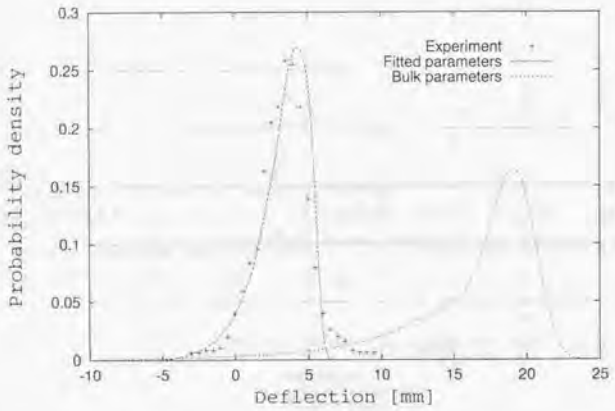

Figure 3.17: The profile of experiment and intermediate coupling model for $Fe_{120-140}$ clusters. We set $\frac{g_i B\hbar S}{k_B T} = 3.92$ and $k_B T = 1$. The ratio of coupling to temperature $\frac{a'}{k_B T}$ is set to 1.53. Both lines are calculated by the intermediate coupling model. The anisotropic coupling and the magnetic moment is fixed to bulk value in "Bulk parameters". These parameters are fitted to the experiment in "Fitted parameters".

Chapter 4

Conclusions

Using the intermediate coupling model, we have studied the magnetization of ferromagnetic clusters in a Stern-Gerlach magnet. In this model the super-electron spin couples to the cluster ions through an anisotropic potential. This model is expected to describe the intermediate behavior between the superparamagnetic and the locked moment. In evaluating the profiles or the magnetization, we assume that the variation of the magnetic field in entering the magnet is slow in time, i.e., adiabatic. Hence, any transition between quantum states is suppressed; the occupation probability of each quantum state is determined in the source area where the magnetic field is absent.

We examined the magnetic susceptibility of the present model applying the perturbation theory. Especially, the magnetic susceptibility in the strong and weak coupling limits is discussed analytically. We expected the intermediate coupling model to approach the locked moment behavior in the strong coupling limit. However, there is a crucial difference between the strong coupling limit of the present model and the locked moment model. In the present model the super-electron spin degree of freedom is treated explicitly and the Coriolis term arises due to the conservation of total angular momentum, while in the locked moment model the Coriolis term is neglected. Consequently, the magnetic susceptibility is always smaller than the locked moment.

The susceptibility in the weak coupling limit coincides with one of the locked moment model. The coincidence originates from the internal symmetry of the rotor. Actually we calculate the susceptibility of the deformed clusters in the limit of low spin angular momentum analytically. The analysis shows that these two limits are different when the cluster is deformed. The susceptibility in the present model obtained by the perturbation theory is not equal to the superparamagnetic value in any range of the coupling. The

position of peak observed around the coupling where the super-spin starts to confine to the anisotropic potential minimum for the typical angular momentum.

We find that the irregular magnetic field response noticed in Ref. [8] also exists in the weak coupling region of the present model. The magnetization linearly increases before the decoupling and saturates after the decoupling. Then, once the pseudo-crossing between levels in different R occurs, the magnetization increases again. Before the decoupling, the susceptibility arises as a perturbation of the magnetic field. But after the decoupling, or once the pseudo-crossing takes place, the susceptibility becomes nonperturbative. Instead, we need to diagonalize the total Hamiltonian, which is difficult for today's computers for high temperatures and large cut off angular momentum. In Ref. [8], Visuthikraisee and Bertsch discussed the susceptibility after the decoupling using uniaxial coupling. They found that the susceptibility reaches the superparamagnetic value. Therefore, if we were to calculate the susceptibility after the decoupling, the susceptibility for the cubic symmetric potential would be superparamagnetic.

While an anomalous temperature dependence is reported in Ref. [26], the calculated susceptibility is always positive. We could not reproduce the anomalous temperature dependence.

The "superparamagnetic peak" which is seen in the profile obtained by the locked moment model is not seen in the present calculation even in the strong coupling limit. As discussed in Sec. 3.3.3, the strong coupling limit of our model is different from the locked moment model because of the Coriolis term. It suggests that the effect of the Coriolis term destroys the superparamagnetic peak. We calculated the profile in the low temperature for the quadrupole coupling and find that the peak does not appear. If we would be able to calculate in such high temperature that the Coriolis term can be negligible, the peak would appear in the deflection profile even in the cubic symmetric coupling.

Finally, we discuss how to analyze the Stern-Gerlach deflection function by our theory. We calculated the cumulant of the profiles up to the third order to characterize the profiles. We found from Fig. 3.9 that the first and second order cumulants are dominant. In particular, evaluation of the susceptibility and second order cumulant by the perturbation technique gave us the analytical expression of the second order cumulant and magnetic susceptibility for high temperature and the strong or weak coupling. One can extract the magnetic moment and the coupling strength by fitting the observed magnetic susceptibility and the second order cumulant into the calculated second order cumulant and the magnetic susceptibility.

For example, we analyze the experiment of Gd_{17}, Gd_{23} and $Fe_{120-140}$. We obtain better agreement than the locked moment model for Gd_{23}. The extracted anisotropic coupling in Gd_{17} is smaller than the coupling of Gd_{23}. The result agrees with the result of experiment [15]. The analysis of profiles become a better fit than the profile calculated by the magnetic moment and coupling for the bulk.

The extracted magnetic moment of gadolinium clusters are much smaller than one of the bulk gadolinium, which indicate the noncollinear configuration of local magnetic moment. The profile of iron clusters can be fitted by the intermediate coupling model. The magnetic moment is again smaller than one of the bulk iron. The antiferromagnetic coupling, like a γ phase of iron, may support small moment of iron clusters. Otherwise, it suggests that the localized surface spin cause a canted configuration of the iron clusters. These configurations of spins decrease the total magnetic moment of iron clusters. To confirm the results, we need further study like a first-principle calculation including the effect of local magnetic moment.

Acknowledgments

I would like to thank my thesis advisor Professor N. Onishi for many instructive discussions and his constant encouragement during my course. I wish to express my gratitude to Professor G. Bertsch for a fruitful collaboration and discussions. I gratefully acknowledge helpful discussions with Professor N. Tajima especially on the various coupling schemes. I wish to thank M. Kaneda and Professor A. Ansari for their helpful advice. I would like to thank Professor K. Matusyanagi for discussions on the boson expansion of angular momentum. I acknowledge useful discussions with thank V. Kondratyev and P. Jensen. I especially would to thank Professor K. Yabana for his valuable comments and advises on my dissertation. I would like to thank Professor A. Bulgac for letting him participate to the program "Atomic Clusters" (INT-98-2). Part of the calculations were performed with a computer VPP500 at RIKEN (Research Institute for Physical and Chemical Research, Japan) and SX4 at RCNP (Research Center of Nuclear Physics).

I would like to thank the members of the particle and nuclear theory group for their warm support and help which made difficult times easier, especially, M. Ohtani for his constant encouragement and discussions, many advises on presentations. I would like to thank Dr. M. Oi for discussions and valuable advises on the writing the doctor thesis. I would also thank to Dr. S. Takahara, Dr. T. Hotta for many useful tips and tricks of the computer. Special thanks to go to T. Hara for tips on LaTeX and postscript documents, which made my work progress much smoother.

Appendix A

A.1 Angular momentum

The main purpose of this appendix is to provide some useful relations used in this thesis. The fundamental commutation relation between components of angular momentum is

$$[J_i, J_j] = i\epsilon_{ijk}J_k. \tag{A.1}$$

an eigenstate of the angular momentum is labeled by the size of angular momentum J and the projection of the angular momentum M on the quantized axis z:

$$\begin{aligned} J^2|JM\rangle =& J(J+1)|JM\rangle, \quad J_k|JM\rangle = M|JM\rangle. \\ & (J = 0, 1, 2, \cdots, \quad M = -J, -J+1, \cdots, J) \end{aligned} \tag{A.2}$$

In the case of three dimensional rotation, we user the Euler angles $\Omega = (\alpha, \beta, \gamma)$[44]. Under a rotation of the coordinate frame around angles Ω the wavefunctions transformed to

$$|\Psi'\rangle = R(\Omega)|\Psi\rangle, \tag{A.3}$$

with the unitary rotational operator

$$R(\Omega) = e^{i\alpha J_z}e^{i\beta J_y}e^{i\gamma J_z}. \tag{A.4}$$

The Wigner $\mathcal{D}$-functions are defined as

$$\mathcal{D}^{\lambda}_{\mu\mu'}(\Omega) = \langle\lambda\mu'|R(\Omega)|\lambda\mu\rangle. \tag{A.5}$$

Corresponding the transformation (A.4), we can define the spherical vector and tensor operators T:

$$T_{\lambda\mu} = R(\Omega)T_{\lambda\mu}R^{\dagger}(\Omega) = \mathcal{D}^{\lambda}_{\mu'\mu}T_{\lambda\mu'}. \tag{A.6}$$

Because two successive finite rotations are represented by a single finite rotation of different angle. The $\mathcal{D}$ function itself behaves as a spherical tenser. The commutation relations between J and an arbitrary spherical tensor $T_{\mu\nu}$ can be expressed in the form

$$[I_\mu, T_{\lambda\mu'}] = \sqrt{\lambda(\lambda+1)}\langle\lambda\mu' 1\mu|\lambda\ \mu+\mu'\rangle T_{\lambda\mu+\mu'}. \tag{A.7}$$

The angular momentum behaves as a spherical tensor of rank one:

$$(J_1, J_0, J_{-1}) = (\frac{1}{\sqrt{2}}(J_x - iJ_y), J_z, -\frac{1}{\sqrt{2}}(J_x + iJ_y)), \tag{A.8}$$

$$J_\nu = T_{i\nu}J_i, \quad \text{where } T_{i\nu} = \frac{1}{\sqrt{2}}\begin{pmatrix} 1 & -i & 0 \\ 0 & 0 & \sqrt{2} \\ -1 & -i & 0 \end{pmatrix}. \tag{A.9}$$

For an arbitrary tensor operator $T_{\lambda\mu}$ we can define intrinsic components $T'_{\lambda\mu}$ through the relation;

$$T_{\lambda\mu} = \sum_\nu \mathcal{D}^\lambda_{\mu\nu}(\Omega)T'_{\lambda\nu}, \tag{A.10}$$

$$T'_{\lambda\mu} = \sum_\mu \mathcal{D}^{*\lambda}_{\mu\nu}(\Omega)T_{\lambda\nu}. \tag{A.11}$$

The angular momentum component in the body-fixed frame J'_μ is defined as

$$J'_\mu = \mathcal{D}^1_{\mu'\mu}J_{\mu'}. \tag{A.12}$$

It can be written in intrinsic component of angular momentum,

$$(I'_1, I'_0, I'_{-1}) = (-\frac{1}{\sqrt{2}}(I'_1 + iI'_2), I'_3, \frac{1}{\sqrt{2}}(I'_1 - iI'_2)), \tag{A.13}$$

$$I'_\nu = T'_{i\nu}I'_i, \quad \text{where } T_{i\nu} = \frac{1}{\sqrt{2}}\begin{pmatrix} -1 & -i & 0 \\ 0 & 0 & \sqrt{2} \\ 1 & -i & 0 \end{pmatrix}. \tag{A.14}$$

The commutation rule of angular momentum in the body-fixed frame can be calculated:

$$[J'_i, J'_j] = -i\epsilon_{ijk}J'_k, \tag{A.15}$$

which is different from the commutation rule of angular momentum in the space-fixed frame by sign. The commutation relation between angular momentum and intrinsic component of spherical tensor is expressed as

$$[J'_\nu, T^\lambda_{\mu\nu'}(\Omega)] = (-1)^\nu\sqrt{\lambda(\lambda+1)}\langle\lambda\mu' 1\ -\nu|\lambda\ \nu'-\nu\rangle T^\lambda_{\mu\ \nu'-\nu}. \tag{A.16}$$

We introduced three kind of angular momentum R,S and $I = R+S$ in the intermediate coupling model. The commutation relation of the momentum can be calculated using commutation relations described above. The commutation relation between the space fixed component;

$$[R_i, R_j] = i\epsilon_{ijk}R_k, \quad [S_i, R_j] = 0, \qquad [I_i, R_j] = i\epsilon_{ijk}R_k, \tag{A.17}$$

$$[S_i, S_j] = i\epsilon_{ijk}S_k, \quad [I_i, S_j] = i\epsilon_{ijk}S_k, \tag{A.18}$$

$$[I_i, I_j] = i\epsilon_{ijk}I_k. \tag{A.19}$$

For the body-fixed frame, the commutation relation is calculated:

$$[R'_i, R'_j] = -i\epsilon_{ijk}R'_k, \quad [S'_i, R'_j] = -i\epsilon_{ijk}R'_k, \quad [I'_i, R'_j] = -i\epsilon_{ijk}I'_k, \tag{A.20}$$

$$[S'_i, S'_j] = -i\epsilon_{ijk}S'_k, \quad [I'_i, S'_j] = 0, \tag{A.21}$$

$$[I'_i, I'_j] = -i\epsilon_{ijk}I'_k. \tag{A.22}$$

We should note that the relations are quite different for the commutation relations between different kinds of angular momentum. The commutation relations between same kinds of angular momentum differ one of the space fixed frame by a minus sign.

The commutation relations between angular momentum of different frame are calculated as

$$[R'_i, R_j] = 0, \quad [S'_i, R_j] = [I'_i, R_j] \neq 0, \tag{A.23}$$

$$[R'_i, S_j] = 0, \quad [S'_i, S_j] = [I'_i, S_j] \neq 0, \tag{A.24}$$

$$[R'_i, I_j] = 0, \quad [S'_i, I_j] = [I'_i, I_j] = 0. \tag{A.25}$$

A.2 The derivation of susceptibility for the locked moment limit

In this appendix, we show the derivation of the susceptibility for the locked moment limit [Eq. (3.101)]. In Sec. 3.3.1, we supposed that the susceptibility was described by the ground band only. The assumption is valid if the band head of excited bands is much higher than the energy of the cut off level, that is,

$$u'(E^{\mathrm{A}}_N - E^{\mathrm{A}}_1) \gg \frac{\hbar^2\{I_c(T)\}^2}{2\mathcal{J}}, \tag{A.26}$$

where $N \geq 7$ because the ground band consists of six-fold degenerate levels.

The wave function and the energy shift of Coriolis term for the ground band were already discussed and turn out to be Eq. (3.99) and Eq. (3.100), respectively. The energy level of the ground band results in

$$E_{IMKi} \simeq \frac{\hbar^2}{2\mathcal{J}}(I(I+1)+S(S+1)) + \frac{\hbar^2}{2\mathcal{J}}MK + u' E_i^{\mathrm{A}} \quad (i \le 6). \tag{A.27}$$

The susceptibility is evaluated through Eq. (3.92) as

$$\chi \simeq -\frac{2}{Z(T)} \sum_{IMKi} \sum_{I'K'i'} \frac{|\langle I'MK'i'|\hat{S}_z|IMKi\rangle|^2}{a(I(I+1)-I'(I'+1)-(MK-MK')) - u'(E_i^{\mathrm{A}} - E_{i'}^{\mathrm{A}})} \exp\left(-\frac{E_{IMKi}}{k_{\mathrm{B}}T}\right) \tag{A.28}$$

where $a = \hbar^2/2\mathcal{J}$. The second term of energy denominator, $E_i^{\mathrm{A}} - E_{i'}^{\mathrm{A}}$, vanishes because of the 6-fold degeneracy of ground band. The matrix element of $\hat{S}_z$ is evaluated by the wave function of the ground band Eq. (3.99),

$$|\langle I'MK'i'|\hat{S}_z|IMKi\rangle|^2 = \delta_{KK'}\delta_{ii'}\hbar^2 S^2 \frac{2I+1}{2I'+1} |\langle IM10|I'M\rangle|^2 |\langle IK10|I'K\rangle|^2 \tag{A.29}$$

One should note that the matrix element is same as the one of the locked moment model [6]. Substituting Eq. (A.29) into Eq. (A.28), we get

$$\chi \simeq -\frac{1}{Z(T)} \sum_{IMKi} \sum_{I'} 4\mathcal{J} \frac{S^2 \frac{2I+1}{2I'+1} |\langle IM10|I'M\rangle|^2 |\langle IK10|I'K\rangle|^2}{I(I+1) - I'(I'+1)} \times \exp\left(-\frac{a\hbar^2(I(I+1)+S(S+1)+2KS) + uE_i^{\mathrm{A}}}{k_{\mathrm{B}}T}\right). \tag{A.30}$$

This is different from the susceptibility for the locked moment [6] only in the Coriolis term. Since the average angular momentum is about $I \simeq 600$, one can safely evaluate Eq. (A.30), treating I, K as a continuous variable and replacing the sum by an integral. Thus we get

$$\begin{aligned} \chi &\simeq \frac{2\mathcal{J}}{3}\left(1 - \frac{e^{-\beta' S^2}}{S}\int_0^S e^{\beta' t^2} dt\right) = \sum_{n=0}^{\infty} \frac{2\mathcal{J}}{3\hbar^2} \frac{(-1)^n 2^n}{(2n+3)!!} (\beta' S^2)^{n+1} \\ &= \frac{2}{9}\frac{\hbar^2 S^2}{k_{\mathrm{B}}T}\left(1 - \frac{2}{5}\beta' S^2 + \frac{4}{35}\left(\beta' S^2\right)^2 + \cdots\right) < \frac{2}{9}\frac{\hbar^2 S^2}{k_{\mathrm{B}}T}, \end{aligned} \tag{A.31}$$

where $\beta' = \frac{\hbar^2}{2\mathcal{J}k_{\mathrm{B}}T}$.

A.3 The second order cumulant for the decoupling regime

The ensemble average of the second order cumulant is determined by $\langle \hat{S}_z \rangle^2$ of each level in the a magnetic field and the energy in the absence of magnetic field. We first calculate the wave function in the decoupling region using the perturbation for the coupling.

According to Eq. (3.127), the coupling is much weaker than the magnetic field. If the coupling were to vanish, the super-spin is completely decoupled from the cluster and precess about the direction of the magnetic field independently of the rotor. Thus, the wave function of super-spin becomes $|S\sigma\rangle$, and one of the clusters is a linear combination of $\mathcal{D}^R_{\mu k}(\Omega)$ for intrinsic quantum number k. The total wave function is constructed as direct product of them.

The actual wave function is not decoupled but perturbed by the weak coupling. The matrix element of the coupling Hamiltonian of degenerate space $(H_{\mathrm{coupl}})^{R\mu\sigma}_{k,k'}$ can be calculated as

$$(H_{\mathrm{coupl}})^{R\mu\sigma}_{k,k'} = A_\kappa \langle Rk4\kappa|Rk'\rangle \langle R\mu 40|R\mu\rangle \langle S\sigma 40|S\sigma\rangle. \tag{A.32}$$

According to the perturbation theory for degenerate case, the unperturbed base $\Psi^{(0)}_{RM\sigma\nu}$ is obtained as the eigenstates of $(H_{\mathrm{coupl}})^{R\mu\sigma}_{k,k'}$:

$$\Psi^{(0)}_{RM\sigma\nu} = \sqrt{\frac{2R+1}{8\pi^2}} c^\nu_k \mathcal{D}^R_{\mu k}(\Omega) \otimes |S\sigma\rangle, \quad M = \mu + \sigma. \tag{A.33}$$

We further take into account the coupling up to the second-order perturbation. If we apply second-order perturbation naively, the wave function (A.33) is mixed with the state of different σ and one in different R. But we can neglect the mixing with states in different R because of Eq. (3.128) in which the energy differences between states of different R are much larger than the magnetic field. The perturbed wave function $\Psi^{(2)}_{RM\sigma\nu}$ can be evaluated as

$$\begin{aligned} \Psi^{(2)}_{RM\sigma\nu} &= \left\{1 - \frac{u_{\mathrm{B}}^2}{2}\sum_{\sigma\neq\sigma'} \frac{|\langle \Psi^{(0)}_{RM\sigma'\nu'}|H_{\mathrm{C}}|\Psi^{(0)}_{RM\sigma\nu}\rangle|^2}{(\sigma-\sigma')^2}\right\}\Psi^{(0)}_{RM\sigma\nu} \\ &\quad + u_{\mathrm{B}} \sum_{\sigma\neq\sigma'} \frac{\langle \Psi^{(0)}_{RM\sigma'\nu'}|H_{\mathrm{C}}|\Psi^{(0)}_{RM\sigma\nu}\rangle}{(\sigma-\sigma')} \Psi^{(0)}_{RM\sigma'\nu} + u_{\mathrm{B}}^2 \sum_{\sigma\neq\sigma'} (\text{const.}) \Psi^{(0)}_{RM\sigma'\nu}, \end{aligned} \tag{A.34}$$

where $u_{\mathrm{B}} = \frac{u'}{Bg_\hbar\hbar}$ and $H_{\mathrm{C}} = H_{\mathrm{coupl}}/u'$. Using the perturbed wave function Eq. (A.34), we

calculate $\langle \hat{S}_z \rangle^2$ up to second order for the coupling:

$$\frac{\langle \hat{S}_z \rangle^2}{\hbar^2} \simeq \sigma^2 + u_{\rm B}^2 C_2,$$
$$\text{where } C_2 = 2\sigma \sum_{\sigma \neq \sigma'} \frac{|\langle \Psi^{(0)}_{RM\sigma'\nu'} | H_{\rm C} | \Psi^{(0)}_{RM\sigma\nu} \rangle|^2}{(\sigma' - \sigma)}. \tag{A.35}$$

The energy in the absence of a magnetic field is also treated as a second order perturbation of the coupling. The first-order energy shift $u' \epsilon^{(1)}_{\nu R}$ is evaluated as the expectation value of $H_{\rm coupl}$ for the unperturbed state:

$$\epsilon^{(1)}_{\nu R} = \langle R\mu 40 | R\mu \rangle \langle S\sigma 40 | S\sigma \rangle \Delta_{\nu R}, \tag{A.36}$$

where $\Delta_{\nu R}$ represents the eigenvalue of $\left[h_{kk'} = \sum_{\kappa=0,\pm 4} \frac{A_\kappa}{u'} \langle Rk4\kappa | Rk' \rangle \right]$. We can neglect the second-order energy shift, since the second-order energy shift comes from the mixing with the states in different R.

We calculate the ensemble average of $\langle \hat{S}_z \rangle^2$ using Eq. (A.35) and Eq. (A.36). The Boltzmann factor is expanded for $u_{\rm T} = \frac{u'}{k_{\rm B}T}$. Neglecting terms higher than second order for $u_{\rm T}$ and $u_{\rm B}$, we obtain

$$\frac{\langle \hat{S}_z \rangle^2_{\rm enav}}{\hbar^2} \simeq \frac{\sum_{R\nu\sigma M} \left[\sigma^2 - u_{\rm T} \sigma^2 \epsilon^{(1)}_{\nu R} + \left\{ u_{\rm B}^2 C_2 + \frac{1}{2} u_1^2 \sigma^2 {\epsilon^{(1)}_{\nu R}}^2 + \cdots \right\} \right] \exp(-\beta E_R)}{\sum_{R\nu\sigma M} \left\{ 1 - u_{\rm T} \epsilon^{(1)}_{\nu R} + \frac{1}{2} u_{\rm T}^2 {\epsilon^{(1)}_{\nu R}}^2 + \cdots \right\} \exp(-\beta E_R)}. \tag{A.37}$$

The sum of $\epsilon^{(1)}_{\nu R}$ which is the eigenvalue of $(H_{\rm coupl})^{R\mu\sigma}_{k,k'}$ vanishes, since $(H_{\rm coupl})^{R\mu\sigma}_{k,k'}$ is a traceless matrix. Expansion of Eq. (A.37) up to second order of $u_{\rm T}$ and $u_{\rm B}$ yields

$$\frac{\langle \hat{S}_z \rangle^2_{\rm enav}}{\hbar^2} \simeq \frac{S(\sigma^2)}{S(1)} + \frac{S(C_2)}{S(1)} u_{\rm B}^2 + \frac{1}{2} \left(\frac{S(\sigma^2 {\epsilon^{(1)}_{\nu R}}^2)}{S(1)} - \frac{S({\epsilon^{(1)}_{\nu R}}^2) S(\sigma^2)}{S(1)^2} \right) u_{\rm T}^2, \tag{A.38}$$

where $S(x)$ is defined as

$$S(x) = \sum_{R\nu\sigma M} x \exp(-\beta E_R). \tag{A.39}$$

Let us estimate the $S(x)$'s appearing in Eq. (A.38):

$$S(1) = \sum_R (2S+1)(2R+1)^2 \exp(-\beta E_R), \tag{A.40}$$
$$S(\sigma^2) = \sum_R \frac{1}{3} S(S+1)(2S+1)(2R+1)^2 \exp(-\beta E_R). \tag{A.41}$$

Before calculating the other $S(x)$'s, we evaluate $\sum_\nu |\Delta_{\nu R}|^2$.

$$\sum_\nu |\Delta_{\nu R}|^2 = {\rm Tr}(h^2_{kk'}) = \sum_{\kappa=0,\pm 4} A_\kappa^2 |\langle R\ k+\kappa \mid 4\ \kappa\ R\ k \rangle|^2$$
$$= \frac{8(2R+1)}{15}. \tag{A.42}$$

Substituting Eq. (A.42), we make a calculation of the other $S(x)$'s

$$S({\epsilon^{(1)}_{\nu R}}^2) = \sum_R \frac{8(2R+1)}{15} \frac{2R+1}{9} \frac{2S+1}{9} \exp(-\beta E_R), \tag{A.43}$$
$$S(\sigma^2 {\epsilon^{(1)}_{\nu R}}^2) = \sum_R \frac{8(2R+1)}{15} \frac{2R+1}{9} \frac{(1+2S)(-190+39S(S+1))}{693} \exp(-\beta E_R), \tag{A.44}$$
$$S(C_2) = \sum_R \frac{8(2R+1)}{15} \frac{2R+1}{9} \frac{-8(2S+1)}{9} \exp(-\beta E_R). \tag{A.45}$$

Finally, putting Eqs. (A.40), (A.41), (A.43), (A.44) and (A.45) into Eq. (A.38), we obtain the ensemble average of $\langle \hat{S}_z \rangle^2$ as a function of the coupling strength

$$\langle \hat{S}_z \rangle^2_{\rm enav} \simeq \frac{1}{3}\hbar^2 S(S+1) - \frac{64}{1215} \left(\frac{u'}{B g_{\rm s}} \right)^2$$
$$+ \left\{ \frac{4}{135}\hbar^2 \left(\frac{-190+39S(S+1)}{693} \right) - \frac{4}{3645}\hbar^2 S(S+1) \right\} \left(\frac{u'}{k_{\rm B}T} \right)^2. \tag{A.46}$$

A.4 Derivation of the matrix element

A.4.1 Anisotropic interaction

The bases are obtained by the angular momentum coupling of $|S\sigma\rangle$ and $\mathcal{D}^R_{\mu k}(\Omega)$ to IM:

$$\Psi_{IM(Rk)} = \sum_\sigma \langle R\mu S\sigma | IM \rangle \sqrt{\frac{2R+1}{8\pi^2}} \mathcal{D}^R_{\mu k}(\Omega) |S\sigma\rangle. \tag{A.47}$$

The anisotropic interaction is

$$H_{\rm coupl}(\mathbf{S}, \Omega) = \sum_m A_\kappa \mathcal{D}^{4*}_{m\kappa}(\Omega) [S]^4_m. \tag{A.48}$$

The matrix element is defined as

$$\Psi^*_{IM(Rk)} H_{\rm C}(\mathbf{S}, \Omega) \Psi_{IM(Rk)} = \sum_{m\sigma\sigma'} \frac{\sqrt{(2R+1)(2R'+1)}}{8\pi^2}$$
$$\times \langle R'\mu' S\sigma' | IM \rangle \langle R\mu S\sigma | IM \rangle A_\kappa \langle S\sigma' | [S]^4_m | S\sigma \rangle$$
$$\times \int \mathcal{D}^{R'*}_{\mu' k'} \mathcal{D}^{4*}_{m\kappa} \mathcal{D}^R_{\mu k} d\Omega. \tag{A.49}$$

Using relation for $\mathcal{D}$-function $\int \mathcal{D}^{j_1*}_{\mu_1 m_1}\mathcal{D}^{j_2*}_{\mu_2 m_2}\mathcal{D}^{j_3}_{\mu_3 m_3}d\Omega = \frac{8\pi^2}{2j_3+1}\langle j_1\mu_1 j_2\mu_2|j_3\mu_3\rangle\langle j_1 m_1 j_2 m_2|j_3 m_3\rangle$ and Wigner-Eckart theorem, we get

$$\begin{aligned}
&= \sum_{m\sigma\sigma'} \frac{\sqrt{(2R+1)(2R'+1)}}{8\pi^2} \\
&\times \langle R'\mu' S\sigma'|IM\rangle\langle R\mu S\sigma|IM\rangle \frac{\langle S\sigma 4m|S\sigma'\rangle}{\sqrt{2S+1}} A_\kappa \langle S||[S]^4_m||S\rangle \\
&\frac{8\pi^2}{2R+1}\langle R'\mu' 4m|R\mu\rangle\langle R'k'4\kappa|RK\rangle. \qquad \text{(A.50)}
\end{aligned}$$

The three Clebsch-Gordan coefficient of the matrix element can be merged into the Racah coefficient using the formula,

$$\sum_\beta \langle a\alpha b\beta|e\epsilon\rangle\langle e\epsilon d\delta|c\gamma\rangle\langle b\beta d\delta|f\phi\rangle = \sqrt{(2e+1)(2f+1)}W(abcd;ef)\langle a\alpha f\phi|c\gamma\rangle.$$

Then, the matrix element can be rearranged as

$$\begin{aligned}
&\sum_{\sigma'} \frac{\sqrt{(2R+1)(2R'+1)}}{8\pi^2}\langle R'\mu' S\sigma'|IM\rangle W(R'4IS;RS) \\
&\times \langle R'\mu' S\sigma'|IM\rangle \frac{1}{\sqrt{2S+1}} A_\kappa \langle S||[S]^4_m||S\rangle \\
&\times \frac{8\pi^2}{2R+1}\langle R'k'4\kappa|RK\rangle \\
&= (-1)^{R+S-I} W(RSR'S;I4)\sqrt{2R'+1}A'_\kappa, \qquad \text{(A.51)}
\end{aligned}$$

where $A'_\kappa = A_\kappa\langle S||[S]^4_m||S\rangle$.

A.4.2 The matrix element of Zeeman coupling

We calculate the matrix element of Zeeman interaction using the base (3.14)

$$\begin{aligned}
\langle \Psi_{\nu IM}|Bg_s\tilde{S}_z|\Psi_{\nu' I' M'}\rangle &= \sum_{RR'kk'\sigma\sigma'} Bg_s f^{\nu I*}_{Rk} f^{\nu' I'*}_{R'k'} \\
&\times \langle R\mu S\sigma|IM\rangle\langle R'\mu' S\sigma|I'M\rangle\langle S\sigma|\tilde{S}_z|S\sigma'\rangle \\
&\times \frac{\sqrt{(2R+1)(2R'+1)}}{8\pi^2}\int \mathcal{D}^{R*}_{\mu k}\mathcal{D}^{R'}_{\mu' k'}d\Omega. \qquad \text{(A.52)}
\end{aligned}$$

Using the orthogonality of $\mathcal{D}$-function $\int \mathcal{D}^{j_1}_{\mu_1 m_1}\mathcal{D}^{j_2}_{\mu_2 m_2}d\Omega = 8\pi^2\delta_{j_1,j_2}\delta_{\mu_1,\mu_2}\delta_{m_1,m_1}/(2j_1+1)$ and Wigner-Eckart theorem, we obtain

$$\begin{aligned}
&= \sum_{RR'kk'\sigma\sigma'} Bg_s f^{\nu I*}_{Rk} f^{\nu' I'*}_{R'k'}\langle R\mu S\sigma|IM\rangle\langle R'\mu' S\sigma|I'M\rangle \frac{\langle S||[S]^1||S\rangle}{\sqrt{2S+1}}\langle S\sigma' 10|S\sigma\rangle \\
&\times \frac{\sqrt{(2R+1)(2R'+1)}}{8\pi^2}\frac{8\pi^2\delta_{R,R'}\delta_{\mu,\mu'}\delta_{kk'}}{2R+1}. \qquad \text{(A.53)}
\end{aligned}$$

where S is integer. Merging the Clebsch-Gordan coefficient to Racah coefficient:

$$\begin{aligned}
&= \sum_{Rk} Bg_S f^{\nu I*}_{Rk} f^{\nu' I'}_{Rk}(-1)^{2R+2S-(I+I')}\sqrt{(2S+1)(2I'+1)}W(1SIR;SI') \\
&\times \langle 10I'M|IM\rangle \frac{\sqrt{S(S+1)(2S+1)}}{\sqrt{2S+1}} \qquad \text{(A.54)} \\
&= Bg_S\sqrt{2I'+1}(-1)^{I'}\langle I'M10|IM\rangle \\
&\times \sum_{Rk}(-1)^{-R+S+1} f^{\nu I*}_{Rk} f^{\nu' I'}_{Rk} W(ISI'S;R1)\sqrt{S(S+1)(2S+1)}. \qquad \text{(A.55)}
\end{aligned}$$

A.5 The large angular momentum limit of the Clebsch-Gordan and Racah coefficient

A.5.1 The Clebsch-Gordan coefficient

The general form of the Clebsch-Gordan coefficient is

$$\begin{aligned}
\langle j_1 m_1 j_2 m_2|jm\rangle &= \left[\frac{(2j+1)(j_1+j_2-j)!(j_1+j-j_2)!(j+j_2-j_1)!}{(j_1+j_2+j+1)!}\right]^{1/2} \\
&\times \sum_z (-1)^z \frac{\sqrt{(j_1+m_1)!(j_1-m_1)!(j_2+m_2)!(j_2-m_2)!(j+m)!(j-m)!}}{z!(j_1+j_2-j-z)!(j_1-m_1-z)!(j_2-m_2-z)!(j-j_2+m_1+z)!(j-j_1-m_2+z)!}. \qquad \text{(A.56)}
\end{aligned}$$

Rewriting M with $j-j_1$, we get

$$\begin{aligned}
&= \sqrt{2j+1}\sum_z (-1)^z \frac{\sqrt{(j_2-M)!(j_2+M)!(j_2+m_2)!(j_2-m_2)!}}{z!(j_1-M-z)!(j_2-m_2-z)!(M-m_2+z)!} \\
&\times \sqrt{\frac{(j_1+j-j_2)!}{(j_1+j_2+j+1)!}}\frac{\sqrt{(j_1-m_1)!(j-m_1-m_2)!}}{(j_1-m_1-z)!}\frac{\sqrt{(j_1+m_1)!(j+m_1+m_2)!}}{(j-j_2+m_1+z)!}. \qquad \text{(A.57)}
\end{aligned}$$

We define $2\tilde{J} = j+j_1$, $2\tilde{M} = m+m_1$. We evaluate the asymptotic form of $j_1, j \gg j_2$,

$$\sqrt{\frac{(j_1+j-j_2)!}{(j_1+j_2+j+1)!}} = \sqrt{\frac{(2\tilde{J}-j_2)!}{(2\tilde{J}+j_2+1)!}} \simeq (2\tilde{J})^{-\frac{2j_2+1}{2}}, \qquad \text{(A.58)}$$

$$\frac{\sqrt{(j_1-m_1)!(j-m_1-m_2)!}}{(j_1-m_1-z)!} = \frac{\sqrt{(\tilde{J}-\tilde{M}-\frac{M-m_2}{2})!(\tilde{J}-\tilde{M}+\frac{M-m_2}{2})!}}{(\tilde{J}-\tilde{M}-\frac{M-m_2}{2}-z)!} \simeq (\tilde{J}-\tilde{M})^{\frac{M-m_2-2z}{2}}, \qquad \text{(A.59)}$$

$$\frac{\sqrt{(j_1+m_1)!(j+m_1+m_2)!}}{(j-j_2+m_1+z)!} = \frac{\sqrt{(\tilde{J}+\tilde{M}-\frac{M+m_2}{2})!(\tilde{J}+\tilde{M}+\frac{M+m_2}{2})!}}{(\tilde{J}+\tilde{M}-j_2+\frac{M-m_2}{2}+z)!} \simeq (\tilde{J}+\tilde{M})^{\frac{2j_2-M+m_2-2z}{2}}. \qquad \text{(A.60)}$$

Defining $\cos\frac{\theta}{2}=\sqrt{\frac{J+M}{2J}}$ and $\sin\frac{\theta}{2}=\sqrt{\frac{J-M}{2J}}$, we can rearrange the Eq. (A.57)

$$= \sqrt{\frac{2j+1}{2J}}\sum_z (-1)^z \frac{\sqrt{(j_2-M)!(j_2+M)!(j_2+m_2)!(j_2-m_2)!}}{z!(j_1-M-z)!(j_1-m_1-z)!(j_2-m_2-z)!(M-m_2+z)!} \times\left(\cos\frac{\theta}{2}\right)^{2j_2+m_2-M-2z}\left(\sin\frac{\theta}{2}\right)^{M-m_2-2z}. \tag{A.61}$$

Putting the definition of d-function,

$$d^j_{mm'}(\theta)=(-1)^{m-m'}\sum_\nu(-1)^\nu \times\frac{\sqrt{(j+m)!(j-m)!(j+m')!(j-m')!}}{(j-m-\nu)!(j+m'-\nu)!(m-m'+\nu)!\nu!}\left(\cos\frac{\theta}{2}\right)^{2j+m'-m-2\nu}\left(\sin\frac{\theta}{2}\right)^{m-m'+2\nu}, \tag{A.62}$$

into Eq. (A.61),we obtain the asymptotic form,

$$\langle j_1m_1j_2m_2|jm\rangle=\sqrt{\frac{2j+1}{2J}}(-1)^{M-m_2}d^{j_2}_{Mm_2}(\theta)\quad(j_1,j\ll j_2). \tag{A.63}$$

A.5.2 The Racah coefficient

The general form of the Racah coefficient is written as

$$W(abcd;ef)=S(abe)S(cdf)S(acf)S(bde)w(adcd;ef), \tag{A.64}$$

where

$$S(abe)=\sqrt{\frac{(a+b-e)!(b+e-a)!(e+a-b)!}{(a+b+e+1)!}} \tag{A.65}$$

$$w(abcd;ef)=\sum_z(-1)^z(a+b+c+d+1-z)!/\{(a+b-e-z)!(c+d-e-z)! \times(a+c-f-z)!(b+d-f-z)!z!(e+f-a-d+z)!(e+f-b-c+z)!\}. \tag{A.66}$$

The transformation $c-a=m, d-b=m', a+b-e-z=z'$ yields

$$W(abcd;ef)=(-1)^{e-a-b}\sum_{z'}(-1)^{z'}\frac{\sqrt{(f+m)!(f-m)!(f+m')!(f-m')!}}{(f-m-z')!(f+m-z')!(m-m'-z')!z'!} \times\sqrt{\frac{(a+c-f)!(b+d-f)!}{(a+c+f+1)!(b+d+f+1)!}} \times\frac{\sqrt{(a-b+e)!(b-a+e)!(c-d+e)!(d-c+e)!}}{(c-b+e-f+z')!(d-a+e-f+z')!} \times\sqrt{\frac{(a+b-e)!(c+d-e)!}{(a+b+e+1)!(c+d+e+1)!}} \times\frac{(c+d+e+1+z')!}{(a+b-e-z')!}. \tag{A.67}$$

Rearranging $\bar a=(a+c)/2, \bar b=(b+d)/2$, we get

$$W(abcd;ef)=(-1)^{e-a-b}\sum_{z'}(-1)^{z'}\frac{\sqrt{(f+m)!(f-m)!(f+m')!(f-m')!}}{(f-m-z')!(f+m-z')!(m-m'-z')!z'!} \times\sqrt{\frac{(2\bar a-f)(2\bar b-f)}{(2\bar a+1+f)!(2\bar b+1+f)!}} \times\frac{\sqrt{(\bar a-\bar b+e-\frac{m+m'}{2})!(\bar a-\bar b+e+\frac{m+m'}{2})!(\bar b-\bar a+e+\frac{m+m'}{2})!(\bar b-\bar a+e-\frac{m+m'}{2})!}}{(\bar a-\bar b+e+\frac{m-m'}{2}-f+z')!(\bar b-\bar a-e+\frac{m-m'}{2}-f+z')!} \times\sqrt{\frac{(\bar a+\bar b-e-\frac{m-m'}{2})!(\bar a+\bar b-e+\frac{m-m'}{2})!}{(\bar a+\bar b+e+1-\frac{m-m'}{2})!(\bar a+\bar b+e+1+\frac{m-m'}{2})!}} \times\frac{(\bar a+\bar b+e+1+\frac{m-m'}{2}+z')!}{(\bar a+\bar b-e-\frac{m-m'}{2}-z')!}. \tag{A.68}$$

We apply the assumption of $a,b,c,d,e\gg m,m',f$. Then we get asymptotic form

$$\sqrt{\frac{(2\bar a-f)(2\bar b-f)}{(2\bar a+1+f)!(2\bar b+1+f)!}}\simeq(2\bar a\times2\bar b)^{-(2f+1)/2}, \tag{A.69}$$

$$\frac{\sqrt{(\bar a-\bar b+e-\frac{m+m'}{2})!(\bar a-\bar b+e+\frac{m+m'}{2})!(\bar b-\bar a+e+\frac{m+m'}{2})!(\bar b-\bar a+e-\frac{m+m'}{2})!}}{(\bar a-\bar b+e+\frac{m-m'}{2}-f+z')!(\bar b-\bar a-e+\frac{m-m'}{2}-f+z')!} \simeq((\bar a-\bar b+e)(\bar b-\bar a+e))^{(m'-m+2f-2z')/2}, \tag{A.70}$$

$$\sqrt{\frac{(\bar{a}+\bar{b}-e-\frac{m-m'}{2})!(\bar{a}+\bar{b}-e+\frac{m-m'}{2})!}{(\bar{a}+\bar{b}+e+1-\frac{m-m'}{2})!(\bar{a}+\bar{b}+e+1+\frac{m-m'}{2})!}} \times \frac{(\bar{a}+\bar{b}+e+1+\frac{m-m'}{2}+z')!}{(\bar{a}+\bar{b}-e-\frac{m-m'}{2}-z')!}$$
$$\simeq (\bar{a}+\bar{b}-e)^{\frac{z'}{2}}(\bar{a}+\bar{b}-e)^{\frac{z'+m-m'}{2}}(\bar{a}+\bar{b}+e)^{\frac{z'}{2}}(\bar{a}+\bar{b}+e)^{\frac{z'+m-m'}{2}}$$
$$= \left\{(\bar{a}+\bar{b}+e)(\bar{a}+\bar{b}-e)\right\}^{\frac{2z'+m-m'}{2}}. \tag{A.71}$$

Using $\cos(\theta/2) = \sqrt{(\bar{a}-\bar{b}+e)(\bar{b}-\bar{a}+e)/4\bar{a}\bar{b}}$, $\sin(\theta/2) = \sqrt{(\bar{a}+\bar{b}+e)(\bar{b}+\bar{a}-e)/4\bar{a}\bar{b}}$, and definition of d function (A.62), we obtain the asymptotic form of Racah coefficient.

$$W(abcd;ef) = \frac{(-1)^{e-a-b-m+m'}}{\sqrt{4\bar{a}\bar{b}}} d^f_{mm'}(\theta) = \frac{(-1)^{e-d-c}}{\sqrt{4\bar{a}\bar{b}}} d^f_{c-a,b-d}(\theta). \tag{A.72}$$

Bibliography

[1] W. Knight, K. Clemenger, W. de Heer, W. Saunders, M. Chow, and M. Cohen, Phys. Rev. Lett. **52,** 2141 (1984).

[2] W. Knight, K. Clemenger, W. de Heer, W. Saunders, M. Chow, and M. Cohen, Phys. Rev. Lett. **53,** 510(E) (1984).

[3] E. Robbins, R. Leckenby, and P. Willis, Adv. Phys. **16,** 739 (1967).

[4] D. Awschalom and D. DiVincenzo, Physics Today **48,** 4, 43 (1995).

[5] S. N. Khanna and S. Linderoth, Phys. Rev. Lett. **67,** 742 (1991).

[6] G. F. Bertsch and K. Yabana, Phys. Rev. A **49,** 1930 (1994).

[7] G. F. Bertsch, N. Onishi, and K. Yabana, Z. Phys. D **34,** 213 (1995).

[8] V. Visuthikraisee and G. F. Bertsch, Phys. Rev. A **54,** 5140 (1996).

[9] N. Hamamoto, N. Onishi, and G. Bertsch, Phys. Rev. B (To be published) **61,** 1336 (2000).

[10] D. M. Cox, D. J. Trevor, R. L. Whetten, E. A. Rohlfing, and A. Kaldor, Phys. Rev. B **32,** 7290 (1985).

[11] D. M. Cox, D. J. Trevor, R. L. Whetten, E. A. Rohlfing, and A. Kaldor, J. Chem. Phys. **84,** 4651 (1986).

[12] I. M. L. Billas, A. Châtelain, and W. de Heer, Science **265,** 1682 (1994).

[13] D. C. Douglass, A. J. Cox, J. P. Bucher, and L. A. Bloomfield, Phys. Rev. B **47,** 12874 (1993).

[14] J. A. Becker and W. A. de Heer, Ber. Bunsenges. Phys. Chem **96,** 1237 (1992).

[15] D. C. Douglass, A. J. Cox, J. P. Bucher, and L. A. Bloomfield, Phys. Rev. B **47,** 12874 (1993).

[16] P. Milani and W. de Heer, Phys. Rev. B **44,** 8346 (1991).

[17] J. P. Bucher, D. C. Douglass, and L. A. Bloomfield, Sci. Instrum. **63,** 5667 (1992).

[18] N. Ashcroft and N. Mermin, *Solid State Physics* (Saunders College Publishing, 1976).

[19] Heukelom, Broeder, and V. Reijen, J. Chem. Phys. **51,** 474 (1954).

[20] C. Bean and I. Jacobs, J. Appl. Phys. **27,** 1448 (1956).

[21] W. Elmore, Phys. Rev. **54,** 1092 (1938).

[22] I. S. Jacobs and C. P. Bean, in *Magnetism III* (Academic, New York, 1963).

[23] G. Xia, S. H. Liou, A. Levy, and C. L. Chien, Phys. Rev. B **34,** 7573 (1986).

[24] D. C. Douglass, J. P. Bucher, and L. A. Bloomfield, Phys. Rev. Lett. **68,** 1774 (1992).

[25] H. Goldstein, *Classical mechanics* (Addition-Wesley, 1959).

[26] W. de Heer, P. Milani, and A. Châtelain, Phys. Rev. Lett. **65,** 488 (1990).

[27] J. G. Louderback, A. J. Cox, L. J. Lising, D. C. Douglass, and L. A. Bloomfield, Z. Phys. D **26,** 301 (1993).

[28] H. Akoh and A. Tasaki, J. Appl. Phys. **49,** 1410 (1978).

[29] C. Rau, B. Xing, M. Robert, and J. Vac. Sci. Technol. A **6,** 579 (1988).

[30] R. Fink, C. Ballentine, J. Erskine, and J. Araya-Pochet, Phys. Rev. B **41,** 10175 (1982).

[31] D. Douglass, J. Bucher, and L. Bloomfield, Phys. Rev. B **45,** 6341 (1992).

[32] P. J. Jensen and K. H. Bennemann, Z. Phys. D **29,** 67 (1994).

[33] P. J. Jensen and K. H. Bennemann, Z. Phys. D **26,** 246 (1993).

[34] S. E. Aspel, J. W. Emmert, J. Deng, and L. A. Bloomfield, Phys. Rev. Lett. **76,** 1441 (1996).

[35] J. Rodriguez-Lopez, F. Aguilera-Granja, A. Vega, and J. Alonso, Eur. Phys. J. D **6,** 235 (1999).

[36] N. Fujima and T. Yamaguchi, Phys. Rev. B **54,** 26 (1995).

[37] V. Kondratyev and H. Lutz, Phys. Rev. Lett. **81,** 4508 (1998).

[38] R. Galicia, Rev. Mex. Fis. **32,** 51 (1985).

[39] B. Reddy, S. Khanna, and B. Dunlap, Phys. Rev. Lett. **70,** 3323 (1993).

[40] A. J. Cox, J. G. Louderback, and L. A. Bloomfield, Phys. Rev. Lett. **71,** 923 (1993).

[41] A. J. Cox, J. G. Louderback, S. Aspel, and L. A. Bloomfield, Phys. Rev. B **49,** 12295 (1994).

[42] T. Hihara, S. Pokrant, and J. A. Becker, Chem. Phys. Lett. **294,** 357 (1998).

[43] C. Kittel, in *Introduciton to the solid state physics* (John Wiley & Sons, Inc., New York, 1986).

[44] A. Bohr and B. R. Mottelson, in *Nuclear Structure* (World Scientific, 1998), Vol. I.

[45] A. de Shalit and I. Talmi, *Nuclear Shell Theory* (Academic, New York, 1963).

[46] T. Holstein and H.Primakoff, Phys. Rev. **58,** 1098 (1940).

[47] J. F. Dyson, Phys. Rev. **102,** 1217,1230 (1956).

[48] J. Schwinger, in *Quantum Theory of Angular Momentum*, L. Biedenharn and H. V. Dam, eds., (Academic, New York, 1965).

[49] M. Yamanura, T. Suzuki, and H. Ichihashi, Prog. Theor. Phys. **60,** 197 (1978).

[50] H. Ichihashi and M. Yamanura, Prog. Theor. Phys. **60,** 753 (1978).

[51] W. Zhang, D. Feng, and R. Gilmore, Rev. Mod. Phys. **62,** 867 (1990).

[52] H. Kuratsuji and T. Suzuki, J. Math. Phys. **21,** 472 (1980).

[53] P. Ballone, P. Milani, and W. A. de Heer, Phys. Rev. B **44,** 10350 (1991).

[54] D. Pappas, A. Popov, A. Anisimov, B. Reddy, and S. Khanna, Phys. Rev. Lett. **76,** 4332 (1996).

[55] H. Tang, D. Weller, T. Walker, J. Scott, C. Chappert, H. Hopster, A. Pang, D. Dessau, and D. Pappas, Phys. Rev. Lett. **71,** 444 (1993).

[56] R. Wu, C. Li, A. Freeman, and C. Fu, Phys. Rev. B **44,** 9400 (1991).

[57] J. Giergiel, A. Pang, H. Hopster, X. Guo, S. Tong, and D. Weller, Phys. Rev. B **51,** 10201 (1995).

[58] T. Oda, A. Pasquarello, and R. Car, Phys. Rev. Lett **80,** 3622 (1998).

[59] M. Castro, C. Jamorski, and D. Salahub, Chem. Phys. Lett. **271,** 133 (1997).

[60] K. Lee, J. Callaway, K. Kwong, R. Tang, and A. Ziegler, Phys. Rev. B **31,** 1796 (1985).

[61] S. Asano and J. Yamashita, J. Phys. Soc. Japan **31,** 1000 (1971).

[62] G. Pastor, J.Dorantes-Dávila, and K. Benemann, Physica B **149,** 22 (1988).